BIOPHYSICAL SIGNIFICANCE OF MITOCHONDRIAL PROPERTIES ON MITOCHONDRIAL FUNCTION: EXPERIMENTAL-COMPUTATIONAL APPROACH

by

Dong Hoon Song

A dissertation submitted in partial fulfillment
of the requirements for the degree of
Doctor of Philosophy
(Mechanical Engineering)
in The University of Michigan
2013

Doctoral Committee:

Emeritus Professor Ann Marie Sastry, Co-Chair
Professor Wei Lu, Co-Chair
Associate Professor Christian Lastoskie
Assistant Research Scientist Jonghyun Park
Professor Martin Philbert

DEDICATION

To my family

TABLE OF CONTENTS

LIST OF TABLES

LIST OF FIGURES

ABSTRACT

With the increase in average life expectancy over the last few decades, the importance of research on central nervous system (CNS) diseases has continuously grown. In one effort to reveal the mechanisms of these diseases, mitochondria have been extensively studied in close relation to neurodegeneration and aging because of their decisive roles in apoptosis and cellular bioenergetics. However, the precise mechanisms behind mitochondrial functions in the development and progression of CNS diseases as well as how mitochondrial properties may reflect the functional states of mitochondria have not yet been elucidated.

Throughout the dissertation, we started our mitochondrial research at the level of individual mitochondria. The scope of the research was then extended to the properties of the mitochondrial population. Finally, we shifted our attention into the internal structure and corresponding electrochemistry of mitochondria.

First, we introduced image analysis methods in order to simultaneously quantify the changes in mitochondrial properties under 1,3-DNB exposure. By using these image analysis techniques, we presented that major membrane potential fluctuations are mostly accompanied by abrupt changes in mitochondrial morphology. Additionally, we found that 1,3-DNB can induce statistically significant changes in mitochondrial morphology and membrane potential, and that theses alterations may not be related to the mitochondrial permeability transition.

Next, we developed a mitochondrion model simulating the electrochemical potential gradient across the inner mitochondrial membrane (IMM) and investigated the biophysical significance of the IMM. By performing simulations with various morphological parameters, we showed that a crista can enhance the capacity for ATP synthesis. Moreover, we identified key morphological parameters that may potentially represent the energy state of mitochondria.

Finally, we investigated the effects of the local pH gradient on the IMM dynamics. A numerical model was developed to simulate the morphological evolution of the cristae membrane at the given pH profile. By using this model, we demonstrated that a tubular crista structure can be formed and regulated by the local pH gradient. The simulation results also suggested that the cristae membrane may contain a higher composition of cardiolipin than the other parts of the IMM.

CHAPTER 1

INTRODUCTION

1.1. CHALLENGES

As average life expectancy has increased, the prevalence and risk of central nervous system (CNS) diseases, such as Alzheimer's disease, Parkinson's disease and Huntington's disease, have increased as well. As of 2013, about 5.2 million Americans of all ages were found to have Alzheimer's disease, which is the most common type of CNS disease. Moreover, the risk of Alzheimer's disease increases with age. About 11% of Americans aged 65 and older have Alzheimer's disease, whereas about 32% of Americans aged 85 and older suffer from this disease. Consequently, about one third of senior Americans die with Alzheimer's disease or other types of dementia [1]. However, the precise mechanism of what triggers the initiation and progression of CNS diseases remains elusive.

In the initiation and progression of these CNS diseases, the impairing of mitochondrial function has been considered a critical process because of the decisive roles of mitochondria in apoptosis and cellular bioenergetics. For example, studies have found that the impairing of mitochondrial function can disrupt energy metabolism, causing mitochondrial DNA mutation. During this process, disrupted energy metabolism

may produce oxidative stress, concomitantly increasing the risk of mitochondrial DNA mutation. The resulting muted mitochondrial DNA can exacerbate already disrupted energy metabolism [2-7]. With these cycling interactions, mitochondrial function may be an underlying mechanism of the progression of CNS diseases.

Moreover, abnormal mitochondrial properties, which are potentially associated with the mitochondrial dysfunction, have been observed in CNS diseases. These abnormal mitochondrial properties include loss of membrane potential, swollen and fragmented external morphologies, and degenerated internal structures [8-11]. These changes in mitochondrial properties may reflect alterations in the disease states of a mitochondrion.

Therefore, studies on mitochondrial properties (such as external and internal morphologies and mitochondrial membrane potential) from mitochondria in different functional or disease states may provide a better understanding of the role of mitochondria in CNS diseases. Finally, this study may allow the use of mitochondrial properties (as an indicator of CNS disease) in diagnosis as well as the development of new treatments.

In the next section, we summarize existing research concerning the role of mitochondria in CNS diseases. In particular, studies on mitochondrial membrane potential and morphology are comprehensively reviewed. Finally, we identify research areas that require further investigation.

1.2. PRIOR ART ON MITOCHONDRIAL RESEARCH

1.2.1. Role of mitochondria in CNS diseases

The primary function of mitochondria is to provide cellular energy by synthesizing ATP. In addition to this energetic function, mitochondria also play important roles in signaling cell cycle and regulating cell death via apoptosis. Moreover, as major sources of reactive oxygen species, mitochondria are vulnerable to oxidative damages. Because of these critical functions and potential susceptibility, mitochondria have been investigated in close relation to various diseases such as diabetes, Leber's hereditary optic neuropathy, Leigh syndrome, and mitochondrial myopathy [12-14]. In particular, impaired mitochondrial functions in the regulations of cellular energy and reactive oxygen species levels have been hypothesized as the underlying mechanism of the initiation and progression of CNS diseases. In this section, we review the existing literature on the role of mitochondria in CNS diseases.

In Table 1.1, we summarized selected literature on the role of mitochondria in CNS diseases. The roles of mitochondria in CNS disease have been investigated in several aspects. Studies have found impaired mitochondrial functions, including decreased activities of electron transport chain and damaged mitochondrial DNA (mtDNA), in CNS diseases patients [2-4]. Defects in energy metabolism may induce oxidative stress, and consequently result in mtDNA mutation. This mtDNA mutation can exacerbate oxidative phosphorylation (i.e., energy metabolism). This interaction between energy metabolism and oxidative stress may be the mechanism of mitochondrial dysfunction in CNS diseases. Additionally, studies have suggested different mechanisms

of mitochondrial dysfunction in sporadic Alzheimer's disease and familiar Alzheimer's disease: mitochondrial dysfunction may initiate sporadic Alzheimer's disease, whereas the progression of familial Alzheimer's disease may result in mitochondrial dysfunction [5]. Moreover, studies have also provided evidence supporting the critical role of mitochondria in the initiation and progression of Parkinson's disease [7].

Finally, there have been studies focusing on altered mitochondrial properties in CNS diseases. By investigating mitochondria from patients with CNS diseases, abnormal properties and defected fusion fission dynamics of mitochondria have been observed. For example, swollen mitochondria presenting loss of cristae membranes were observed from Parkinson's diseas and Alzheimer's disease cybrid cells [8]. Similarly, mitochondria from Alzheimer's disease patients and Huntington's disease patients showed abnormal cristae morphologies [15, 16]. In addition to the abnormalities in morphology, impaired mitochondrial dynamics (unbalanced fusion and fission) was found in Alzheimer's disease [17]. In the next two sections, mitochondrial properties, specifically mitochondrial membrane potential (1.2.2) and morphology (1.2.3) are comprehensively reviewed.

Table 1.1. Prior art on mitochondria and CNS diseases

Year	Author	Focus	Conclusions
1995	Bowling et al. [2]	Mitochondrial dysfunction and oxidative stress in CNS	Mitochondrial dysfunction and oxidative stress may be the pathogenesis of CNS disease
2001	Hirai et al. [3]	Mitochondria in AD	Increase in mtDNA and decrease in number of mitochondria were observed in AD
2002	Castellani et al. [4]		Abnormal mitochondrial function is associated with AD
2005	Reddy et al. [5]		Mitochondrial defects may result in sporadic AD, while mitochondrial abnormalities and oxidative damage may result from familial AD
2009	Yao et al. [6]		Mitochondrial dysfunction and resulting energy deficit occur early in AD pathogenesis
2011	Keane et al. [7]	Mitochondria in PD	Evidence supporting the close relationship between mitochondrial dysfunction and neuronal cell death in PD were reviewed
2000	Trimmer et al. [8]	Abnormal morphology	Morphologically abnormal mitochondria were observed from PD and AD cybrid cells
2003	Sharma et al. [15]		Swollen mitochondria with defected cristae were found in AD
2003	Yu et al. [16]		Swollen mitochondria with abnormal cristae were observed in Huntington's disease
2009	Wang et al. [17]	Abnormal mitochondrial dynamics	Impaired balance in mitochondrial fission and fusion may be an underlying mechanism of mitochondrial dysfunction

1.2.2. Mitochondrial membrane potential

Mitochondrial membrane potential is a critical parameter determining the viability of a mitochondrion because it regulates respiratory activities and ATP synthesis. During oxidative phosphorylation, electrochemical potential called the proton motive force is generated by electron transport chain (complex I, II, II, and IV) and utilized for synthesizing ATP via ATP synthase (complex V). Mitochondrial membrane potential is the electric potential component of this proton motive force.

Even though the exact mechanism of how mitochondrial membrane potential is generated and regulated is still controversial, it is generally accepted that mitochondrial membrane potential is induced by coupled electron transport and proton translocation. By using free energy released from a series of redox reactions, the electron transport chain pumps protons across the inner mitochondrial membrane (IMM), and consequently the outer side of the IMM is positively charged by these protons. In the mean time, electrons transferred through the electron transport chain charged the inner side of the IMM negatively. Finally, mitochondrial membrane potential is generated by this charge separation across the IMM [18-23].

In Table 1.2, selected literature on mitochondrial membrane potential is summarized. Mitochondrial membrane potential has been primarily measured by using potentiometric fluorescent dyes such as TMRE (Tetramethyl Rhodamine Eethyl Ester), TMRM (Tetramethyl Rhodamine Methyl Ester), R123 (rhodamine 123), and JC-1 (5,5',6,6'-tetrachloro-1,1',3,3'-tetraethylbenzimidazolocarbocyanine iodide) [24-30]. To estimate mitochondrial membrane potential, the Nersnt equation was applied to the ratio of intramitochondrial fluorescence and cytosolic fluorescence. This method enables the

measuring of mitochondrial membrane potential in living cells, and consequently the investigating of factors affecting mitochondrial membrane potential.

In particular, factors inducing disruption or fluctuation of mitochondrial membrane potential have been extensively studied. For example, increased permeability of the IMM (by opening of mitochondrial permeability transition pores) was observed when mitochondria underwent rapid depolarizations [31]. Other factors such as Ca^{2+} influx, activities of ATP synthase, free radicals from the matrix side of mitochondria, and TMRM photoactivation were also considered to induce fluctuations of mitochondrial membrane potential [32-35]. Moreover, studies have found that this mitochondrial membrane potential disruption (mediated by permeability transition) can propagate from one mitochondrion to another by communicating the release of reactive oxygen species [36]. Given that these factors inducing disruption of mitochondrial membrane potential are closely related to energy metabolism, oxidative damages, and apoptosis, studies have investigated this disruption as an indicator of mitochondrial dysfunction [31, 37]. However, the underlying mechanism of how mitochondrial membrane potential represents the functional states of mitochondria remains elusive and requires further investigation.

Table 1.2. Prior art on mitochondrial membrane potential (MMP)

Year	Author	Focus	Conclusions
1993	Loew et al. [24]	MMP quantification	MMP was estimated by using three-dimensional imaging microscopy and mathematical modeling
1999	Lemaster et al. [26]		The methods for measuring MMP and pH by using confocal microscopy were introduced
2008	Distelmaier et al. [29]		An automated protocol was developed to measure MMP in living cells at the level of individual mitochondria
1998	Huser et al. [31]	MMP fluctuation inducing factors	MMP fluctuation may be caused by mitochondrial permeability transition
1998	Duchen et al. [32]		MMP fluctuation may be caused by Ca^{2+} influx
2001	Buckman et al. [33]		MMP fluctuation may be caused by F_0F_1 ATPase activity
2003	Aon et al. [34]		MMP fluctuation may be caused by free radicals from matrix side of mitochondria
2005	Falchi et al. [35]		MMP fluctuation may be caused by TMRM photoactivation
2003	Vergun et al. [37]	MMP fluctuation and mitochondrial dysfunction	MMP fluctuation may be an intermediate state to mitochondrial dysfunction
2004	Brady et al. [36]	Propagation of mitochondrial depolarization	Mitochondrial permeability transition (causing MMP fluctuation) can propagate from one mitochondrion to another via reactive oxygen species induced reactive oxygen species release
2005	Hattori et al. [38]	Transient depolarization	Transient depolarization may be caused by the opening of a proton conductive channel

1.2.3. Mitochondrial morphology

Mitochondria are double-membraned organelles, structurally defined by the inner mitochondrial membrane (IMM) and the outer mitochondrial membrane (OMM). These membranes are composed of phospholipid bilayers and proteins. The OMM defines the outer boundary of the organelle, and is permeable to molecules of about 5000 daltons or less. On the other hand, the IMM, which is a major site of the electron transport chain and ATP synthase, is impermeable to most molecules. The space between the IMM and the OMM is the intermembrane space. The matrix is the space enclosed by the IMM, containing the mitochondrial DNA and high concentrations of enzymes [39]. Because of this compartmentalized structure of a mitochondrion, studies have focused either on the external structure or the internal structure (IMM morphology).

The external morphologies of mitochondria have been studied in close relation to fusion and fission dynamics. Many studies have found evidence supporting the hypothesis that the external mitochondrial morphologies (regulated by fusion and fission) may reflect the functional states of mitochondria [39-43]. Moreover, mitochondrial fission has been considered to be a critical step of programmed cell death (apoptosis) [42, 43]. However, the underlying mechanisms of these hypotheses (i.e., how mitochondrial morphology and dynamics are related to apoptosis and bioenergetics) are not well understood, and these hypotheses have not been supported by quantitative data.

Recently, numerous advanced image processing and analysis techniques were developed. With these techniques, mitochondrial morphologies were quantified in living cells [30, 44-46]. However, studies on the external morphology as an indicator of mitochondrial functional states is still insufficient.

In the past decade, with the support of progress in imaging techniques, the internal structure of a mitochondrion has been comprehensively studied. The components of the internal structure of a mitochondrion were visualized and analyzed with advanced imaging techniques. In particular, cristae, which are infoldings of the IMM, have been extensively studied [47-57]. The folded morphology of the cristae membrane (CM) has been hypothesized to provide a greater capacity for ATP synthesis by increasing the surface area, whereas the narrow crista junction, which connects the CM and the inner boundary membrane, has been hypothesized as a diffusion barrier of molecules such as substrates and metabolites [48, 49, 56]. Additionally, recent studies have shown that the IMM has a diverse and dynamic morphology that differ widely among different physiological and pathological conditions. For example, electron tomography showed two distinctive IMM morphologies from mitochondria in two different energy states [50, 51, 55]. The condensed conformation (characterized by enlarged cristae and contracted matrix) was observed from mitochondria in state III, while the orthodox conformation (characterized by constricted cristae and expanded matrix) was shown from mitochondria in state IV. As mentioned earlier in Section 1.2.1, more detrimental changes in the IMM morphology (loss of cristae) were observed from mitochondria in neurodegenerative diseases [8, 15, 16]. However, how the IMM morphologies are associated with the functional and disease states of mitochondria remains unclear.

Table 1.3. Prior art on mitochondrial morphologies

Year	Author	Focus	Conclusions
1994	Bereiter-Hahn et al. [39]	Fusion, fission and apoptosis	Mitochondrial dynamics including fusion and fission were reviewed
2003	Karbowski et al. [40]		Mitochondrial morphology can be regulated by fusion and fission
2005	Perfettini et al. [41]		Fission may induce or inhibit apoptosis depending on the initial lethal stimulus
2005	Youle et al. [42]		Mitochondrial fission may be a critical step in apoptosis
2010	Sauvanet et al. [43]		Evidence supporting that mitochondrial morphologies may represent their functional states was reviewed
2006	Koopman et al. [44]	Quantitative analysis	Multiple mitochondrial parameters in living cells were simultaneously quantified
2007	Kaasik et al. [45]		Morphological parameters of swollen mitochondria were measured by using 3D reconstructions
2010	Murphy et al. [46]		Morphologies of mitochondria from mutant cells were compared with normal cells by using ion-abrasion scanning electron microscopy
2000	Frey et al. [47]	IMM morphology	3D structure of the IMM was visualized by using electron microscopic tomography
2006	Mannella [50]		Distinctive IMM structures were observed from mitochondria in different energy states
2009	Zick et al. [57]		Widely varied IMM structures between cell types and physiological states were reviewed
2011	Perkins et al. [55]		It was shown that the morphology of the IMM is related to the workload of mitochondria

1.3. SCOPE AND OUTLINE OF THE DISSERTATION

In Chapters 2 through 4, we investigate the effects of mitochondrial properties on mitochondrial functions. Specifically, in Chapter 2, we begin our study of mitochondria with individual mitochondria and then extend the scope to the average properties of the mitochondrial population. In Chapters 3 and 4, we shift our focus to the internal structure and corresponding electrochemistry of mitochondria.

In Chapter 2, the changes in mitochondrial properties under 1,3-DNB are investigated. We introduce imaging and image processing techniques applicable to simultaneous quantification of mitochondrial properties. With these techniques, we investigate the effects of 1,3-DNB on the mitochondrial properties of both individual mitochondria and the mitochondrial population.

In Chapter 3, we study the role of dynamic and diverse internal structures of mitochondria on ATP synthesis. A model is developed to simulate the distributions of electric potential and proton concentration at the given mitochondrial morphologies. By using this model, we investigate the biophysical significance of cristae membrane structures and examine morphological parameters potentially related to ATP synthesis.

In Chapter 4, we investigate the effects of the local pH gradient on the cristae membrane morphology. A model simulating the optimized inner mitochondrial membrane morphologies at the given pH profiles is introduced. By using this model, we investigate the mechanisms of cristae formation and regulation.

Finally, in Chapter 5, our major findings and contributions are summarized. In addition, we suggest future work.

1.4. BIBLIOGRAPHY

1.   2013 Alzheimer's disease facts and figures. *Alzheimers Dement* 9, 208 (2013).
2.   A. C. Bowling, and M. F. Beal, Bioenergetic and oxidative stress in neurodegenerative diseases. *Life sciences* 56, 1151 (1995).
3.   K. Hirai, G. Aliev, A. Nunomura, H. Fujioka, R. L. Russell, C. S. Atwood, A. B. Johnson, Y. Kress, H. V. Vinters, and M. Tabaton, Mitochondrial abnormalities in Alzheimer's disease. *The Journal of neuroscience* 21, 3017 (2001).
4.   R. Castellani, K. Hirai, G. Aliev, K. L. Drew, A. Nunomura, A. Takeda, A. D. Cash, M. E. Obrenovich, G. Perry, and M. A. Smith, Role of mitochondrial dysfunction in Alzheimer's disease. *Journal of Neuroscience Research* 70, 357 (2002).
5.   P. H. Reddy, and M. F. Beal, Are mitochondria critical in the pathogenesis of Alzheimer's disease? *Brain research reviews* 49, 618 (2005).
6.   J. Yao, R. W. Irwin, L. Zhao, J. Nilsen, R. T. Hamilton, and R. D. Brinton, Mitochondrial bioenergetic deficit precedes Alzheimer's pathology in female mouse model of Alzheimer's disease. *Proceedings of the National Academy of Sciences* 106, 14670 (2009).
7.   P. Keane, M. Kurzawa, P. Blain, and C. Morris, Mitochondrial dysfunction in Parkinson's disease. *Parkinson's disease* 2011, (2011).
8.   P. A. Trimmer, R. H. Swerdlow, J. K. Parks, P. Keeney, J. P. Bennett, S. W. Miller, R. E. Davis, and W. D. Parker, Abnormal mitochondrial morphology in sporadic Parkinson's and Alzheimer's disease cybrid cell lines. *Experimental Neurology* 162, 37 (2000).
9.   D. C. Chan, Mitochondria: dynamic organelles in disease, aging, and development. *Cell* 125, 1241 (2006).
10.   M. S. Parihar, and G. J. Brewer, Simultaneous age-related depolarization of mitochondrial membrane potential and increased mitochondrial reactive oxygen species production correlate with age-related glutamate excitotoxicity in rat hippocampal neurons. *Journal of Neuroscience Research* 85, 1018 (2007).
11.   K. F. Winklhofer, and C. Haass, Mitochondrial dysfunction in Parkinson's disease. *Biochimica et Biophysica Acta (BBA)-Molecular Basis of Disease* 1802, 29 (2010).
12.   D. C. Wallace, Mitochondrial Diseases in Man and Mouse. *Science* 283, 1482 (March 5, 1999, 1999).
13.   S. DiMauro, Mitochondrial diseases. *Biochimica et Biophysica Acta (BBA) - Bioenergetics* 1658, 80 (2004).
14.   A. H. Schapira, Mitochondrial diseases. *The Lancet*, (2012).
15.   S. K. Sharma, Neuroprotective actions of Selegiline in inhibiting 1-methyl, 4-phenyl, pyridinium ion (MPP)-induced apoptosis in SK-N-SH neurons. *Journal of neurocytology* 32, 329 (2003).
16.   Z. X. Yu, Mutant huntingtin causes context-dependent neurodegeneration in mice with Huntington's disease. *The Journal of neuroscience* 23, 2193 (2003).

17. X. Wang, B. Su, H.-g. Lee, X. Li, G. Perry, M. A. Smith, and X. Zhu, Impaired balance of mitochondrial fission and fusion in Alzheimer's disease. *The Journal of neuroscience* 29, 9090 (2009).

18. P. Mitchell, Chemiosmotic coupling in oxidative and photosynthetic phosphorylation. *Biological Reviews* 41, 445 (1966).

19. M. Prats, J.-F. Tocanne, and J. Teissie, Lateral proton conduction at a lipid/water interface. Its modulation by physical parameters. Experimental and mathematical approaches. *European journal of biochemistry* 149, 663 (1985).

20. J. Heberle, J. Riesle, G. Thiedemann, D. Oesterhelt, and N. A. Dencher, Proton migration along the membrane surface and retarded surface to bulk transfer. *Nature (London)* 370, 379 (1994).

21. Y. N. Antonenko, and P. Pohl, Coupling of proton source and sink via H^+-migration along the membrane surface as revealed by double patch-clamp experiments. *FEBS Letters* 429, 197 (1998).

22. L. S. Yaguzhinsky, V. I. Yurkov, and I. P. Krasinskaya, On the localized coupling of respiration and phosphorylation in mitochondria. *Biochimica et Biophysica Acta (BBA) - Bioenergetics* 1757, 408 (2006).

23. N. Kocherginsky, Acidic lipids, H^+-ATPases, and mechanism of oxidative phosphorylation. Physico-chemical ideas 30 years after P. Mitchell's Nobel Prize award. *Progress in Biophysics and Molecular Biology* 99, 20 (2009).

24. L. M. Loew, R. A. Tuft, W. Carrington, and F. S. Fay, Imaging in five dimensions: time-dependent membrane potentials in individual mitochondria. *Biophysical Journal* 65, 2396 (1993).

25. C. Fink, F. Morgan, and L. M. Loew, Intracellular fluorescent probe concentrations by confocal microscopy. *Biophysical Journal* 75, 1648 (1998).

26. J. J. Lemasters, D. R. Trollinger, T. Qian, W. E. Cascio, and H. Ohata, Confocal imaging of Ca^{2+}, pH, electrical potential, and membrane permeability in single living cells. *Methods in Enzymology* 302, 341 (1999).

27. S. Nakayama, T. Sakuyama, S. Mitaku, and Y. Ohta, Fluorescence imaging of metabolic responses in single mitochondria. *Biochemical and Biophysical Research Communications* 290, 23 (2002).

28. G. Solaini, G. Sgarbi, G. Lenaz, and A. Baracca, Evaluating mitochondrial membrane potential in cells. *Bioscience reports* 27, 11 (2007).

29. F. Distelmaier, W. J. H. Koopman, E. R. Testa, A. S. de Jong, H. G. Swarts, E. Mayatepek, J. A. M. Smeitink, and P. H. G. M. Willems, Life cell quantification of mitochondrial membrane potential at the single organelle level. *Cytometry Part A* 73A, 129 (2008).

30. W. J. H. Koopman, F. Distelmaier, J. J. Esseling, J. A. M. Smeitink, and P. H. G. M. Willems, Computer-assisted live cell analysis of mitochondrial membrane potential, morphology and calcium handling. *Methods* 46, 304 (2008).

31. J. Hüser, C. E. Rechenmacher, and L. A. Blatter, Imaging the Permeability Pore Transition in Single Mitochondria. *Biophysical Journal* 74, 2129 (1998).

32. M. R. Duchen, A. Leyssens, and M. Crompton, Transient mitochondrial depolarizations reflect focal sarcoplasmic reticular calcium release in single rat cardiomyocytes. *The Journal of Cell Biology* 142, 975 (1998).

33. J. F. Buckman, and I. J. Reynolds, Spontaneous changes in mitochondrial membrane potential in cultured neurons. *The Journal of neuroscience* 21, 5054 (2001).

34. M. A. Aon, S. Cortassa, E. Marbán, and B. O'Rourke, Synchronized whole cell oscillations in mitochondrial metabolism triggered by a local release of reactive oxygen species in cardiac myocytes. *Journal of Biological Chemistry* 278, 44735 (2003).

35. A. M. Falchi, R. Isola, A. Diana, M. Putzolu, and G. Diaz, Characterization of depolarization and repolarization phases of mitochondrial membrane potential fluctuations induced by tetramethylrhodamine methyl ester photoactivation. *FEBS journal* 272, 1649 (2005).

36. N. R. Brady, S. P. Elmore, J. J. van Beek, K. Krab, P. J. Courtoy, L. Hue, and H. V. Westerhoff, Coordinated behavior of mitochondria in both space and time: a reactive oxygen species-activated wave of mitochondrial depolarization. *Biophysical Journal* 87, 2022 (2004).

37. O. Vergun, T. V. Votyakova, and I. J. Reynolds, Spontaneous changes in mitochondrial membrane potential in single isolated brain mitochondria. *Biophysical Journal* 85, 3358 (2003).

38. T. Hattori, K. Watanabe, Y. Uechi, H. Yoshioka, and Y. Ohta, Repetitive transient depolarizations of the inner mitochondrial membrane induced by proton pumping. *Biophysical Journal* 88, 2340 (2005).

39. J. Bereiter-Hahn, and M. Vöth, Dynamics of mitochondria in living cells: shape changes, dislocations, fusion, and fission of mitochondria. *Microscopy research and technique* 27, 198 (1994).

40. M. Karbowski, and R. Youle, Dynamics of mitochondrial morphology in healthy cells and during apoptosis. *Cell Death & Differentiation* 10, 870 (2003).

41. J.-L. Perfettini, T. Roumier, and G. Kroemer, Mitochondrial fusion and fission in the control of apoptosis. *Trends in cell biology* 15, 179 (2005).

42. R. J. Youle, and M. Karbowski, Mitochondrial fission in apoptosis. *Nature reviews Molecular cell biology* 6, 657 (2005).

43. C. Sauvanet, S. Duvezin-Caubet, J.-P. di Rago, and M. Rojo, in *Seminars in cell & developmental biology*. (Elsevier, 2010), vol. 21, pp. 558-565.

44. W. J. Koopman, H. J. Visch, J. A. Smeitink, and P. H. Willems, Simultaneous quantitative measurement and automated analysis of mitochondrial morphology, mass, potential, and motility in living human skin fibroblasts. *Cytometry Part A* 69, 1 (2006).

45. A. Kaasik, D. Safiulina, V. Choubey, M. Kuum, A. Zharkovsky, and V. Veksler, Mitochondrial swelling impairs the transport of organelles in cerebellar granule neurons. *Journal of Biological Chemistry* 282, 32821 (2007).

46. G. E. Murphy, B. C. Lowekamp, P. M. Zerfas, R. J. Chandler, R. Narasimha, C. P. Venditti, and S. Subramaniam, Ion-abrasion scanning electron microscopy reveals distorted liver mitochondrial morphology in murine methylmalonic acidemia. *Journal of Structural Biology* 171, 125 (2010).

47. T. G. Frey, and C. A. Mannella, The internal structure of mitochondria. *Trends in biochemical sciences* 25, 319 (2000).

48. T. G. Frey, C. W. Renken, and G. A. Perkins, Insight into mitochondrial structure and function from electron tomography. *Biochimica et Biophysica Acta (BBA) - Bioenergetics* 1555, 196 (2002).

49. C. A. Mannella, The relevance of mitochondrial membrane topology to mitochondrial function. *Biochimica et Biophysica Acta (BBA) - Molecular Basis of Disease* 1762, 140 (2006).

50. C. A. Mannella, Structure and dynamics of the mitochondrial inner membrane cristae. *Biochimica et Biophysica Acta (BBA) - Molecular Cell Research* 1763, 542 (2006).

51. C. A. Mannella, Structural diversity of mitochondria. *Annals of the New York Academy of Sciences* 1147, 171 (2008).

52. C. A. Mannella, D. R. Pfeiffer, P. C. Bradshaw, I. I. Moraru, B. Slepchenko, L. M. Loew, C. E. Hsieh, K. Buttle, and M. Marko, Topology of the mitochondrial inner membrane: dynamics and bioenergetic implications. *IUBMB Life* 52, 93 (2001).

53. G. Perkins, E. Bossy-Wetzel, and M. H. Ellisman, New insights into mitochondrial structure during cell death. *Experimental Neurology* 218, 183 (2009).

54. G. Perkins, C. Renken, M. E. Martone, S. J. Young, M. Ellisman, and T. Frey, Electron tomography of neuronal mitochondria: three-dimensional structure and organization of cristae and membrane contacts. *Journal of Structural Biology* 119, 260 (1997).

55. G. A. Perkins, and M. H. Ellisman, Mitochondrial configurations in peripheral nerve suggest differential ATP production. *Journal of Structural Biology* 173, 117 (2011).

56. G. A. Perkins, C. W. Renken, T. G. Frey, and M. H. Ellisman, Membrane architecture of mitochondria in neurons of the central nervous system. *Journal of Neuroscience Research* 66, 857 (2001).

57. M. Zick, R. Rabl, and A. S. Reichert, Cristae formation—linking ultrastructure and function of mitochondria. *Biochimica et Biophysica Acta (BBA) - Molecular Cell Research* 1793, 5 (2009).

CHAPTER 2

QUANTITATIVE ANALYSIS OF MITOCHONDRIAL PROPERTIES UNDER 1,3-DNB EXPOSURE

2.1. INTRODUCTION

Mitochondria are the primary cellular powerhouses in most eukaryotic cells because their main function is synthesizing ATP. In addition to ATP synthesis, mitochondria participate in signaling calcium, controlling the cell cycle, and regulating the apoptotic pathway. Moreover, mitochondria are dynamic organelles that can change their properties in response to physiological and pathological conditions [1-3]. Because of these critical and dynamic functions of mitochondria in cell viability, their dysfunction has been investigated in connection with central nervous system (CNS) diseases such as Alzheimer's disease, Parkinson's disease, and Huntington's disease [4-10]. In particular, the abnormal mitochondrial properties (including loss of membrane potential, swollen and fragmented external morphologies, and degenerated internal structures) have been hypothesized as the critical criteria for the initiation and the progression of CNS diseases [3, 11-13]. Therefore, investigating mitochondrial properties in different disease states may provide a better understanding of the role of mitochondria in CNS diseases.

There have been many studies investigating altered mitochondrial properties in different disease states. For example, swollen mitochondria with degenerated cristae membranes were observed in Parkinson's disease and Alzheimer's disease cybrid cells [11]. Abnormal mitochondrial dynamics (impaired balance of fission and fusion) was found in Alzheimer's disease [14]. Fragmented mitochondrial morphology and decreased membrane potential were observed under neurotoxin challenges such as 1,3-Dinitrobenzene (DNB) [15-17]. However, these studies mostly provided only qualitative descriptions of the changes in mitochondrial properties.

Recently, with the aid of progress in image processing techniques, several methods for the quantification of mitochondrial properties were introduced. Mitochondrial membrane potential was estimated by using potentiometric fluorescent dyes [18-24]. The diameter and volume of swollen mitochondria were measured by 3D reconstructions [25]. 3D image processing techniques were applied to access mitochondrial fusion and fission [26]. Mitochondrial properties including mitochondrial membrane potential and morphology were simultaneously quantified [24]. However, these quantitative analyses have not sufficiently investigated the properties of mitochondria in association with functional and disease states of mitochondria.

In this study, we investigate the alterations in mitochondrial properties induced by 1,3-DNB exposure because this neurotoxin can reproduce the neurotoxic response of CNS diseases. First, the imaging technique is refined to independently capture both the morphology and the membrane potential of mitochondria. For the accurate quantification of mitochondrial properties, we introduce image processing and data analysis techniques. By using these techniques, we investigate i) the correlation between mitochondrial

properties (Section 2.3.1), ii) the effects of 1,3-DNB on mitochondrial properties (Section 2.3.2), and iii) the effects of mitochondrial permeability transition inhibitors (Section 2.3.3). Finally, the limitations of this study are discussed.

2.2. METHODS

2.2.1. Experimental methods

Immortalized astrocyte cell lines (DI TNC) were obtained from the American Type Culture Collection. These cells were cultured to have passages between 4 and 30 and were exposed to 50, 100, 200, 400, and 600 μM concentrations of 1,3-DNB within a 26-hour period. After 1,3-DNB exposure, in order to obtain time-lapse images (500 ms time interval for 1 min), the cells were incubated in a 20 mM HBSS/HEPES buffer containing fluorescent dye (100 nM TMRM (Tetramethyl Rhodamine Methyl Ester)) for 15 min. The excitation and emission wavelengths were 560 nm and 607 nm, respectively. To limit photobleaching of the dye, laser intensity was controlled at 13.5 μW for 50 ms. With this setup, wide-field images were captured using a 100x oil immersion objective. The experimental data analyzed in Section 2.3.2 were collected in collaboration with Ms. Laura Maurer (PhD candidate, Department of Toxicology, School of Public Health) and Mr. Andrew Jureziz (MPH, Department of Toxicology, School of Public Health).

For the simultaneous quantification of mitochondrial membrane potential and morphology in Section 2.3.1, cells were exposed to 400 μM 1,3-DNB for 2 hours. Since the fluorescence intensity of TMRM depends on mitochondrial membrane potential, the

mitochondrial morphology may be inaccurately captured when a mitochondrion lose its membrane potential. To resolve this problem, we used MTDR (MitoTracker Deep Red) because its fluorescence intensity does not depend on mitochondrial membrane potential. To alternately capture the images from TMRM and MTDR, the cells were incubated in a 20 mM HBSS/HEPES buffer containing 100 nM TMRM and 100 nM MTDR for 15 min.

2.2.2. Image processing and quantification of mitochondrial properties
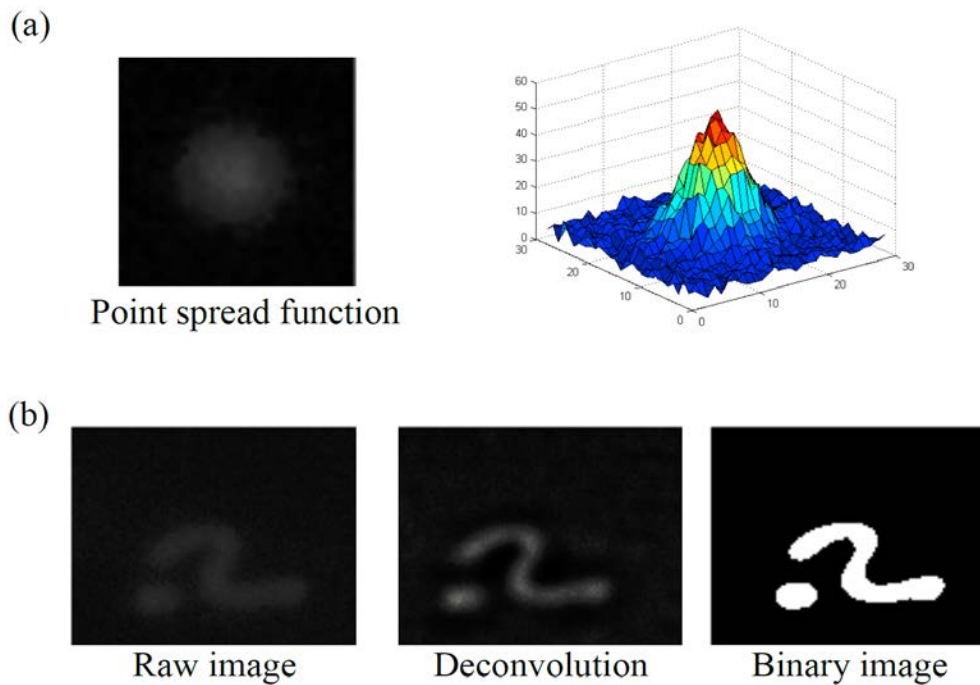
Figure 2.1. Image processing procedures. (a) Image of the experimentally measured point spread function. (b) An example of the image processing result.

At each set of images, mitochondrial properties including the aspect ratio and membrane potential were quantified, and the existence of mitochondria showing major membrane potential fluctuation (i.e., flickering) was examined.

To define the boundaries of mitochondria, raw images were converted to binary images using MATLAB (R2010a). Fig. 2.1 shows the image processing procedure for obtaining the binary image from the raw image. First, gray values of TMRM fluorescence intensities were linearly transformed to cover the entire 8 bit gray scale (0-255). These images were then deblurred using the 'deconvblind' function. The experimentally measured point spread function (PSF) was applied as an initial PSF for this deconvolution process [19, 27-29]. A Gaussian low pass filter with size 100 and standard deviation 1.33 was applied to smoothen the edge of the boundary. Finally, these images were converted to the binary images using Otsu's method [30].

Conventionally, the aspect ratio of a mitochondrion is measured as the ratio between major and minor axis lengths of the ellipse equivalent to the mitochondrial shape (Fig. 2.2(a)). These conventional quantification methods, however, may not accurately quantify heterogeneous shapes of mitochondria. As illustrated in Fig. 2.2(a), by using the conventional method, mitochondria with clearly different morphologies can have the same aspect ratio. To resolve this problem, we redefined the mitochondrial aspect ratio. As can be seen in Fig. 2.2(b), the centerline of a mitochondrion was extracted from the binary image using a morphological thinning operation in MATLAB ('bwmorph' function with 'thin' operation). After the thinning operation, the endpoints of the centerline were connected to the boundary of a mitochondrion to complete the centerline.

The average width of a mitochondrion was then calculated as area divided by centerline length.

$$\text{average width} = \frac{\text{area}}{\text{centerline length}} \quad (2.1)$$

The aspect ratio was defined as the ratio between centerline length and average width (multiply by $\pi/4$ allows the aspect ratio of a circle to be 1).

$$AR = \frac{\pi}{4} \frac{\text{centerline length}}{\text{average width}} \quad (2.2)$$

(a)

(b)
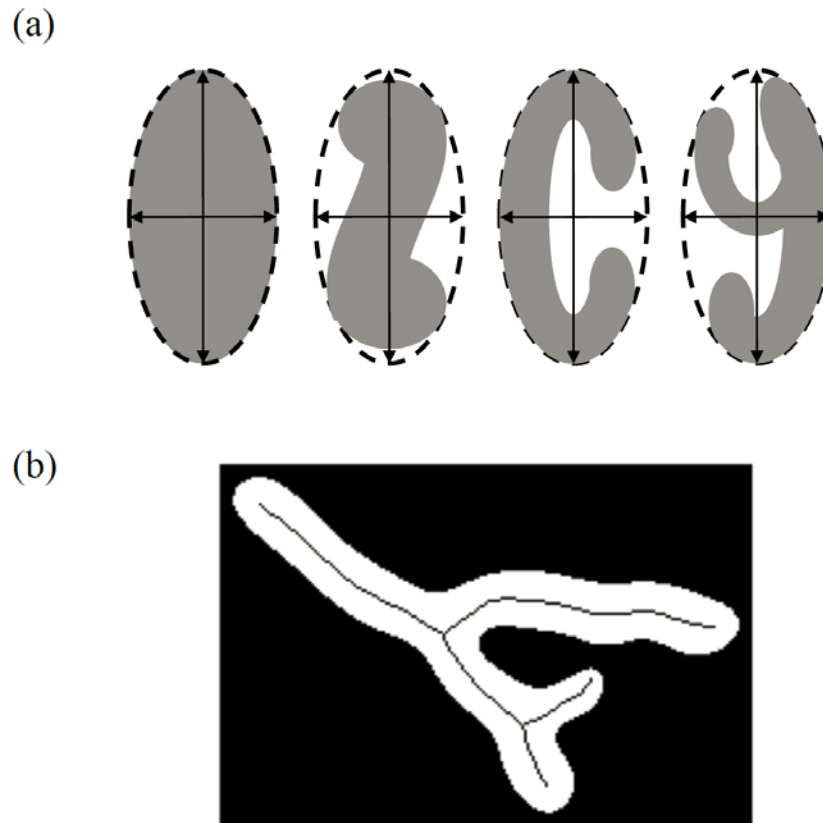
Figure 2.2. (a) Illustration of the problem in the conventional morphology quantification method. (b) Morphology quantification of a branched mitochondrion achieved by applying the method introduced in this study.

Next, we quantified mitochondrial membrane potential from TMRM images. For this membrane potential quantification, we applied the method developed by Fink et al. [19]. Individual mitochondrial images were extracted from the binary images and used as masks. The average TMRM fluorescence intensity inside a mitochondrion (F_{mit}) and the average fluorescence intensity of background (F_{cyt}) were measured. Finally, mitochondrial membrane potential ($\Delta\Psi_m$) was calculated from the following modified Nernst equation [19].

$$\Delta\Psi_m(\text{mV}) = -60\log_{10}(C\frac{F_{mit}}{F_{cyt}}), \tag{2.3}$$

where C is a correction factor (C=7.6).

2.2.3. Treatment of mitochondrial permeability transition inhibitors

The observed mitochondrial membrane potential disruption and morphological change may be related to the opening of permeability transition pores. To test this hypothesis, we treated cells with drugs that can inhibit the mitochondrial permeability transition. Since bongkrekic acid (BKA) and cyclosporine A (CSA) are well-known inhibitors of the mitochondrial permeability transition [31-33], we prepared cells with the following four treatments: i) cells were exposed to 600 uM 1,3-DNB for 5 hours ('DNB' treatment), ii) cells were pretreated with 5 uM Bongkrekic acid for 30 min and then exposed to 600 uM 1,3-DNB for 5 hours ('BKA' treatment), iii) cells were pretreated with 1 uM Cyclosporin A for 30 min and then exposed to 600 uM 1,3-DNB for 5 hours ('CSA' treatment), and iv) cells were exposed to the same amount of DMSO (Dimethyl

sulfoxide) used for delivering 1,3-DNB ('vehicle control (VC)' treatment). We conducted 120 sets of experiments (N=30 for each treatment). Finally, the images were obtained with the same setup described in Section 2.2.1. In addition to TMRM fluorescence images, bright field images were captured to identify the boundaries of a cell membrane and a nucleus.

In order to compare the difference between the treatments, the mean aspect ratio and the number of mitochondria per cell were calculated. In addition, the position of mitochondria with respect to the nucleus was quantified.
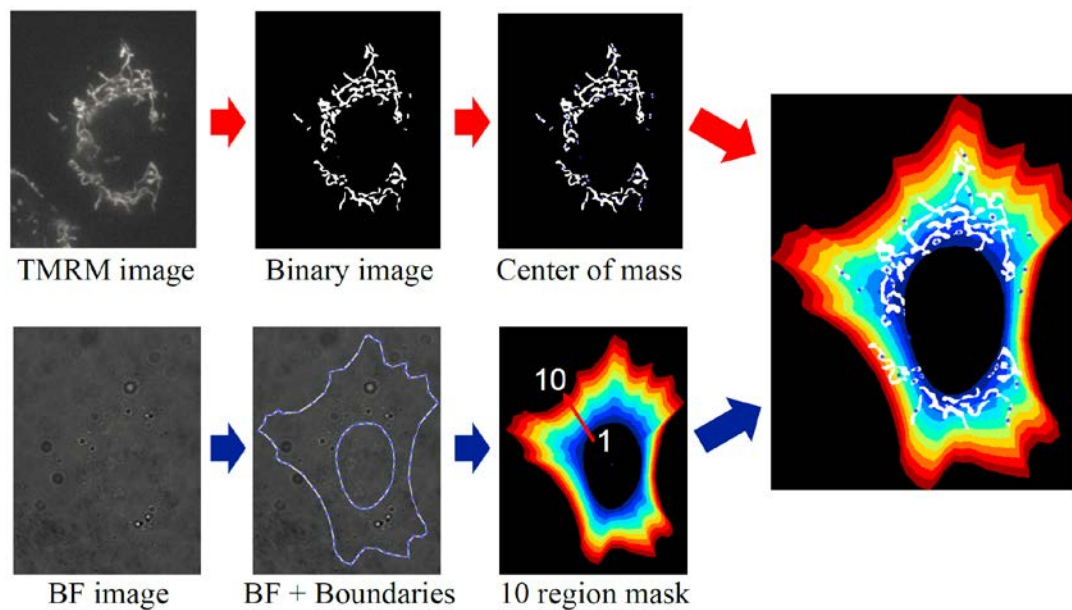
Figure 2.3. Image processing for the quantification of mitochondrial position.

As can be seen in Fig. 2.3, a TMRM fluorescence image was first converted to the binary image. Then this binary image was numerically labeled to identify each

mitochondrion. The center of mass of each mitochondrion was calculated from the labeled image. In the meantime, the boundaries of the cell and the nucleus were manually drawn from the bright field image. We processed this image of the boundaries in order to obtain equidistant lines that divide the area between the cell boundary and the nucleus boundary into 10 regions. These regions were numbered from 1 to 10, where 1 is closest to the center of the nucleus and 10 is farthest. Finally, the position of each mitochondrion was quantified by two parameters: i) the distance from the centers of the nucleus and ii) the region number where the center of the mitochondrion belongs.

After quantifying the positions of mitochondria within a cell, the distribution of these mitochondrial positions was obtained from each cell. This distribution was finally parameterized by the mean (or 1st moment) and the skewness (or 3rd standardized moment).

2.2.4. Statistical analysis

All of the statistical analyses in this chapter were conducted by using R (version 2.11.1) and MATLAB (R2010a).

In Section 2.3.1, we tested the correlation between the properties (length, width, aspect ratio, fluorescence intensity, and membrane potential) of an individual mitochondrion. The percentile change of each property was calculated and plotted against the elapsed time. In particular, the fluorescence intensity representing membrane potential and the aspect ratio were normalized to have a minimum of 0 and a maximum of 1. The correlation between these two parameters was calculated by the following equation.

$$\mathrm{cor}(X,Y) = \frac{\mathrm{cov}(X,Y)}{\sigma_x \sigma_y} = \frac{\mathrm{E}[(X - \overline{X})(Y - \overline{Y})]}{\sigma_x \sigma_y}, \tag{2.4}$$

where X and Y are the normalized fluorescence intensity and aspect ratio, respectively; σ_x and σ_y are the standard deviations of X and Y, respectively; and $\overline{X}$ and $\overline{Y}$ are the mean values of X and Y, respectively.

In Section 2.3.2, the statistical significance of the respective effects of 1,3-DNB concentration, exposure time, and cell passage on mitochondrial morphology and membrane potential was tested. First, the mean aspect ratio (AR) representing the morphology of a mitochondrial population was calculated from each image. Linear regression with log transformation was used to check the respective statistical significance of 1,3-DNB concentration, exposure time, and cell passage on the mean AR.

$$\mathrm{mean\ AR} = \beta_0 + \beta_1 \log x_1 + \beta_2 \log x_2 + \beta_3 \log x_3, \tag{2.5}$$

where x_1 is 1,3-DNB concentration, x_2 is exposure time, and x_3 is cell passage. The ordinary least square method was used to calculate the estimated value of each coefficient and its p-value. On the other hand, the statistical significance of the probability of flickering was examined using the probit regression model because flickering is a dichotomous measure.

$$\mathrm{Prob(flickering)} = \Phi(\beta_0 + \beta_1 x_1 + \beta_2 x_2 + \beta_3 x_3), \tag{2.6}$$

where Φ is a cumulative distribution function of the standard normal distribution, x_1 is 1,3-DNB concentration, x_2 is exposure time, and x_3 is passage group (stratified into two groups: young cell (4−8) and old cell (9−30)). To compare the results from the probit regression model with the actual data, the probability was calculated by binning the x-axis of the plot.

$$\text{Prob(flickering} \mid a \leq z < \text{b)} = \frac{\text{number of flickering events when a} \leq z < \text{b}}{\text{number of total events when a} \leq z < \text{b}}, \qquad (2.7)$$

where $z = \beta_0 + \beta_1 x_1 + \beta_2 x_2 + \beta_3 x_3$.

In Section 2.3.3, we compared the mean aspect ratio and the number of mitochondria per cell obtained from 4 different treatments ('VC', 'DNB', 'BKA', and 'CSA'). For this analysis, we used one-way ANOVA (analysis of variance) where the null hypothesis is that there is no difference between the treatments. In this section, we also analyzed the distribution of mitochondria within a cell. This distribution was quantified by the mean and skewness of the distribution. The statistical significance of the difference between these parameters was also tested by using one-way ANOVA.

2.3. RESULTS

In this section, we first investigate the correlation between mitochondrial properties by tracking individual mitochondria. The average properties of the mitochondrial population are then analyzed under different 1,3-DNB exposure conditions. Finally, the effects of mitochondrial permeability transition inhibitors on these mitochondrial properties are examined.

2.3.1. Correlation between mitochondrial morphology and membrane potential in individual mitochondria

To investigate the relationship between the change in mitochondrial morphology and membrane potential fluctuation under 1,3-DNB exposure, we simultaneously quantified mitochondrial properties by tracking individual mitochondria.

	0 sec	11	21	60	100
MTDR					
TMRM					
Image Processing					
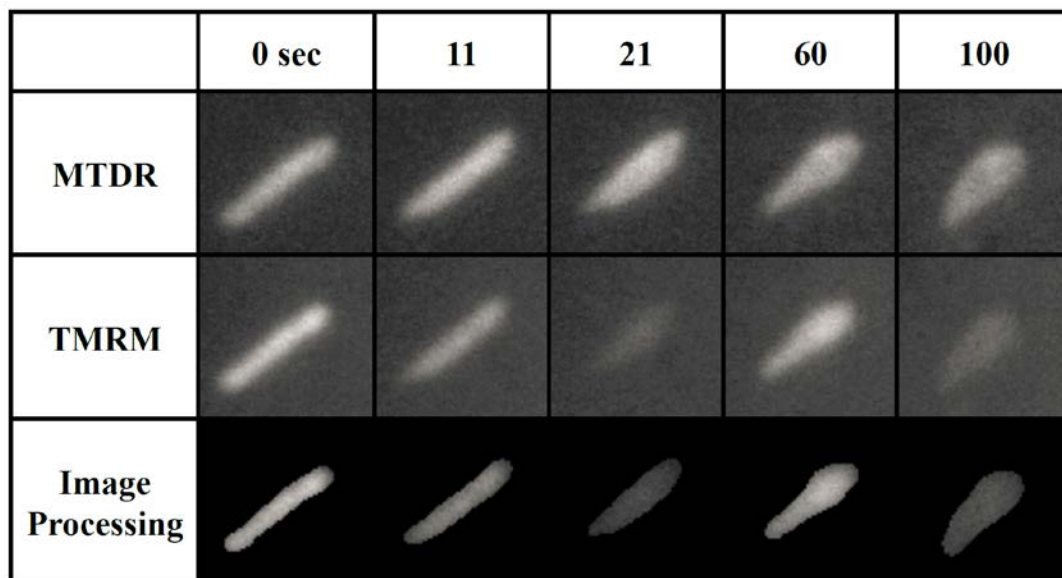
Figure 2.4. Images of the selected mitochondrion showing correlated changes in mitochondrial morphology (MTDR images) and membrane potential (TMRM images).

Fig. 2.4 shows an example of images obtained from MTDR, TMRM, and image processing. We found that the morphological change of mitochondria was associated with membrane potential fluctuation. At 21 sec, accompanied by the morphological change (swollen mitochondrion), the membrane potential of the mitochondrion was abruptly dropped and then recovered. We quantified these changes in mitochondrial properties as described in Section 2.2.2.
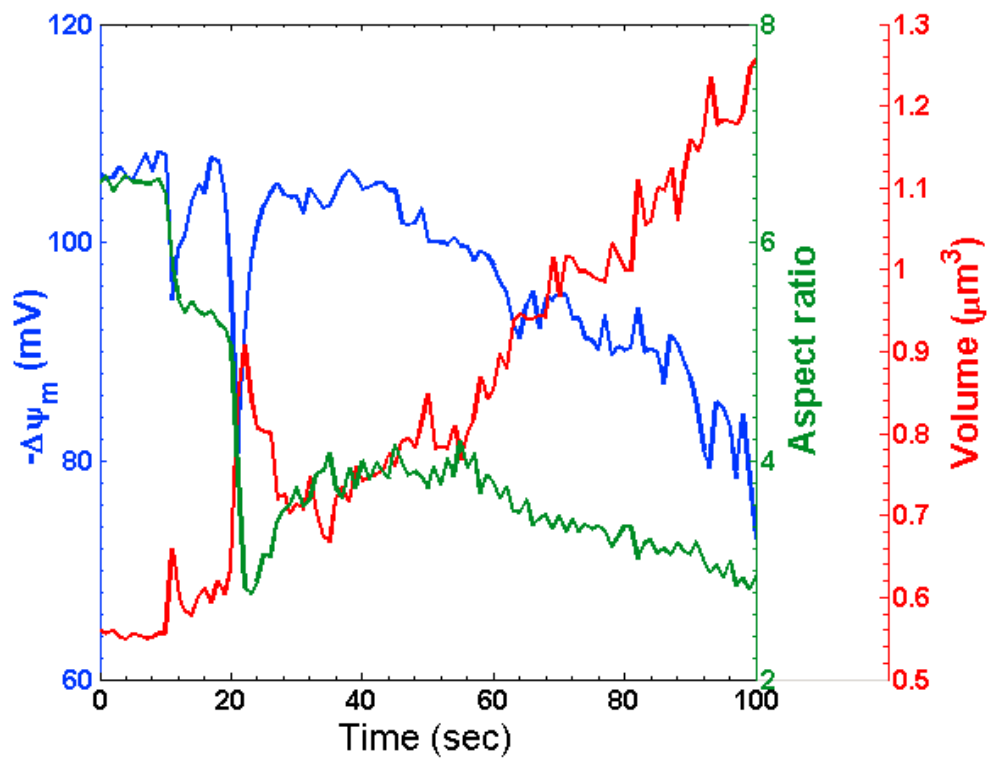
Figure 2.5. Simultaneous quantification of mitochondrial properties (mitochondrial membrane potential, aspect ratio, and volume).

As can be seen in Fig. 2.5, two major fluctuations of the membrane potential that occurred at 11 and 21 sec coincided with the steep drops of the aspect ratio and the fluctuations of volume. After the major fluctuations, the membrane potential and the aspect ratio gradually decreased, while the volume increased. Finally, the mitochondrion was entirely swollen and lost its membrane potential.

In order to further confirm this relationship, we selected 16 mitochondria showing membrane potential disruption and analyzed their properties. The percentile changes of

the properties of these mitochondria were measured to calculate the correlation between the fluorescence intensity and the aspect ratio. The results are summarized in Table 2.1. The average correlation between the fluorescence intensity (which depends on the membrane potential) and the aspect ratio was 0.80, and the standard deviation was 0.13. These results support our hypothesis that the change in mitochondrial morphology is closely related to the membrane potential fluctuation.

Table 2.1. Correlation between mitochondrial morphology and membrane potential

Index #	% change of morphology			% change of fluorescence intensity (FI)	Correlation between FI and AR	
	Length	Width	AR		cor (FI, AR)	p-value
1	32.3	43.8	61.4	59.2	0.72	1.4e-6
2	47.7	26.2	57.7	88.1	0.74	5.9e-07
3	33.9	23.7	46.8	76.5	0.92	3.2e-14
4	40.7	33.3	55.5	59.4	0.42	0.013
5	46.4	30.9	60.9	61.7	0.89	1.5e-12
6	44.2	51.5	64.3	63.9	0.94	1.7e-16
7	41.9	28.4	58.0	53.7	0.93	8.5e-16
8	38.4	35.3	59.7	79.3	0.68	8.6e-06
9	17.2	20.5	30.5	59.0	0.72	1.5e-06
10	34.6	33.0	53.5	51.3	0.82	2.4e-09
11	41.9	32.9	56.7	57.4	0.90	6.9e-13
12	35.9	21.3	48.5	62.2	0.81	5.2e-09
13	29.9	21.4	43.1	50.0	0.77	1.2e-07
14	36.5	31.8	47.1	50.1	0.86	7.8e-11
15	35.9	30.9	49.7	54.6	0.86	4.4e-11
16	29.8	31.9	49.5	52.4	0.75	3.3e-07

2.3.2. Effects of 1,3-DNB on mitochondrial properties

Changes in mitochondrial properties such as fragmented and swollen morphologies and loss of membrane potential have been experimentally observed. Fig. 2.6 shows an example of alterations in mitochondrial properties induced by 1,3-DNB. Before 1,3-DNB exposure, mitochondria were mostly elongated tubules that formed interconnected networks. On the other hand, fragmented and swollen mitochondria were observed after 1,3-DNB exposure. Moreover, in many 1,3-DNB exposed cells, very weak fluorescence of TMRM was detected.
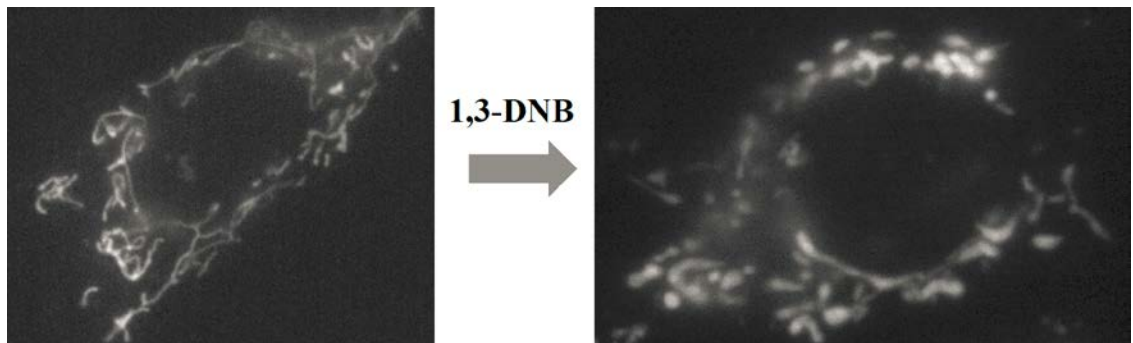
Figure 2.6. Changes in mitochondrial properties after 5 hours of 600 μM 1,3-DNB exposure.

In addition to these observations, we hypothesized that the alterations in mitochondrial morphology and membrane potential may be initiators of mitochondrial dysfunction. Thus, we further investigated the respective effects of 1,3-DNB concentration, exposure time, and cell passage on the mitochondrial morphology and membrane potential fluctuation by using statistical analysis.
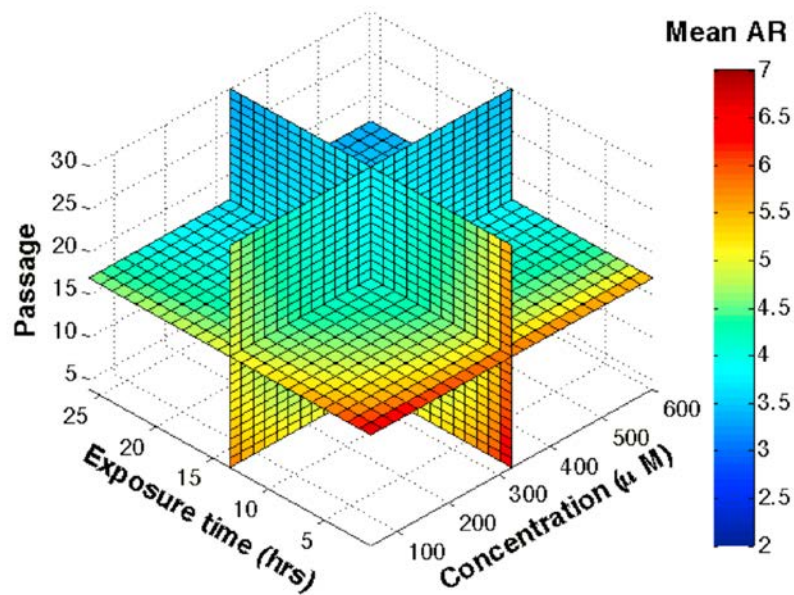
Figure 2.7. Response surface of linear regression model for mean aspect ratio.

Fig. 2.7 shows the effects of 1,3-DNB concentration, exposure time, and cell passage on the mean aspect ratio. The experimental results obtained from image processing were fitted to the linear regression model (Eq. 2.5). As expected, both 1,3-DNB exposure and cell passage induced a significant decrease in the mean aspect ratio. The estimated values of β_0, β_1, β_2, and β_3 were 10.0464, -0.4956, -0.6542, and -0.5151, respectively. From the statistical analysis, we confirmed that all of these coefficients are statistically significant (p-values of β_0, β_1, β_2, and β_3 were 5.4e-11, 0.003, 0.0002, and 0.008, respectively). However, because of the intrinsically high cell-to-cell variation, a discrete change of the mean aspect ratio, which may indicate the initiation point of

mitochondrial dysfunction, was not observed. This high variation also resulted in a low R-square value (0.0823) of the fitted model.
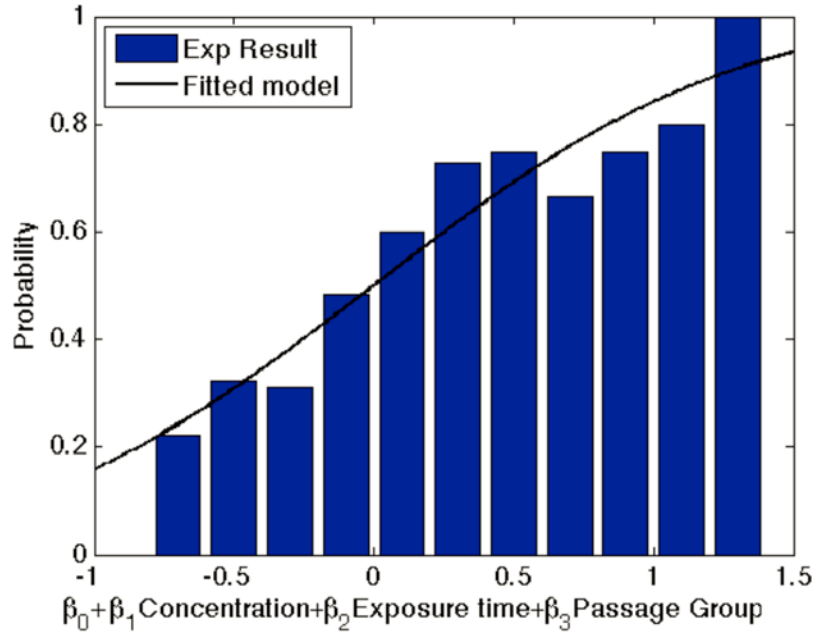
Figure 2.8. Probability of flickering estimated from the probit regression model and experiment.

We hypothesized that major fluctuation (or disruption) in mitochondrial membrane potential (i.e., flickering) may also represent the initiation of mitochondrial dysfunction. Therefore, the effects of 1,3-DNB and cell passage on the probability of flickering were investigated. The statistical significance of each independent variable was calculated using the probit regression model (Eq. 2.6).

As can be seen in Fig. 2.8, the probability of flickering increased as 1,3-DNB concentration, exposure time, and cell passage increased (β_0=-2.0461, β_1=0.0696,

33

β_2=0.0031, and β_3=1.0739). The probit regression model suggested that this positive correlation between the probability of flickering and each independent variable is statistically significant (p-values of β_0, β_1, β_2, and β_3 were 0.0007, 0.0003, 0.015, and 0.0005, respectively). Even though we showed that the effects of 1,3-DNB and passage on the membrane potential disruption were statistically significant, the abrupt increase in the probability was not observed. Therefore, it is not yet conclusive whether flickering may be an initiator of mitochondrial dysfunction.

2.3.3. Effects of mitochondrial permeability transition inhibitors

Since the mitochondrial permeability transition may be the underlying mechanism of the alterations in mitochondrial properties, we examined the effects of mitochondrial permeability transition inhibitors on mitochondrial properties. As explained in Section 2.2.3, we analyzed mitochondria from four different treatments: VC, DNB, BKA, and CSA.

First, the mean aspect ratios of mitochondria from the VC, DNB, BKA, and CSA treatment were compared (Fig. 2.9(a)). The one-way ANOVA results showed that the mean aspect ratios of the DNB, BKA, and CSA treatments were significantly smaller than that of the VC treatment (p-value=1.3e-7). However, the inhibition of the opening of the mitochondrial permeability transition pores did not restrain the changes in the mitochondrial morphology induced by 1,3-DNB exposure because the difference among the DNB, BKA, and CSA treatments were not statistically significant (p-value=0.81).

Moreover, as can be seen in Fig. 2.9(b), the number of mitochondria per cell did not show significant differences between the treatments (p-value=0.93).
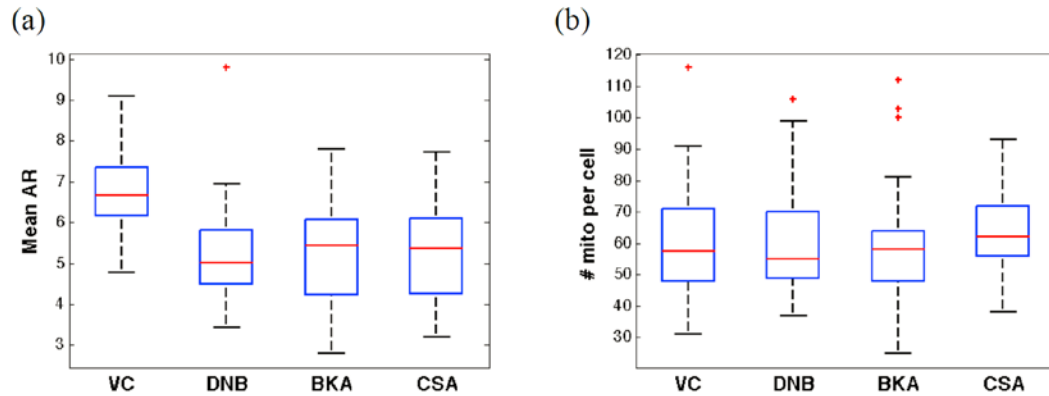
Figure 2.9. The effects of the treatments on the mean aspect ratio and the number of mitochondria per cell. (a) The mean aspect ratios of mitochondria from the different treatments. (b) The numbers of mitochondria per cell from the different treatments.

We further investigated the effects of the treatments by comparing the mitochondrial position distributions. Mean region numbers of mitochondria from the DNB, BKA, and CSA treatments were significantly smaller than that from the VC treatment (p-value=0.0043). This result implies that mitochondria were more concentrated near the nucleus when cells were exposed to 1,3-DNB. However, the difference among the DNB, BKA, and CSA treatments were not statistically significant (p-value=0.60), and the skewness did not show a significant difference (p-value=0.73).
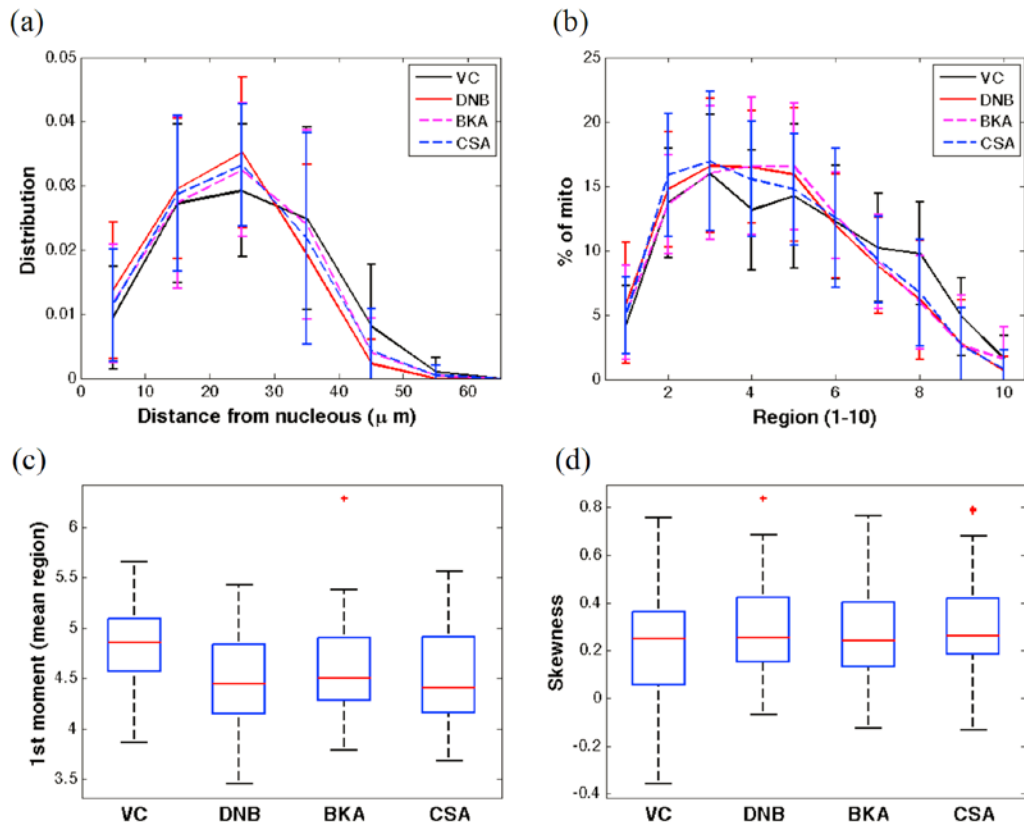
Figure 2.10. The effects of the treatments on mitochondrial position distribution. (a) Mitochondrial position distributions quantified by the distance from the center of the nucleus. (b) Mitochondrial position distributions quantified by the region number (1 is the closest to the center and 10 is the farthest from the center). (c) Mean region numbers of the mitochondrial position distributions. (d) Skewnesses of the mitochondrial position distributions.

2.4. DISCUSSION

In this section, we discuss the limitations in our imaging and image processing techniques and data analysis.

The accuracy of mitochondrial property quantification was restricted by the limitations in the imaging and image processing techniques. Firstly, since the 2D wide-field images were captured and used for the analysis, we did not have sufficient 3D information for differentiating the overlapped mitochondria from branched mitochondria. This limitation can cause inaccuracies in morphological quantification because branched mitochondria generally have higher aspect ratios.

Moreover, with this 2D imaging technique, vertically drifting mitochondria can be confused with flickering mitochondria because it is very difficult to distinguish the loss of fluorescence caused by the actual membrane potential disruption from that caused by the drifting of mitochondria above and below the focal plane.

Additionally, mitochondria with low membrane potential could not be included in our analysis because we used fluorescent dyes only capable of capturing images of viable mitochondria. This inability to capture the entire population of mitochondria limits the analysis of unhealthy or dying mitochondria under neurotoxin exposures.

The data analysis methods applied in this study also have limitations. In Section 2.3.1, we calculated the correlation between the fluorescence intensity and the aspect ratio when a mitochondrion underwent a major membrane fluctuation. However, the critical degree (or amplitude) of the major fluctuation could not be strictly defined, because the initial fluorescence intensities of mitochondria varied widely.

In Section 2.3.2, we tested the respective statistical significance by using the linear regression model and the probit regression model. However, functional forms for the response models of both the mean aspect ratio and the probability of flickering (with

respect to 1,3-DNB concentration, exposure time, and cell passage) are unavailable in the literature. Instead, these response models were based only on fitting experimental results.

Even though our data analyses demonstrated that the effects of 1,3-DNB on mitochondrial properties are statistically significant, threshold values, which can be used to differentiate the disease state from the normal state, were not defined. Because the objective of this study is to investigate mitochondrial properties as indicators (or initiators) of mitochondrial dysfunction, further investigation on the existence of these threshold values is required. Therefore, the imaging and image processing techniques and the data analysis method need to be improved in order to handle the data with intrinsically high levels of variation.

2.5. CONCLUSIONS

The abnormal mitochondrial properties have been studied as indicators of CNS diseases. However, the existing literature has not sufficiently provided quantitative relationships between the properties of mitochondria and their functions under different disease states.

In this study, we quantitatively investigated the changes in mitochondrial properties under 1,3-DNB exposure. By adding the MTDR, we simultaneously quantified the morphology and membrane potential of mitochondria. For more precise estimation of heterogeneous mitochondrial morphologies, we redefined the aspect ratio. Finally, the statistical significance was tested by using linear and probit regression models and one-way ANOVA.

From the image processing and data analysis results, we found that major membrane potential fluctuations coincided with the morphological changes (steep drops of the aspect ratio and the fluctuations of volume). In addition, we showed that the respective effects of 1,3-DNB concentration, exposure time, and cell passage on both the mean aspect ratio and the membrane potential disruption were statistically significant. Finally, the mitochondrial permeability transition inhibitors, such as bongkrekic acid and cyclosporine A, could not prevent the property alterations induced by 1,3-DNB.

Even though our results quantitatively presented the effects of 1,3-DNB on the properties of mitochondria, the existence of the threshold values determining the initiation of mitochondrial dysfunction has not been fully investigated. This objective may be achieved by the improvement in the imaging and image processing techniques as well as the data analysis methods.

2.6. BIBLIOGRAPHY

1.   M. Karbowski, and R. Youle, Dynamics of mitochondrial morphology in healthy cells and during apoptosis. *Cell Death & Differentiation* 10, 870 (2003).
2.   R. J. Youle, and M. Karbowski, Mitochondrial fission in apoptosis. *Nature reviews Molecular cell biology* 6, 657 (2005).
3.   D. C. Chan, Mitochondria: dynamic organelles in disease, aging, and development. *Cell* 125, 1241 (2006).
4.   A. C. Bowling, and M. F. Beal, Bioenergetic and oxidative stress in neurodegenerative diseases. *Life sciences* 56, 1151 (1995).
5.   K. Hirai, G. Aliev, A. Nunomura, H. Fujioka, R. L. Russell, C. S. Atwood, A. B. Johnson, Y. Kress, H. V. Vinters, and M. Tabaton, Mitochondrial abnormalities in Alzheimer's disease. *The Journal of neuroscience* 21, 3017 (2001).
6.   R. Castellani, K. Hirai, G. Aliev, K. L. Drew, A. Nunomura, A. Takeda, A. D. Cash, M. E. Obrenovich, G. Perry, and M. A. Smith, Role of mitochondrial dysfunction in Alzheimer's disease. *Journal of Neuroscience Research* 70, 357 (2002).
7.   A. Eckert, U. Keil, C. A. Marques, A. Bonert, C. Frey, K. Schüssel, and W. E. Müller, Mitochondrial dysfunction, apoptotic cell death, and Alzheimer's disease. *Biochemical pharmacology* 66, 1627 (2003).
8.   P. H. Reddy, and M. F. Beal, Are mitochondria critical in the pathogenesis of Alzheimer's disease? *Brain research reviews* 49, 618 (2005).
9.   J. Yao, R. W. Irwin, L. Zhao, J. Nilsen, R. T. Hamilton, and R. D. Brinton, Mitochondrial bioenergetic deficit precedes Alzheimer's pathology in female mouse model of Alzheimer's disease. *Proceedings of the National Academy of Sciences* 106, 14670 (2009).
10. P. Keane, M. Kurzawa, P. Blain, and C. Morris, Mitochondrial dysfunction in Parkinson's disease. *Parkinson's disease* 2011, (2011).
11. P. A. Trimmer, R. H. Swerdlow, J. K. Parks, P. Keeney, J. P. Bennett, S. W. Miller, R. E. Davis, and W. D. Parker, Abnormal mitochondrial morphology in sporadic Parkinson's and Alzheimer's disease cybrid cell lines. *Experimental Neurology* 162, 37 (2000).
12. M. S. Parihar, and G. J. Brewer, Simultaneous age-related depolarization of mitochondrial membrane potential and increased mitochondrial reactive oxygen species production correlate with age-related glutamate excitotoxicity in rat hippocampal neurons. *Journal of Neuroscience Research* 85, 1018 (2007).
13. K. F. Winklhofer, and C. Haass, Mitochondrial dysfunction in Parkinson's disease. *Biochimica et Biophysica Acta (BBA)-Molecular Basis of Disease* 1802, 29 (2010).
14. X. Wang, B. Su, H.-g. Lee, X. Li, G. Perry, M. A. Smith, and X. Zhu, Impaired balance of mitochondrial fission and fusion in Alzheimer's disease. *The Journal of neuroscience* 29, 9090 (2009).
15. R. B. Tjalkens, A. D. Phelka, and M. A. Philbert, Regional variation in the activation threshold for 1, 3-DNB-induced mitochondrial permeability transition in brainstem and cortical astrocytes. *Neurotoxicology* 24, 391 (2003).

16. A. D. Phelka, M. M. Sadoff, B. P. Martin, and M. A. Philbert, BCL-XL expression levels influence differential regional astrocytic susceptibility to 1, 3-dinitrobenzene. *Neurotoxicology* 27, 192 (2006).

17. S. R. Steiner, and M. A. Philbert, Proteomic identification of carbonylated proteins in 1, 3-dinitrobenzene neurotoxicity. *Neurotoxicology* 32, 362 (2011).

18. L. M. Loew, R. A. Tuft, W. Carrington, and F. S. Fay, Imaging in five dimensions: time-dependent membrane potentials in individual mitochondria. *Biophysical Journal* 65, 2396 (1993).

19. C. Fink, F. Morgan, and L. M. Loew, Intracellular fluorescent probe concentrations by confocal microscopy. *Biophysical Journal* 75, 1648 (1998).

20. J. J. Lemasters, D. R. Trollinger, T. Qian, W. E. Cascio, and H. Ohata, Confocal imaging of Ca^{2+}, pH, electrical potential, and membrane permeability in single living cells. *Methods in Enzymology* 302, 341 (1999).

21. S. Nakayama, T. Sakuyama, S. Mitaku, and Y. Ohta, Fluorescence imaging of metabolic responses in single mitochondria. *Biochemical and Biophysical Research Communications* 290, 23 (2002).

22. G. Solaini, G. Sgarbi, G. Lenaz, and A. Baracca, Evaluating mitochondrial membrane potential in cells. *Bioscience reports* 27, 11 (2007).

23. F. Distelmaier, W. J. H. Koopman, E. R. Testa, A. S. de Jong, H. G. Swarts, E. Mayatepek, J. A. M. Smeitink, and P. H. G. M. Willems, Life cell quantification of mitochondrial membrane potential at the single organelle level. *Cytometry Part A* 73A, 129 (2008).

24. W. J. H. Koopman, F. Distelmaier, J. J. Esseling, J. A. M. Smeitink, and P. H. G. M. Willems, Computer-assisted live cell analysis of mitochondrial membrane potential, morphology and calcium handling. *Methods* 46, 304 (2008).

25. A. Kaasik, D. Safiulina, V. Choubey, M. Kuum, A. Zharkovsky, and V. Veksler, Mitochondrial swelling impairs the transport of organelles in cerebellar granule neurons. *Journal of Biological Chemistry* 282, 32821 (2007).

26. W. Song, B. Bossy, O. J. Martin, A. Hicks, S. Lubitz, A. B. Knott, and E. Bossy-Wetzel, Assessing mitochondrial morphology and dynamics using fluorescence wide-field microscopy and 3D image processing. *Methods (San Diego, Calif.)* 46, 295 (2008).

27. J. B. de Monvel, S. Le Calvez, and M. Ulfendahl, Image restoration for confocal microscopy: improving the limits of deconvolution, with application to the visualization of the mammalian hearing organ. *Biophysical Journal* 80, 2455 (2001).

28. M. Bertero, P. Boccacci, G. Desidera, and G. Vicidomini, Image deblurring with Poisson data: from cells to galaxies. *Inverse Problems* 25, 123006 (2009).

29. P. Kner, J. Sedat, D. Agard, and Z. Kam, High-resolution wide-field microscopy with adaptive optics for spherical aberration correction and motionless focusing. *Journal of microscopy* 237, 136 (2010).

30. N. Otsu, A threshold selection method from gray-level histograms. *Automatica* 11, 23 (1975).

31. N. Zamzami, P. Marchetti, M. Castedo, T. Hirsch, S. A. Susin, B. Masse, and G. Kroemer, Inhibitors of permeability transition interfere with the disruption of the

mitochondrial transmembrane potential during apoptosis. *FEBS Letters* 384, 53 (1996).

32. P. Marchetti, M. Castedo, S. A. Susin, N. Zamzami, T. Hirsch, A. Macho, A. Haeffner, F. Hirsch, M. Geuskens, and G. Kroemer, Mitochondrial permeability transition is a central coordinating event of apoptosis. *The Journal of experimental medicine* 184, 1155 (1996).

33. J. L. Scarlett, P. W. Sheard, G. Hughes, E. C. Ledgerwood, H.-H. Ku, and M. P. Murphy, Changes in mitochondrial membrane potential during staurosporine-induced apoptosis in Jurkat cells. *FEBS Letters* 475, 267 (2000).

CHAPTER 3

BIOPHYSICAL SIGNIFICANCE OF THE INNER MITOCHONDRIAL MEMBRANE STRUCTURE ON THE ELECTROCHEMICAL POTENTIAL OF MITOCHONDRIA[1]

3.1. INTRODUCTION

Mitochondria are double-membraned organelles enclosed by inner and outer membranes composed of phospholipid bilayers and proteins. The inner mitochondrial membrane (IMM) is of particular interest in that it is a major site of the electron transport chain and ATP synthase. The structure of the IMM has been extensively studied for the past decade. Advanced imaging techniques have permitted researchers to visualize the various components of mitochondrial structure. The IMM is composed of the inner boundary membrane (IBM) and the crista membrane (CM). Cristae are the involuted structures of the IMM that form tubules or lamellae. The CM and the IBM are connected via narrow tubular sites called crista junctions [1]. It is hypothesized that the role of crista morphology is to increase the surface area of the IMM to enable greater capacity for oxidative phosphorylation, whereas the morphologies of crista junctions have been

---

[1] Material in this chapter is a submitted paper: D. H. Song, L. L. Maurer, J. Park, W. Lu, M. A. Philbert, and A. M. Sastry, Biophysical significance of the inner mitochondrial membrane structure on the electrochemical potential of mitochondria. *Biophysical Journal* (2013).

studied and characterized as merely a molecular diffusion barrier [2-4]. Recent studies have shown that the IMM structures can differ widely among different cell types as well as physiological and pathological conditions. Therefore, investigating the mechanistic and functional effects of these pleomorphic IMM structures is a crucial step in understanding the progression of mitochondrial function and dysfunction.

Experimental studies have investigated the IMM structure in relation to the energy state and disease state of mitochondria. Using electron tomography, two different morphologies of the IMM have been observed in mitochondria at different energy states [5-7]. Mitochondria with high respiratory activity (state III) contain enlarged cristae, while those with low respiratory activity (state IV) have small cristae. In addition to these studies, more decisive and detrimental changes in the IMM structures were observed from mitochondria in neurodegenerative diseases. For example, swollen mitochondria and loss of cristae are seen in Parkinson's diseases [8], and swollen mitochondria with degenerated cristae are observed in Huntington's disease [9]. However, these studies provide only a qualitative description of the morphological changes. Morphometric analyses of the IMM structure, on the other hand, may provide more concrete criteria for differentiating the multiplicity of known disease states from normal function.

Despite providing compelling evidence that the IMM structure is closely related to mitochondrial function, experimental studies have not yet successfully explained how changes in the IMM structure alter the energetic function of mitochondria. The answer to this question requires estimations of both the electric potential and the difference in proton concentration across the IMM (that are driving forces for ATP synthesis) in different IMM structures. To date, mitochondrial membrane potential and proton

concentration have been experimentally measured primarily by the use of potentiometric fluorescent dyes [10-17]. However, limitations such as diffusion and optical resolution of structures smaller than the wavelength of light prevent other than the measurement of bulk proton concentrations and electric potential and make impossible the direct measurement of local variations of these properties along irregular IMM surfaces. Mathematical simulations are, therefore, an excellent adjunct to the observations made by conventional fluorescence microscopy and aid in a better understanding of the effects of the IMM morphology on mechanistic function. For example, a thermodynamic model of the tubular cristae was developed to examine changes in free energy induced by different morphology and composition of the membrane [18]. Later, this model was modified to explain observed morphologies of cristae by considering tensile force and shape entropy [19]. The effect of cristae geometry on diffusion was investigated using Monte Carlo simulations with simplified geometries of tubular and lamellar cristae [20]. However, simulation studies have not sufficiently investigated the most important role of the IMM structure: the effect of the IMM structure on the electrochemical potential (or ATP synthesis) of mitochondria.

In this study, we introduce a model simulating the distributions of the electric potential and proton concentration in mitochondria to investigate the relationship between the IMM structure and the energetic function of mitochondria. The electric potential and proton transport were modeled based on the coupled Poisson-Nernst-Planck equations, which have been used for modeling the electrodiffusion of ions in membranes, double layer capacitors, and solvated biomolecular systems [21-23]. This equation was applied to the mitochondrion model with simplified geometry and solved using the finite element

method. By using this model, we tested the following hypotheses: i) the proton motive force on the CM is higher than that on the IBM, ii) the morphological parameters of a crista, such as the surface area and the surface-to-volume ratio, correlate with both the proton motive force and the capacity for ATP synthesis. Finally, the biophysical significance of the simulation results and the validity of model assumptions were discussed.

3.2. METHODS

3.2.1. Structure of the mitochondrion model

A 2D axisymmetric mitochondrion model mimicking the key features of the mitochondrial compartments was constructed (Fig. 3.1). This mitochondrion model comprises three concentric spheres with a single crista. The innermost sphere and the middle sphere represent the inner side and the outer side of the IMM, respectively. As can be seen in Fig. 3.1(c), the inner side is the N side (negatively charged by electrons) and the outer side is the P side (positively charged by membrane-bound protons). The outermost sphere is the outer mitochondrial membrane (OMM). The space between the P side and the OMM is the intermembrane space (IMS). One specific element of this structure is that the IMM was modeled as a domain (volume), while the OMM was modeled as a boundary (surface). The IMM is composed of the crista membrane (CM) and the inner boundary membrane (IBM). The CM is connected to the IBM through a crista junction. As can be seen in Fig. 3.1(b) and (c), the crista junction was modeled as a

46

cylinder with diameter D (30 nm) and length L (40 nm). The edges connecting the crista junction with the CM and the IBM are rounded with an inside radius of 5 nm and an outside radius of 10 nm. The N side sphere has a diameter of 1 μm. The thickness of the IMM and the IMS is 5 nm and 25 nm, respectively.
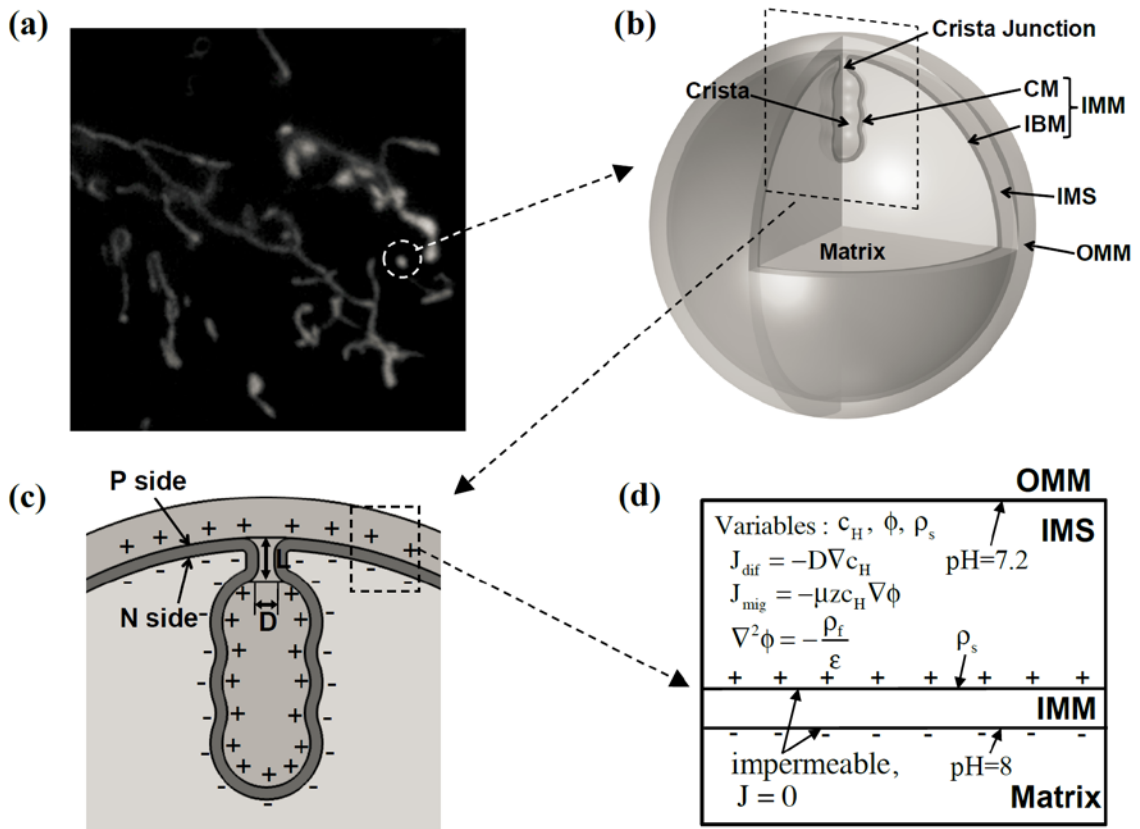
Figure 3.1. Structure of a mitochondrion model. (a) Heterogeneous morphologies of mitochondria observed in DI TNC1 cells. (b) Compartments of a mitochondrion model. (c) Cross section view of a crista in the mitochondrion model. (d) Description of proton transport model and boundary conditions (c_H is the proton concentration, ϕ is the electric potential, ρ_s is the surface charge density at the P side, ρ_f is the free charge density, and J_{dif} and J_{mig} are the diffusion flux and the migration flux, respectively). Note: The dimension in this figure is exaggerated in order to clearly illustrate of the structure.

To study the effects of overall shapes and detailed morphologies of cristae, we constructed two types of crista geometries: type I (Fig. 3.2(a)) and type II (Fig. 3.2(b)). As can be seen in Fig. 3.2(a), type I crista geometries were constructed using three parameters (r_1, r_2, and z_0). Parameters r_1 and r_2 represent the radii of the upper and lower circles of the crista structure and z_0 is the distance between the centers of these circles.
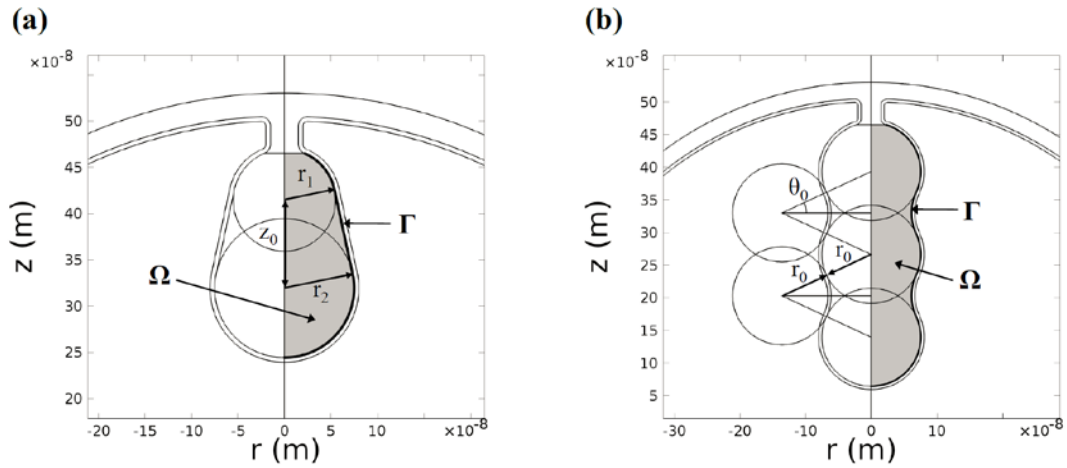
Figure 3.2. Two types of crista geometries. (a) Type I geometries were used for studying the effect of the overall crista shape. (b) Type II geometries were used to investigate the effect of detailed crista morphology.

To parameterize the overall shape of a crista, we defined the slope of the lateral surface of a crista as follows:

$$k \equiv (r_2 - r_1)/z_0 .$$ (3.1)

A positive value of k forms a narrow opening and a wide end of the crista structure, while a negative value of k forms a reversed shape. To investigate the effect of k on the electrochemical potential of a crista, we constructed three geometry groups, each with

different surface area and volume (Table 3.1). For each group, we generated a reference geometry whose $k=0$ ($r_1=r_2$). Within each group, we varied k from -0.25 to 0.25 with increments of 0.05. To solve for r_1, r_2, and z_0 at a given k, we first calculated the surface area and the volume of the reference geometry.

$$\text{Surface area} = \iint_{\text{P side CM}} dA = \int_{\Gamma} 2\pi r ds, \tag{3.2}$$

$$\text{Volume} = \iiint_{\text{crista}} dV = \iint_{\Omega} 2\pi r dA, \tag{3.3}$$

where Γ and Ω are the bold line and the shaded area in Fig. 3.2, respectively. From Eqs. 3.1, 3.2, and 3.3, we found solutions for r_1, r_2, and z_0 at the given surface area, volume and k.

$$\begin{aligned}
\text{Surface area} &= \iint_{\text{P side CM}} dA = \int_{\Gamma} 2\pi r ds \\
&= 2\pi r_1^2 (a-k) + \pi z_0 b^2 (r_1 + r_2) + 2\pi r_2^2 (1+k),
\end{aligned}$$

$$\begin{aligned}
\text{Volume} &= \iiint_{\text{crista}} dV = \iint_{\Omega} 2\pi r dA \\
&= \pi r_1^3 (a - \frac{1}{3}a^3 - k + \frac{1}{3}k^3) + \frac{\pi}{3}b^2(r_1^2 + r_1 r_2 + r_2^2)(z_0 + kr_1 - kr_2) \\
&\quad + \pi r_2^3 (\frac{2}{3} + k - \frac{1}{3}k^3)
\end{aligned} \qquad ,$$

where $a = \dfrac{\sqrt{(r_1 + r_{out})^2 - (D/2 + r_{out})^2}}{r_1 + r_{out}}$, $b = \dfrac{\sqrt{z_0^2 - (r_2 - r_1)^2}}{z_0}$.

Finally, we used these parameters to construct type I crista geometries.

Table 3.1. Parameters for constructing type I geometries

Group	$k=(r_2-r_1)/z_0$	Reference geometry (k=0)	Surface area (μm^2)	Volume ($10^{-4}\ \mu m^3$)	SVR (μm^{-1})
1	$-0.25-0.25$	$r_1=r_2=50,\ z_0=30$	0.0394	7.54	52.18
2	$-0.25-0.25$	$r_1=r_2=50,\ z_0=40$	0.0425	8.33	51.03
3	$-0.25-0.25$	$r_1=r_2=50,\ z_0=50$	0.0456	9.11	50.08

To further investigate the detailed morphologies of crista structures, type II crista geometries were constructed. As can be seen in Fig. 3.2(b), the cross section of a single crista was modeled as a combination of circles. To construct cristae structures with various surface area and volume, we varied the number of circles aligned in the centerline (N_{circle}=1, 2, … , 6), the radius of the circle (r_0=30, 31, … , 65 nm), and the angle (θ_0=10, 11, … , 25°) shown in Fig. 3.2(b). The surface area and the volume of a crista were calculated using Eqs. 3.2 and 3.3.

$$\text{Surface area} = \iint_{\text{P side CM}} dA = \int_\Gamma 2\pi r ds$$
$$= 2\pi r_0^2(1+a) + N_{circle}\{4\pi r_0^2 \sin\theta_0 + 4\pi r_0(2r_0\theta_0 \cos\theta_0 - r_0 \sin\theta_0)\}\,,$$

$$\text{Volume} = \iiint_{crista} dV = \iint_\Omega 2\pi r dA$$
$$= \frac{4}{3}\pi r_0^3(\frac{1}{2}+\frac{3}{4}a-\frac{1}{4}a^3) + N_{circle}\{\frac{1}{2}\pi r_0^3(3\sin\theta_0 + \frac{\sin 3\theta_0}{3})$$
$$+2\pi r_0(4r_0^2\cos^2\theta_0 \sin\theta_0 - 2r_0^2\cos\theta_0(\frac{\sin 2\theta_0}{2}+\theta_0)$$
$$+\frac{r_0^2}{4}(3\sin\theta_0 + \frac{\sin 3\theta_0}{3})\}$$

where $a = \dfrac{\sqrt{(r_0+r_{out})^2 - (D/2+r_{out})^2}}{r_0+r_{out}}$.

To avoid high correlation between the parameters, we selected structures whose surface areas were between 0.048 and 0.052 μm^2 (Table 3.2). This allows studying respective effects of the surface area and the surface-to-volume ratio of a crista.

Table 3.2. Parameters for constructing type II geometries

N_{circle}	Number constructed	r_0 (nm)	θ_0 (°)	Surface area (μm^2)	Volume (10^{-4} μm^3)	SVR (μm^{-1})
1	3	63−65	−	0.048−0.052	10.42−11.45	45.0−46.4
2	32	47 −56	10−25	0.048−0.052	8.86−11.02	46.7−54.5
3	27	39−50	10−25	0.048−0.052	7.64−10.48	49.2−62.7
4	24	35−45	10−25	0.048−0.052	7.12−9.56	52.6−68.4
5	24	31−42	10−25	0.048−0.052	6.43−9.33	54.9−76.1
6	20	30−39	10−23	0.048−0.052	6.40−8.72	58.0−77.0

3.2.2. Model descriptions and assumptions

To study the effect of the IMM morphology on the electrochemical potential of mitochondria, we modeled proton transport that is driven by diffusion and electric field-induced migration. The effects of other ions and proteins in mitochondria and their interactions were not considered. As can be seen in Fig. 3.1(d), a diffusion flux can be induced by pH difference in mitochondria, whereas an electric field can be generated by the surface charge of the IMM.

This model has 2 domains (IMM and IMS) and 3 boundaries (OMM, P side, and N side). The matrix domain was not considered because we assumed that the electric potential and the proton concentration inside the matrix are uniform. Three variables

including electric potential (ϕ), proton concentration in the IMS (c_H), and the surface charge density at the P side (ρ_s) were considered in this model.

Classically, the Nernst-Planck equation has been used to describe the transport of ions under a concentration gradient and an electric potential gradient [21-23]. In this study, the modified Nernst-Planck (N-P) equation was used to simulate the steady state proton concentration in the IMS (c_H).

$$\nabla \cdot [D_H^i \nabla c_H + \mu z c_H \nabla \phi] = 0, \tag{3.4}$$

where D_H^i is the intracellular proton diffusion coefficient, μ is the electrical mobility of the proton, and z is the valence of the proton ($z=1$). The Stokes-Einstein relation, which is the relationship between a diffusion coefficient and electrical mobility, was not applied in this equation because the interaction between solute and solvent may not be negligible in our model system. Instead, we used experimentally measured diffusion coefficients and electrical mobility.

All coefficients and parameters used in this model are summarized in Table 3.3. Two boundary conditions at the P side and the OMM were required because the N-P equation was applied only in the IMS domain. At the P side, the net flux of protons was determined to be zero by assuming a balance between the number of protons pumped out by electron transport chain and those brought in through ATP synthase.

At the OMM boundary, the Dirichelet boundary condition was applied. Because the OMM is permeable to protons, the protons at the OMM boundary can be buffered by the bulk cytosolic solution.

Boundary conditions:

$$\begin{cases} \boldsymbol{n} \cdot (-D_H^i \nabla c_H - \mu z c_H \nabla \phi)\big|_{P\ side} = 0 \\ c_H\big|_{OMM} = [H^+]_{cyto} \end{cases},$$

(3.5)

where $[H^+]_{cyto}$ is bulk concentration of proton in cytosol.

We modeled the electric potential (ϕ) in the IMM and the IMS based on the following theoretical model. Mitochondrial membrane potential ($\Delta\Psi_m$) is induced by coupled electron transport and proton translocation. Protons are pumped out from the matrix by electron transport chain. Some of these protons bind to the P side instead of diffusing into the bulk solution of the IMS. These membrane-bound protons efficiently diffuse along the membrane surface (P side) from source (electron transport chain) to sink (ATP synthase), charging the P side positively. In the meantime, electrons flowed from the electron transport chain, and then charged the N side negatively [24-29]. Accordingly, the electric potential (ϕ) in the IMM and the IMS can be described by Poisson's equation.

$$\nabla^2 \phi = -\frac{\rho_f}{\varepsilon},$$

(3.6)

where ρ_f is the free charge density, and ε is the permittivity. The free charge density (ρ_f) in the IMM domain was assumed to be zero because the IMM was modeled as a capacitor. Zero free charge density was also applied in the IMS domain because we assumed that the electroneutrality condition holds in the IMS (i.e., the net electrical charge is zero because charges from protons may be canceled out by other ions). Boundary conditions are applied at the N side, the P side and the OMM. Based on the above theoretical model, the N side may be assumed to be an equipotential surface, while

the P side requires the surface charge density (ρ_s) profile to be used as a boundary condition. At the OMM, the zero charge boundary condition was used.

Boundary conditions:

$$\begin{cases} \phi\big|_{N\ side} = 0 \\ \boldsymbol{n} \cdot (\varepsilon_0 \varepsilon_{IMM} E_1 - \varepsilon_0 \varepsilon_{IMS} E_2)\big|_{P\ side} = \rho_s\ , \\ \boldsymbol{n} \cdot (\varepsilon \nabla \phi)\big|_{OMM} = 0 \end{cases} \tag{3.7}$$

where $\boldsymbol{n}$ is a normal vector, ε_0 is the electric constant, ε_{IMM} is the relative permittivity of the IMM, ε_{IMS} is the relative permittivity of the IMS, and E_1 and E_2 are electric fields of the IMM and IMS at the P side, respectively.

The surface charge density (ρ_s) used in the above boundary condition at the P side is not a constant. Because the surface charge density can be obtained from the density of membrane-bound protons (by multiplying the Faraday constant), ρ_s was also modeled using the modified Nernst-Planck equation.

$$\nabla \cdot [D_H^{mb} \nabla \rho_s + \mu \rho_s \nabla \phi] = 0\ , \tag{3.8}$$

where D_H^{mb} is the diffusion coefficient of membrane-bound protons. The electrical mobility of the membrane-bound proton is assumed to be the same as that of the proton in the IMS. To impose a constraint on ρ_s, we assumed that the average density of membrane-bound proton (or surface charge density) does not vary in each simulation.

$$\oiint_{P\ side} \rho_s dA = \rho_0 \oiint_{P\ side} dA\ , \tag{3.9}$$

where ρ_0 is the average surface charge density at the P side. Because this constraint can provide an equivalent condition of proton transport across the IMM (or the activities and contributions of proton source and sink) at each simulation, it enables to exclusively

investigate the effect of the IMM morphology without considering the effects of proton

source and sink.

Table 3.3. Simulation coefficients and parameters

Symbol	Description	Reference value	Value used	Reference
$c_{H,matrix}$	Bulk concentration of proton in matrix	pH 8.0	1×10^{-5} mol/m^3	[16]
$c_{H,cyto}$	Bulk concentration of proton in cytosol	pH 7.2	$1 \times 10^{-4.2}$ mol/m^3	[16]
D_H^i	Diffusion coefficient of intracellular proton	$4 \times 10^{-7} - 15.2 \times 10^{-7}$ cm^2/s	10×10^{-7} cm^2/s	[30]
D_H^{mb}	Diffusion coefficient of membrane-bound proton	$2 \times 10^{-7} - 5.8 \times 10^{-5}$ cm^2/s	1×10^{-5} cm^2/s	[29, 31-36]
μ	Electric mobility of proton in medium	$28.7 \times 10^{-4} - 35.9 \times 10^{-4}$ cm^2/(V s)	30×10^{-4} cm^2/(V s)	[37]
ε_{IMS}	Relative permittivity of the IMS	80	80	[38]
ε_{IMM}	Relative permittivity of the IMM	–	5.647	*
ρ_0	Average surface charge density at the P side	–	1.5×10^{-3} C/m^2	†
ρ_{ATPase}	Density of ATP synthase	–	2500 molecules/μm^2	‡
J_H	Proton flux	3100 H$^+$/s/ATPase	4.966×10^{-16} C/s/ATPase	[39]
E_{ATP}	Energy used to synthesize 1 mole of ATP	14 kcal/mol	58576 J/mol	[29]
D	Diameter of a crista junction	20−40 nm	30 nm	[4]
L	Length of a crista junction	30−50 nm	40 nm	[4]

* ε_{IMM} is calculated by assuming that the capacitance of the IMM is 1 μF/cm^2 and the IMM thickness (t_{IMM}) is 5 nm. $\varepsilon_{IMM} = (t_{IMM}/\varepsilon_0) \times (1$ μF/cm$^2) = 5.647$, where ε_0 is the electric constant.
† ρ_0 is calculated using the parallel plate capacitor model with a $\Delta\Psi_m$ of -150 mV.
$\rho_0 = \varepsilon_0 \varepsilon_{IMM} \times (\Delta\phi/ t_{IMM}) = 1.5 \times 10^{-3}$ C/m^2, where $\Delta\phi$ is 150 mV.
‡ ρ_{ATPase} is calculated from the average distance between ATP synthases [40]
$\rho_{ATPase} = 1/(20$ nm$\times 20$ nm$) = 2500$ molecules/μm^2.

The 2D axisymmetric finite element method was implemented to solve these coupled equations with coupled boundary conditions. We used the 'Transport of Diluted Species', 'Electrostatics', and 'Weak Form Boundary PDE' modules in COMSOL Multiphysics 4.3 (Comsol, Stockholm, Sweden).

3.2.3. Post-processing

The electric potential (ϕ) and proton concentration (c_H) distributions were simulated with various geometrical parameters of a crista. The mitochondrial membrane potential ($\Delta\Psi_m$) and the proton concentration difference across the IMM (ΔpH) were calculated from these two variables (ϕ and c_H), as

$$\Delta\Psi_m = \phi\big|_{N\ side} - \phi\big|_{P\ side} ,$$
(3.10)

$$\Delta pH = pH\big|_{N\ side} - pH\big|_{P\ side} = \log_{10}\frac{c_H\big|_{P\ side}}{[H^+]_{matrix}} .$$
(3.11)

From ΔpH, the chemical potential difference across the IMM ($\Delta\mu_H$) was calculated.

$$\Delta\mu_H = RT\ln\frac{c_H\big|_{N\ side}}{c_H\big|_{P\ side}} = -\ln(10)RT\Delta pH ,$$
(3.12)

where R is the gas constant and T is temperature (310 K).

The proton motive force (PMF) is composed of the electric potential difference ($\Delta\Psi_m$) and chemical potential difference ($\Delta\mu_H$).

$$PMF = \Delta\Psi_m + \Delta\mu_H / F ,$$
(3.13)

where F is the Faraday constant.

Given that the PMF is not uniform along the P side, the average PMF was defined in order to compare the effects of various parameters. The average PMF on the CM (PMF_{CM}) was calculated by integrating the PMF over the P side of the CM divided by the area of that region.

$$PMF_{CM} = \frac{\iint_{\text{P side CM}} PMF \; dA}{\iint_{\text{P side CM}} dA} .$$

(3.14)

The average PMF on the IBM (PMF_{IBM}) was also defined similarly.

However, the average PMF might be an insufficient parameter for representing the total capacity for ATP synthesis because it does not consider the total area. To quantify this total capacity, we calculated the rate of ATP synthesis (R_{ATP}) of a crista as follows:

$$R_{ATP} = \iint_{\text{P side CM}} (-PMF) J_H \rho_{ATPase} dA \Big/ E_{ATP} ,$$

(3.15)

where J_H is the proton flux, ρ_{ATPase} is the density of ATP synthase, and E_{ATP} is the energy used to synthesize 1 mole of ATP.

For calculating and plotting the results, MATLAB R2009a (The MathWorks, Natick, MA) was used with COMSOL Multiphysics.

3.3. RESULTS

3.3.1. The effect of the crista on electrochemical potential

By using the mitochondrion model, we first tested the hypothesis that the PMF is higher on the CM than on the IBM. Fig. 3.3 shows an example of a mitochondrion model and its simulation results. As can be seen in Fig. 3.3(a), the electric potential in the crista is lower than that in the non-crista portion of the IMS. This electric potential difference can induce proton concentration gradient, i.e., protons are more concentrated in the crista because of the lower electric potential there (more details will be explained in the discussion section). As a result, the proton concentration in the crista is significantly greater than that of the non-crista portion (Fig. 3.3(b)). This high proton concentration inside the crista results in a higher absolute value of the chemical potential difference ($\Delta\mu_H$) across the CM compared to that across the IBM, and a consequently higher absolute value of the PMF on the CM. In the model shown in Fig. 3.3, the average PMF on the CM (PMF_{CM}) is -231.1 mV, while that on the IBM is -200.5 mV.
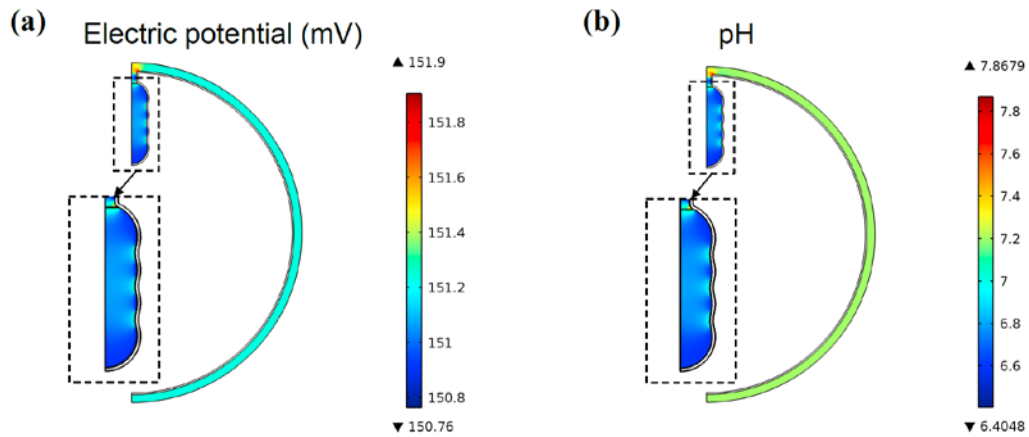
Figure 3.3. An example of the mitochondrion model with a single crista (type II, N_{circle}=4, r_0=50 nm, θ_0=15°). (a) Electric potential distribution in the IMS (mV). (b) Proton concentration distribution in the IMS (expressed as pH).

3.3.2. The effect of the overall shape of a crista

To investigate the effect of the overall shape of a crista structure on electrochemical potential, the type I crista geometries were constructed as described in the methods section.
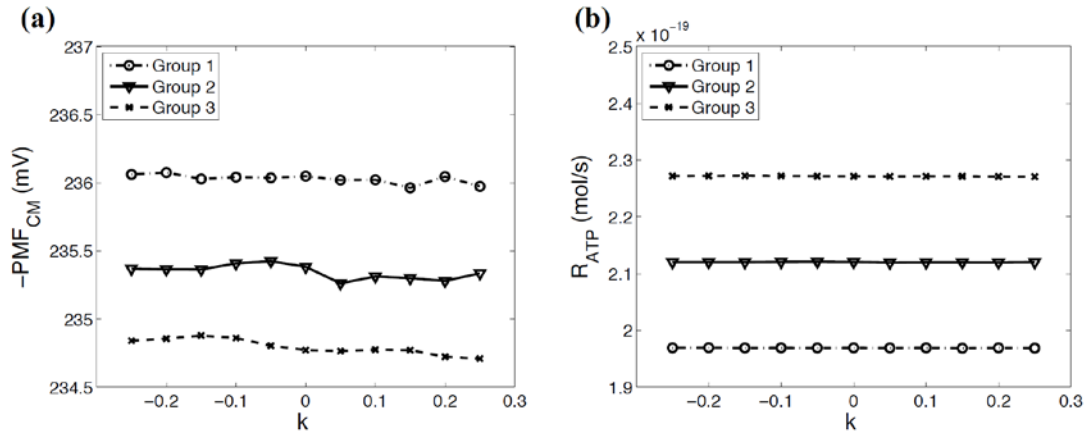
Figure 3.4. The effect of the overall crista shape (parameterized by k) on the average PMF on the CM (PMF_{CM}) and the rate of ATP synthesis (R_{ATP}). (A) The effect of k on the PMF_{CM} for groups 1−3. (B) The effect of k on the R_{ATP} for groups 1−3.

As can be seen in Fig. 3.4, k does not show significant effects on either the PMF_{CM} or the R_{ATP} (ANOVA p-value≈1). Thus, the overall shape of a crista may not be an important factor for the electrochemical potential of mitochondria. Instead, even though the difference of the PMF_{CM} among groups 1, 2 and 3 is substantively small (~1.2 mV difference between groups 1 and 3), this difference is still statistically significant (p-value<0.05). Similarly, the difference of the R_{ATP} among groups is statistically significant.

As summarized in Table 3.1, groups 1, 2 and 3 have different surface areas and surface-to-volume ratios. Group 1, which has the highest surface-to-volume ratio and the smallest surface area, has the highest absolute value of the PMF_{CM} and the lowest R_{ATP}. Conversely, group 3, which has the smallest surface-to-volume ratio and the largest surface area, has the lowest absolute value of the PMF_{CM} and the highest R_{ATP}. Therefore, the PMF_{CM} may depend on the surface-to-volume ratio, whereas the R_{ATP} may depend on the surface area. This hypothesis was further investigated by using the type II crista geometries.

3.3.3. The effect of the surface area and the surface-to-volume ratio of a crista
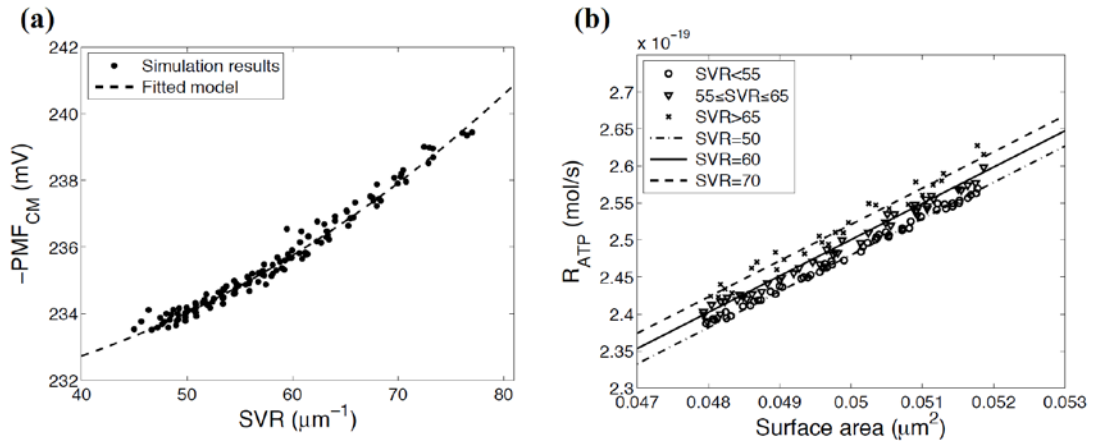
Figure 3.5. The effect of the detailed crista morphology on the average PMF on the CM (PMF_{CM}) and the rate of ATP synthesis (R_{ATP}). (A) The effect of the surface-to-volume ratio (SVR) on the PMF_{CM}. (B) The respective effects of the surface area and the SVR on the R_{ATP}. Markers show the simulation results. Dashed lines are fitted models of simulation results.

By using the type II crista geometry, we examined the hypothesis that the surface area and the surface-to-volume ratio of a crista correlate with both the PMF_{CM} and the R_{ATP}. Fig. 3.5 shows the effects of the surface-to-volume ratio and the surface area on the PMF_{CM} and the R_{ATP}.

The lines in Fig. 3.5 are fitted models of the simulation results based on following equations:

$$-PMF_{CM} = \alpha_0 + \alpha_1 x_1^{\alpha_2}, \tag{3.16}$$

$$R_{ATP} = \beta_0 + \beta_1 x_1 + \beta_2 x_2, \tag{3.17}$$

where x_1 is the surface-to-volume ratio and x_2 is the surface area. Both models fit well with the simulation results (R^2 for the $-PMF_{CM}$ and the R_{ATP} are 0.9818 and 0.9982, respectively). The absolute value of the PMF_{CM} mainly depends on the surface-to-volume ratio (fits well to a power-law model), whereas the R_{ATP} almost linearly depends on the surface area. The effect of the surface area on the PMF_{CM} is not statistically significant (p-value=0.063), while the effect of the surface-to-volume ratio on the R_{ATP} is statistically significant (p-value<0.05).

3.3.4. The effect of the crista junction morphology

The size effects of the crista junction on electrochemical potential were also investigated. Unlike the crista morphology, the crista junction morphology may not be significantly regulated by the energy state of mitochondria. Instead, the crista junction may be formed spontaneously to have a thermodynamically favored conformation. This

hypothesis is consistent with the empirical observations that found similar morphologies of crista junctions from condensed and orthodox mitochondria [2, 41]. To test the hypothesis that the morphology of the crista junction is correlated with energetic functions of mitochondria, we varied crista junction length (L) and diameter (D), and subsequently calculated the PMF_{CM} and the R_{ATP}.
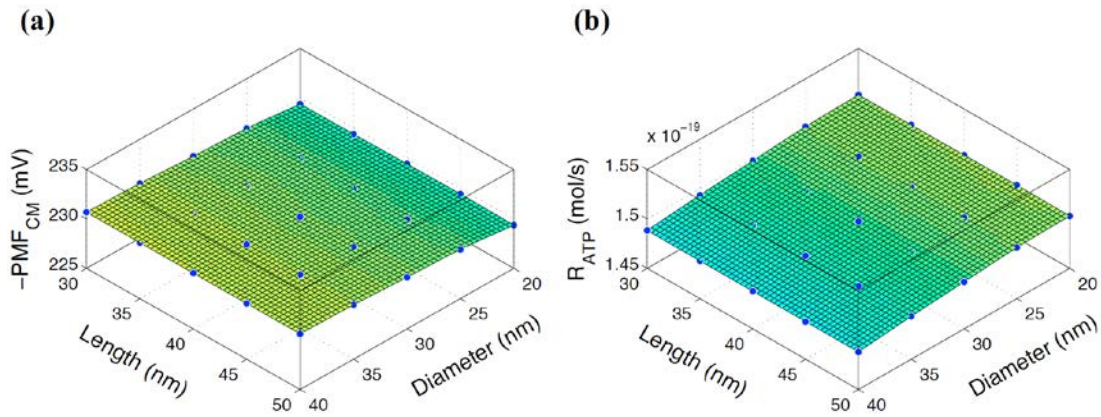
Figure 3.6. The effect of the crista junction diameter (D) and length (L) on the average PMF on the CM (PMF_{CM}) and the rate of ATP synthesis (R_{ATP}) (D_H^{mb} =1×10⁻⁵ cm²/s, a single sphere crista with radius=50 nm). (A) Change in the average PMF on the CM. (B) Change in the ATP synthesis rate (R_{ATP}). Blue dots indicate data points where simulations were conducted.

As can be seen in Fig. 3.6, the length of the crista junction (L) does not notably affect either the PMF_{CM} or the R_{ATP}. The effect of the crista junction diameter (D) is also small. When the diameter ranges from 20 nm to 40 nm, the PMF_{CM} and the R_{ATP} vary only 0.6% and 1%, respectively. Thus, these simulation results are in accordance with the existing literature.

Based on the simulation results, we propose that different thermodynamically favored morphological configurations between individual cristae and the crista junction may be achieved by specific protein complexes such as those related to the dynamin-related protein and/or membrane composition. Given the relatively uniform morphology of the crista junction and the conservation of distinctive crista morphologies at different energy states, these two sub-compartments of the IMM may contain significantly different compositions, giving rise to diverse localized mechanical properties. For example, if the elastic moduli (or stiffness) of the crista and the crista junction are significantly different, two distinguishable sub-compartments may be formed. On the one hand, the crista can easily change its morphology in response to the matrix volume regulation. On the other hand, the crista junction may maintain its tubular shape if it has a relatively high elastic modulus. However, the precise compositions and mechanical properties of the crista and the crista junction are not fully understood.

3.4. DISCUSSION

3.4.1. Biophysical significance of the crista structure

The higher absolute value of the PMF on the CM predicted by this model may provide an explanation of experimentally observed non-uniform distribution of the proton source (electron transport chain) and sink (ATP synthase) along the IMM. It has been found that the electron transport chain and ATP synthase are more concentrated in the CM [42, 43]. From our simulation results, this inhomogeneous distribution may benefit

the energy conversion process of mitochondria: by having more ATP synthase in the CM, mitochondria can synthesize ATP more efficiently due to the high absolute value of the PMF, which is the driving force for ATP synthesis.

Additionally, the simulation model showed that a high PMF can be induced by the large surface-to-volume ratio of a crista, while a high capacity for ATP synthesis may require the large surface area of a crista. These simulation results may present inferences for the relationship between the IMM morphology and the energy state of mitochondria. As mentioned earlier in the introduction section, two distinctive cristae structures were observed from mitochondria of two different respiratory activities: small cristae at low respiratory activity (state 4) and large cristae at high respiratory activity (state 3) [5-7]. At low respiratory activity, a small crista may be favorable because a small surface area is sufficient for the low ATP synthesis rate. Moreover, a small crista may have a higher PMF than a large crista of similar shape because a small crista can have a greater surface-to-volume ratio. On the other hand, a large crista with a large surface area, which has greater capacity for ATP synthesis, may be required to meet high energy demand at high respiratory activity. This hypothesis is in agreement with experimental studies that estimated 30−60 mV higher PMF in state 4 (~230 mV) compared to that in state 3 (170−200 mV) [44, 45].

3.4.2. Membrane-bound proton diffusion coefficient

In our model, the membrane-bound proton diffusion coefficient (D_H^{mb}) was assumed to be 1×10^{-5} cm^2/s. However, the measurements of the lateral proton diffusion

coefficient along the membrane surface have exhibited two orders of magnitude in difference (2×10^{-7}−5.8×10^{-5} cm^2/s) [29, 31-36]. Because the D_H^{mb} can influence the profiles of membrane-bound proton concentration, surface charge density at the P side, and electric potential, we will discuss the effects of the D_H^{mb} on the electrochemical potential of mitochondria.
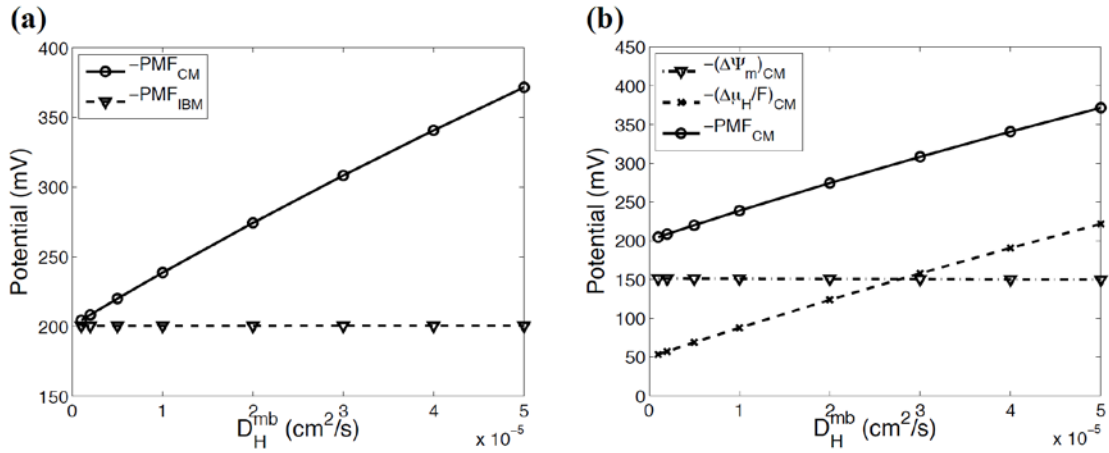
Figure 3.7. The effect of the membrane-bound proton diffusion coefficient (D_H^{mb}) on electrochemical potential (using a single sphere crista with radius=50 nm). (A) Change in the average PMF on the CM and the IBM. (B) Change in the average $\Delta\Psi_m$, the average $\Delta\mu_H/F$, and the average PMF on the CM.

As can be seen in Fig. 3.7(a), the absolute value of the average PMF on the CM increases linearly as the diffusion coefficient increases, while the average PMF on the IBM is almost independent of the diffusion coefficient. This increase in the $-PMF_{CM}$ is caused by the increase in the chemical potential difference (Fig. 3.7(b)), not by the membrane potential. In our model, two transport mechanisms of membrane-bound proton were considered: 'diffusion' and 'electric field-induced migration'. If the D_H^{mb} is small

compared to the electric mobility (μ), then 'electric field-induced migration' will be the dominant mechanism of the membrane-bound proton transport. This will induce membrane-bound protons to move along the P side in order to minimize the electric potential gradient along the P side. Because of this approximately constant electric potential, the proton concentration in the IMS (c_H) near the P side will become nearly uniform, resulting in a relatively small chemical potential gradient. In contrast, if the D_H^{mb} is sufficiently large compared to the electric mobility (μ), 'diffusion' will be the dominant mechanism of the membrane-bound proton transport. In this case, the membrane-bound proton concentration along the P side (which determines the surface charge density) will be closer to uniform. Due to the irregular geometry of the CM, this roughly uniform surface charge density profile will induce an electric potential gradient (lower electric potential on the P side of the CM than that on the P side of the IBM). At this point the protons in the IMS will be transported to the opposite direction of the electric potential gradient, resulting in a high proton concentration in the crista and consequently a high chemical potential gradient across the CM.

As mentioned earlier, it has been proposed that high proton concentration inside a crista is induced by restricted diffusion. However, simulation results presented here suggest that the high proton concentration inside a crista can also be induced by the non-uniform electric potential along the P side resulting from the morphology-dependent membrane-bound proton distribution. To validate this model, the measurements of the local electric potential and the proton concentration around the IMM warrant further investigation.

3.4.3. Model assumptions and limitations

We applied continuum theories to model the electrochemical potential of mitochondria, even though few protons can exist at the given pH values and sizes of the system. This treatment of pH values as a continuum is based on the chemiosmotic theory (i.e., the chemiosmotic theory assumes pH values in the chemical potential term of the proton motive force as a continuum). However, to the best of our knowledge, this issue has not been clearly justified in the existing literature. Our justification of this issue is as follows: Even though the number of protons at each moment is very small, it has been experimentally shown that the proton flux through ATP synthase and electron transport chain is very high (>1000 H^+/s/molecule) [29, 39, 46]. To meet this high flux condition, protons should circulate very rapidly. Thus, the average distribution of protons over time can still be treated as a continuum. Moreover, a continuum-based approach is reasonable because we are not interested in the specific position of each proton at each instance of time, but the average distributions related to different geometries.

The next subject to be discussed is the modeling mitochondrial structures. Mitochondrial structures were constructed from combinations of basic shapes including sphere and cylinder. The application of basic shapes in the crista structure may limit the available range of the surface-to-volume ratio of a crista. As the PMF_{CM} is a function of the surface-to-volume ratio, the range of the PMF_{CM} simulated in this study ($\sim 234-240$ mV) is limited and may not be enough to show a biologically meaningful difference. Furthermore, given the heterogeneous compositions of the IMM, the thickness of the IMM is not uniform, which can cause changes in the local electrical capacity and the electric potential. However, it is difficult to implement a complex 3D mitochondrion

structure that requires extremely fine elements and currently expensive computations. Capturing complex geometries and localized properties of the IMM would require a stochastic model, with a large number of realizations for a variety of conditions. Variations among realizations of the same complex set of geometric descriptors would be likely to obfuscate lager trends, such as the effects of the suface area and the surface-to-volume ratio of an individual crista. This complex model geometry can also introduce computational inaccuracies and instabilities. In this sense, simplified model geometries may be more suitable for identifying the effects of key morphological parameters.

Another set of assumptions in this model is proton concentration distributions outside the mitochondrion, inside the matrix, and in the IMS. Proton concentration outside the OMM was not modeled due to our assumption of constant cytosolic pH; however, cytosolic pH can also be affected by mitochondrial matrix alkalinization [47]. In addition, uniform pH in the matrix can be challenged by complex compositions of the matrix. A prerequisite for the assumption of uniform pH in the matrix is uniform electric potential in the matrix. However, little is known of electric potential and proton concentration distributions in the matrix. The matrix contains a high density of enzymes and other proteins [48]. This high density of macromolecules may require specific configurations that may induce non-uniform electric potential. In the IMS, we modeled proton concentration profile by assuming that the interaction between protons and other ions are negligible and that the net electric charge of ions in the IMS is neutral. These assumptions, however, have not been sufficiently investigated.

Furthermore, we assumed that the narrow crista junction morphology does not alter the diffusion coefficient. However, the narrow opening of the crista junction has

been hypothesized to restrict the diffusion of molecules between the crista and the non-crista portion of the IMS [1-4, 41]. In addition, a recent simulation study suggested that the anomalous diffusion of proteins can be induced by cristae geometries [20]. Even though this geometrical effect on the diffusion coefficient might not be applicable to protons (given the relatively small size and low concentration of protons with respect to the typical size of the crista junction), the crista junction morphology may affect mitochondrial functions by regulating the transport of metabolic substrates and proteins, which have greater molecular weights and volumes [1, 4].

Finally, inhomogeneous composition of the IMM was not considered. In particular, proteins, including ATP synthase and electron transport chain, are not evenly distributed in the IMM [42, 43]. These non-uniform distributions of proton source and sink may influence the membrane potential. Moreover, the activities of these protein complexes, regulated by the energy state of mitochondria, can also change the membrane potential. In our model, however, the average surface charge density was assumed to be constant in each simulation in order to exclusively investigate the morphological effects.

3.5. CONCLUSIONS

To date, research on the role of highly varied IMM structure has been primarily based on empirical observations that are not supported by theoretical verifications. Recently, some simulation studies have been conducted to explain the observed IMM structures using thermodynamic models [18, 19] and to examine the validity of a crista junction morphology as a diffusion barrier [20]. However, a model simulating the effect

of the IMM structure on ATP synthesis has not yet been developed. This study aimed to explain the biophysical significance of IMM structures on the energetic function of mitochondria using finite element methods. We constructed a simplified mitochondrion model that enables easy parameterization of the IMM structure. From this model, we found that a crista can enhance ATP synthesis not only by increasing the surface area, but also by increasing the PMF. Based on results from the current simulation, high PMF on the CM (mainly contributed by high proton concentration in the crista) is induced by its concave geometry, but is not necessarily related to the restricted diffusion that may be caused by a narrow crista junction opening. It was shown in the model that the morphology-dependent electric potential induces a proton concentration difference between a crista and the non-crista portion of the IMS (i.e., a crista can act as a proton trap not by restricted diffusion, but by induced electric field).

Our simulation results also present potential explanations on the relationship between cristae morphologies and energy states. The simulation model showed that a high PMF can be induced by the large surface-to-volume ratio of a crista, whereas a high capacity for ATP synthesis can be mainly achieved by increasing the surface area of a crista. Based on these simulation results, the orthodox conformation (small cristae) might be more favorable for mitochondria of low respiratory activity, whereas the condensed conformation (large cristae) can be more preferable for mitochondria of high respiratory activity.

Even though our model successfully details the biophysical significance of IMM structures, the current model might not sufficiently describe some important biological aspects because of potential over-simplifications and assumptions specific to these

calculations. Further investigation is required into the local electric potential and the distribution of protons, as well as the proton transport mechanisms in mitochondria in order to improve the validity of computational estimates of causal relationships between morphology and biochemical function.

3.6. BIBLIOGRAPHY

1. C. A. Mannella, D. R. Pfeiffer, P. C. Bradshaw, I. I. Moraru, B. Slepchenko, L. M. Loew, C. E. Hsieh, K. Buttle, and M. Marko, Topology of the mitochondrial inner membrane: dynamics and bioenergetic implications. *IUBMB Life* 52, 93 (2001).

2. G. A. Perkins, C. W. Renken, T. G. Frey, and M. H. Ellisman, Membrane architecture of mitochondria in neurons of the central nervous system. *Journal of Neuroscience Research* 66, 857 (2001).

3. T. G. Frey, C. W. Renken, and G. A. Perkins, Insight into mitochondrial structure and function from electron tomography. *Biochimica et Biophysica Acta (BBA) - Bioenergetics* 1555, 196 (2002).

4. C. A. Mannella, The relevance of mitochondrial membrane topology to mitochondrial function. *Biochimica et Biophysica Acta (BBA) - Molecular Basis of Disease* 1762, 140 (2006).

5. C. A. Mannella, Structure and dynamics of the mitochondrial inner membrane cristae. *Biochimica et Biophysica Acta (BBA) - Molecular Cell Research* 1763, 542 (2006).

6. C. A. Mannella, Structural diversity of mitochondria. *Annals of the New York Academy of Sciences* 1147, 171 (2008).

7. G. A. Perkins, and M. H. Ellisman, Mitochondrial configurations in peripheral nerve suggest differential ATP production. *Journal of Structural Biology* 173, 117 (2011).

8. S. K. Sharma, Neuroprotective actions of Selegiline in inhibiting 1-methyl, 4-phenyl, pyridinium ion (MPP)-induced apoptosis in SK-N-SH neurons. *Journal of neurocytology* 32, 329 (2003).

9. Z. X. Yu, Mutant huntingtin causes context-dependent neurodegeneration in mice with Huntington's disease. *The Journal of neuroscience* 23, 2193 (2003).

10. L. M. Loew, R. A. Tuft, W. Carrington, and F. S. Fay, Imaging in five dimensions: time-dependent membrane potentials in individual mitochondria. *Biophysical Journal* 65, 2396 (1993).

11. C. Fink, F. Morgan, and L. M. Loew, Intracellular fluorescent probe concentrations by confocal microscopy. *Biophysical Journal* 75, 1648 (1998).

12. J. J. Lemasters, D. R. Trollinger, T. Qian, W. E. Cascio, and H. Ohata, Confocal imaging of Ca^{2+}, pH, electrical potential, and membrane permeability in single living cells. *Methods in Enzymology* 302, 341 (1999).

13. W. J. H. Koopman, F. Distelmaier, J. J. Esseling, J. A. M. Smeitink, and P. H. G. M. Willems, Computer-assisted live cell analysis of mitochondrial membrane potential, morphology and calcium handling. *Methods* 46, 304 (2008).

14. J. Llopis, J. M. McCaffery, A. Miyawaki, M. G. Farquhar, and R. Y. Tsien, Measurement of cytosolic, mitochondrial, and golgi pH in single living cells with green fluorescent proteins. *Proceedings of the National Academy of Sciences of the United States of America* 95, 6803 (1998).

15. A. M. Porcelli, A. Ghelli, C. Zanna, P. Pinton, R. Rizzuto, and M. Rugolo, pH difference across the outer mitochondrial membrane measured with a green

fluorescent protein mutant. *Biochemical and Biophysical Research Communications* 326, 799 (2005).

16. A. P. Bolshakov, M. M. Mikhailova, G. Szabadkai, V. G. Pinelis, N. Brustovetsky, R. Rizzuto, and B. I. Khodorov, Measurements of mitochondrial pH in cultured cortical neurons clarify contribution of mitochondrial pore to the mechanism of glutamate-induced delayed Ca^{2+} deregulation. *Cell Calcium* 43, 602 (2008).

17. D. Poburko, J. Santo-Domingo, and N. Demaurex, Dynamic regulation of the mitochondrial proton gradient during cytosolic calcium elevations. *The Journal of biological chemistry* 286, 11672 (2011).

18. A. Ponnuswamy, J. Nulton, J. M. Mahaffy, P. Salamon, T. G. Frey, and A. R. C. Baljon, Modeling tubular shapes in the inner mitochondrial membrane. *Physical Biology* 2, 73 (2005).

19. M. Ghochani, J. D. Nulton, P. Salamon, T. G. Frey, A. Rabinovitch, and A. R. C. Baljon, Tensile forces and shape entropy explain observed crista structure in mitochondria. *Biophysical Journal* 99, 3244 (2010).

20. V. M. Sukhorukov, and J. Bereiter-Hahn, Anomalous diffusion induced by cristae geometry in the inner mitochondrial membrane. *PLoS ONE* 4, e4604 (2009).

21. T. Sokalski, P. Lingenfelter, and A. Lewenstam, Numerical solution of the coupled Nernst−Planck and Poisson equations for liquid junction and ion selective membrane potentials. *The Journal of Physical Chemistry B* 107, 2443 (2003/03/01, 2003).

22. J. Lim, J. D. Whitcomb, J. G. Boyd, and J. Varghese, Effect of electrode pore geometry modeled using Nernst–Planck–Poisson-modified Stern layer model. *Computational mechanics* 43, 461 (2009).

23. B. Lu, M. J. Holst, J. Andrew McCammon, and Y. C. Zhou, Poisson–Nernst–Planck equations for simulating biomolecular diffusion–reaction processes I: finite element solutions. *Journal of Computational Physics* 229, 6979 (2010).

24. P. Mitchell, Chemiosmotic coupling in oxidative and photosynthetic phosphorylation. *Biological Reviews* 41, 445 (1966).

25. M. Prats, J.-F. Tocanne, and J. Teissie, Lateral proton conduction at a lipid/water interface. Its modulation by physical parameters. Experimental and mathematical approaches. *European journal of biochemistry* 149, 663 (1985).

26. J. Heberle, J. Riesle, G. Thiedemann, D. Oesterhelt, and N. A. Dencher, Proton migration along the membrane surface and retarded surface to bulk transfer. *Nature (London)* 370, 379 (1994).

27. Y. N. Antonenko, and P. Pohl, Coupling of proton source and sink via H^+-migration along the membrane surface as revealed by double patch-clamp experiments. *FEBS Letters* 429, 197 (1998).

28. L. S. Yaguzhinsky, V. I. Yurkov, and I. P. Krasinskaya, On the localized coupling of respiration and phosphorylation in mitochondria. *Biochimica et Biophysica Acta (BBA) - Bioenergetics* 1757, 408 (2006).

29. N. Kocherginsky, Acidic lipids, H^+-ATPases, and mechanism of oxidative phosphorylation. Physico-chemical ideas 30 years after P. Mitchell's Nobel Prize award. *Progress in Biophysics and Molecular Biology* 99, 20 (2009).

30. P. Swietach, M. Zaniboni, A. K. Stewart, A. Rossini, K. W. Spitzer, and R. D. Vaughan-Jones, Modelling intracellular H^+ ion diffusion. *Progress in Biophysics and Molecular Biology* 83, 69 (2003).

31. U. Alexiev, R. Mollaaghababa, P. Scherrer, H. G. Khorana, and M. P. Heyn, Rapid long-range proton diffusion along the surface of the purple membrane and delayed proton transfer into the bulk. *Proceedings of the National Academy of Sciences of the United States of America* 92, 372 (1995).

32. C. J. Slevin, and P. R. Unwin, Lateral proton diffusion rates along stearic acid monolayers. *Journal of the American Chemical Society* 122, 2597 (2000/03/01, 2000).

33. J. Zhang, and P. R. Unwin, Proton diffusion at phospholipid assemblies. *Journal of the American Chemical Society* 124, 2379 (2002/03/01, 2002).

34. S. Serowy, S. M. Saparov, Y. N. Antonenko, W. Kozlovsky, V. Hagen, and P. Pohl, Structural proton diffusion along lipid bilayers. *Biophysical Journal* 84, 1031 (2003).

35. M. Brändén, T. Sandén, P. Brzezinski, and J. Widengren, Localized proton microcircuits at the biological membrane-water interface. *Proceedings of the National Academy of Sciences of the United States of America* 103, 19766 (2006).

36. Y. Antonenko, and P. Pohl, Microinjection in combination with microfluorimetry to study proton diffusion along phospholipid membranes. *European Biophysics Journal* 37, 865 (2008).

37. A. B. Duso, and D. D. Y. Chen, Proton and hydroxide ion mobility in capillary electrophoresis. *Analytical Chemistry* 74, 2938 (2002/07/01, 2002).

38. A. Ron, N. Fishelson, N. Croitoru, I. Shur, D. Benayahu, and Y. Shacham-Diamand, Examination of the induced potential gradients across inner and outer cellular interfaces in a realistic 3D cytoplasmic-embedded mitochondrion model. *Journal of electroanalytical chemistry* 638, 59 (2010).

39. M. J. Franklin, W. S. A. Brusilow, and D. J. Woodbury, Determination of proton flux and conductance at pH 6.8 through single F_o sectors from Escherichia coli. *Biophysical Journal* 87, 3594 (2004).

40. D. Acehan, A. Malhotra, Y. Xu, M. Ren, D. L. Stokes, and M. Schlame, Cardiolipin affects the supramolecular organization of ATP synthase in mitochondria. *Biophysical Journal* 100, 2184 (2011).

41. G. Perkins, C. Renken, M. E. Martone, S. J. Young, M. Ellisman, and T. Frey, Electron tomography of neuronal mitochondria: three-dimensional structure and organization of cristae and membrane contacts. *Journal of Structural Biology* 119, 260 (1997).

42. R. W. Gilkerson, J. M. L. Selker, and R. A. Capaldi, The cristal membrane of mitochondria is the principal site of oxidative phosphorylation. *FEBS Letters* 546, 355 (2003).

43. F. Vogel, C. Bornhövd, W. Neupert, and A. S. Reichert, Dynamic subcompartmentalization of the mitochondrial inner membrane. *The Journal of Cell Biology* 175, 237 (2006).

44. P. Mitchell, and J. Moyle, Estimation of Membrane Potential and pH Difference across the Cristae Membrane of Rat Liver Mitochondria. *European journal of biochemistry* 7, 471 (1969).

45.   D. G. Nicholls, The Influence of Respiration and ATP Hydrolysis on the Proton-Electrochemical Gradient across the Inner Membrane of Rat-Liver Mitochondria as Determined by Ion Distribution. *European journal of biochemistry* 50, 305 (1974).

46.   A. Wiedenmann, P. Dimroth, and C. von Ballmoos, $\Delta\psi$ and ΔpH are equivalent driving forces for proton transport through isolated F0 complexes of ATP synthases. *Biochimica et Biophysica Acta (BBA) - Bioenergetics* 1777, 1301 (2008).

47.   S. Matsuyama, J. Llopis, Q. L. Deveraux, R. Y. Tsien, and J. C. Reed, Changes in intramitochondrial and cytosolic pH: early events that modulate caspase activation during apoptosis. *Nat Cell Biol* 2, 318 (2000).

48.   B. A. Scalettar, J. R. Abney, and C. R. Hackenbrock, Dynamics, structure, and function are coupled in the mitochondrial matrix. *Proceedings of the National Academy of Sciences of the United States of America* 88, 8057 (1991).

CHAPTER 4

NUMERICAL STUDY OF INNER MITOCHONDRIAL MEMBRANE DYNAMICS: EFFECTS OF LOCAL pH ON CRISTAE MORPHOLOGIES[1]

4.1. INTRODUCTION

Mitochondria have been recognized as the primary cellular powerhouses, because their main function is synthesizing ATP by oxidative phophorylation. During oxidative phosphorylation, the electron transport chain pumps protons across the inner mitochondrial membrane (IMM) by using free energy released from a series of redox reactions. The resulting electrochemical gradient of proton is used for synthesizing ATP via ATP synthase [1, 2]. These protein complexes involved in ATP synthesis are located in the IMM. In particular, a subcompartment of the IMM called a crista has been considered to be the major site of ATP synthesis since proteins comprising ATP synthase and electron transport chain are more concentrated on cristae membranes [3, 4]. These cristae membranes have complex, diverse, and dynamic morphologies. The biophysical effects of these widely varied cristae morphologies have been studied in relation to mitochondrial functions. For example, the morphologies of cristae have been speculated

---

as the capacity enhancer for ATP synthesis by providing greater surface area and electrochemical potential [5-7]. Moreover, experimental studies found that mitochondria can have distinctive IMM morphologies with respect to their respiratory activities [8, 9]. However, the mechanisms of how these cristae structures can be formed and regulated and how the morphologies can be associated with mitochondrial functions have not been fully understood.

To explain the formation and regulation of cristae structures, two hypotheses have been proposed: i) cristae morphologies may be related to the distributions of protein complexes [7, 10, 11], and ii) cristae morphologies may be regulated by the local pH gradient generated from oxidative phosphorylation [12-14]. The first hypothesis is supported by the experimental observation (by using electron microscopy with 3D image reconstruction) showing long ribbons of ATP synthase dimers located at the apex of cristae membranes [11]. Even though these dimer ribbons may contribute to the formation of cristae structures by bending the membrane, this hypothesis does not provide a sufficient explanation on how the cristae morphologies can be regulated by the respiratory activities. The second hypothesis is based on the fact that area per lipid headgroup decreases as pH decreases. The local pH difference across the membrane can induce the curvature by the area mismatch between two layers of the membrane. In this case, the morphology of a crista membrane can change in response to the local pH gradient generated during oxidative phosphorylation. Therefore, the curvature and the morphology of a membrane can be associated with the respiratory activity.

The above hypothesis of the cristae formation by the local pH gradient was proposed by Khalifat et al. [12]. They experimentally showed that the local pH gradient

can form a cristae-like invagination on the giant unilamellar vesicle (GUV). The local pH gradient on the GUV was generated by the microinjection of acid. The cardiolipin (CL) containing GUVs presented dynamic and reversible changes of the cristae-like invaginations by acid delivery. They also provided theoretical explanations of observed cristae-like invaginations. Theoretical values of the radius and lengths of cristae-like tubules were calculated and compared with their experimental results. However, this study could not successfully explain why the cristae-like structures have tubular shapes and whether this shape is energetically favorable. Moreover, the mechanism proposed in this study needs to be validated at the mitochondrial scale because of the large size difference between mitochondria and GUVs (i.e. to form a crista at the mitochondrial scale, much higher local pH gradient may be required because a small crista has a higher curvature than a large crista of similar shape).

However, the experimental validation of this mechanism at the actual mitochondrial scale is restricted by optical resolution and control of the local pH profile. Therefore, simulation models are not only plausible supplements for resolving those experimental limitations, but also excellent techniques for presenting a theoretical understanding of existing observations. For example, a thermodynamic model was used to provide theoretical explanations of experimentally observed cristae morphologies [15-17]. The dynamics of lipid bilayer membranes were modeled and validated with the well-known biological membrane dynamics [18-24]. To date, however, a numerical model simulating the IMM dynamics associated with the local pH gradient has not been developed.

In this paper, we introduce a model simulating the morphologies of the IMM at the given pH profiles. First, a spontaneous curvature depending on the pH difference across the membrane is modeled. In addition to the estimation of the spontaneous curvature, the finite element model of lipid bilayer membranes developed by Feng, Ma, and Klug [19, 21] is applied to find the energetically favorable membrane configuration. By using this model, we investigate i) how a tubular cristae structure can be formed and dissipated by the local pH gradient, ii) which factors can affect the cristae membrane morphologies, and iii) whether the same mechanism proposed by Khalifat et al. can be applicable at the mitochondrial scale. Finally, the validity and limitations of this study are discussed.

4.2. METHODS

We applied the finite element model of lipid bilayer membranes developed by Feng, Ma and Klug [19, 21]. Our model system was composed of a single closed lipid bilayer with homogeneous composition (the effects of protein compositions were not considered). To reduce the computational cost, we limited our study to 2D axisymmetric geometries. We first calculated the spontaneous curvature of the membrane induced by the pH difference across the membrane in order to simulate the effect of the local pH. Finally, this spontaneous curvature was plugged into the lipid bilayer model to find the membrane configuration having the minimum energy.

4.2.1. Local pH and curvature of the lipid bilayer

During the oxidative phosphorylation, protons are pumped out from the matrix by the electron transport chain and generating the pH difference across the IMM. This pH difference can induce a curvature by mismatched areas between two layers of the membrane.
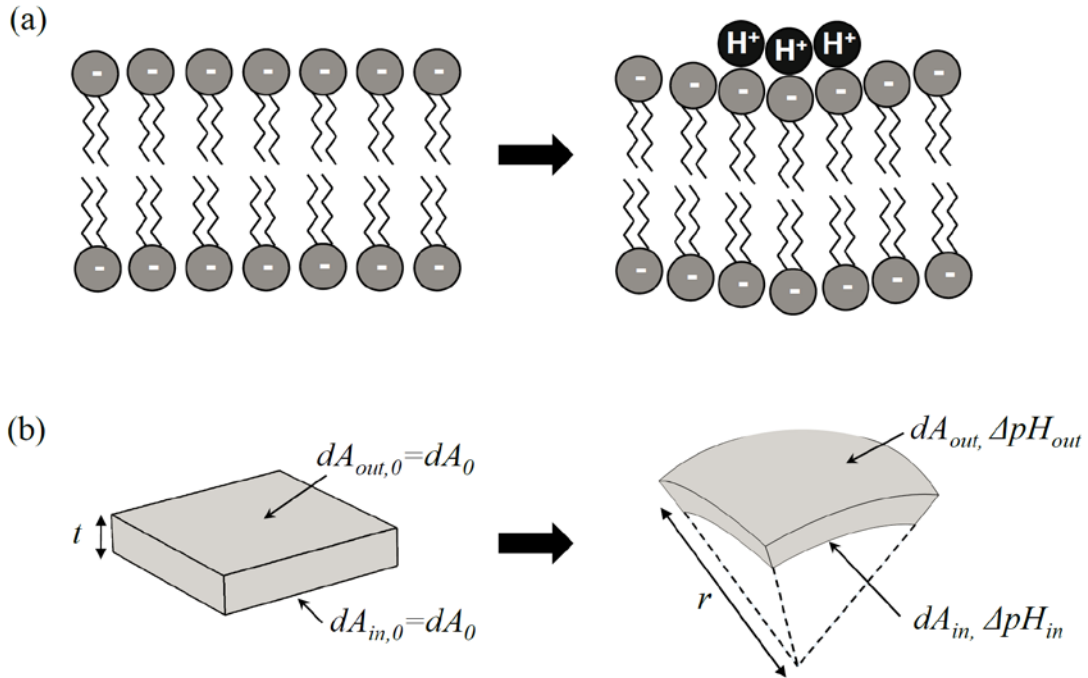

Figure 4.1. Curvature of the lipid bilayer induced by local pH. (a) Illustration of a curvature induced by locally introduced protons. (b) Modeling of the pH-dependent area change and resulting spontaneous curvature.

As illustrated in Fig. 4.1(a), positively charged protons (or hydrated hydrogen ions) introduced on the outer side of the membrane neutralize the negative charges of

lipid headgroups. This electrical neutralization reduces repulsive forces between headgroups and consequently the area per headgroup. This decreased area of the outer layer results in area mismatch between the inner and the outer layer. Finally, the curvature of the lipid bilayer can be induced by this area mismatch.

First, we modeled the pH-dependent area change similar to thermal expansion.

$$A = A_0(1 + \alpha_A \Delta pH),$$ (4.1)

where A and A_0 are areas of the layer before and after pH change, respectively; α_A is the area expansion coefficient; and ΔpH is the pH difference ($\Delta pH = pH - pH_0$). From Eq. (4.1), the infinitesimal areas of the inner and the outer layer after pH change dA_{in} and dA_{out} (see Fig. 4.1(b)) are

$$dA_{in} = dA_0(1 + \alpha_A \Delta pH_{in}),$$ (4.2)

$$dA_{out} = dA_0(1 + \alpha_A \Delta pH_{out}).$$ (4.3)

On the other hand, dA_{in} and dA_{out} can also be calculated by assuming that the inner and outer layers form concentric spherical surfaces.

$$dA_{in} = (r - t/2)^2 \sin\theta d\theta d\phi,$$ (4.4)

$$dA_{out} = (r + t/2)^2 \sin\theta d\theta d\phi,$$ (4.5)

where r is the radius of the midplane of the membrane, t is the thickness of the membrane (5 nm), θ is a polar angle, and ϕ is an azimuth angle of a spherical coordinate system. From Eqs. (4.2)−(4.5), the spontaneous curvature of the membrane at the given pH (C_0) is

$$C_0 = \frac{1}{r} = \frac{2(c-1)}{t(c+1)}, \text{ where } c = \sqrt{\frac{dA_{out}}{dA_{in}}} = \sqrt{\frac{1 + \alpha_A \Delta pH_{out}}{1 + \alpha_A \Delta pH_{in}}}.$$ (4.6)

Therefore, C_0 can be determined by the given pH values of the inner and outer surfaces of the membrane. The details of pH profiles used in this simulation will be explained in Section 4.2.5.

4.2.2. Area expansion coefficient (α_A)

The area expansion coefficient (α_A) can be estimated from the measurements of the mean area per lipid molecule at different pH values. For the GUV simulations, we used the mean area per lipid measured in Ref. [12]. The mean area per lipid molecule in monolayers composed of 90 mol % of phosphatidylcholine (PC) and 10 mol % of cardiolipin (CL) was measured at pH 8 and 4. The mean area decreased ~8.6% as pH decreased from 8 to 4. From Eq. (4.1), this corresponds to α_A of 0.0214. We used this value for the area expansion coefficient of the GUV (α_{GUV}=0.0214).

For the simulations at the mitochondrial scale, we applied different values of α_A. Since the lipid composition of the IMM is different from that of the GUV, the IMM can have a different α_A. In particular, the IMM has higher CL composition (~20 %) [25, 26], which is considered to be the main contributor for the pH-dependent area change [12, 14, 27, 28]. Thus, this higher CL composition can provide greater α_A than α_{GUV}. Moreover, it has been speculated that the CL composition in the cristae membrane is even higher [29, 30]. However, to the best of our knowledge, accurate CL composition in the critae membrane has not been estimated. Therefore, we performed simulations with various α_A in the range between α_{GUV} and 10 times of α_{GUV}.

4.2.3. Lipid bilayer model

To simulate the lipid bilayer mechanics, we employed the model developed by Feng, Ma, and Klug [19, 21]. We modified the model suitable for the 2D axisymmetic geometry and large deformation. Since the lipid bilayer mechanics is not a main focus of this study, we will briefly explain the lipid bilayer model (see Ref. [21] for more detailed descriptions of the lipid bilayer model).

Following Ref. [21], the total energy functional (I) of the single closed membrane can be written as

$$I = \Pi + I^{con} + I^{reg},$$ (4.7)

where Π is the potential energy, I^{con} is the constraint energy, and I^{reg} is the regularization energy.

The potential energy (Π) was constructed from the Helfrich functional [31-33].

$$\Pi = \int \frac{1}{2} K (2H - C_0)^2 A ds,$$ (4.8)

where K is the bending modulus, H is the mean curvature, C_0 is the spontaneous curvature, and Ads is the infinitesimal surface area element. The potential energy was only composed of the bending energy because we assumed no work was done by external forces. The Gaussian curvature term in the Helfrich functional was neglected by the Gauss-Bonnet theorem.

To enforce area and volume constraints, the constraint energy I^{con} was established by applying the augmented Lagrangian approach.

$$I^{con} = \frac{\mu_V}{2}(V - V_0)^2 - p^n V + \frac{\mu_A}{2}(A - A_0)^2 + \alpha^n A,$$ (4.9)

where V and V_0 are the current and the initial enclosed volumes, respectively; A and A_0 are the current and the initial surface areas, respectively; μ_V and μ_A are penalty parameters for the volume and area constraints, respectively; p^n and α^n are multiplier estimates for the volume and area constraints at the nth iteration, respectively. By employing this energy functional, Lagrange multipliers for the volume and area constraints can be solved iteratively.

However, the constraint energy I^{con} can only impose global constraints. This constraint does not penalize in-plane deformations of finite element nodes and does not enforce local incompressibility. Especially in large deformation problems, these in-plane deformations may induce degenerate modes. To resolve this problem, we used dashpot regularization energy (which penalizes in-plane deformations) introduced by Ma and Klug [21].

$$I^{reg} = \sum_{edge\ ab} \frac{k}{2}(l_{ab} - L_{ab})^2 ,\tag{4.10}$$

where k is a spring constant, l_{ab} and L_{ab} are lengths between nodes a and b of current and reference configurations, respectively.

From the principle of minimum potential energy, the weak form of the energy functional was derived from the variation of a functional.

$$\delta I = \delta \Pi + \delta I^{con} + \delta I^{reg} ,\tag{4.11}$$

$$\delta \Pi = \int \left[K(2H - C_0)\delta(2H)A + \frac{1}{2}K(2H - C_0)^2 \delta A \right] ds ,\tag{4.12}$$

$$\delta I^{con} = \int [-p^{n+1}\delta V + \alpha^{n+1}\delta A] ds ,\tag{4.13}$$

$$\delta I^{reg} = \sum_{edge\ ab} k(l_{ab} - L_{ab})\delta l_{ab} ,\tag{4.14}$$

where $p^{n+1}=p^n-\mu_V(V-V_0)$ and $\alpha^{n+1}=\alpha^n+\mu_A(A-A_0)$.
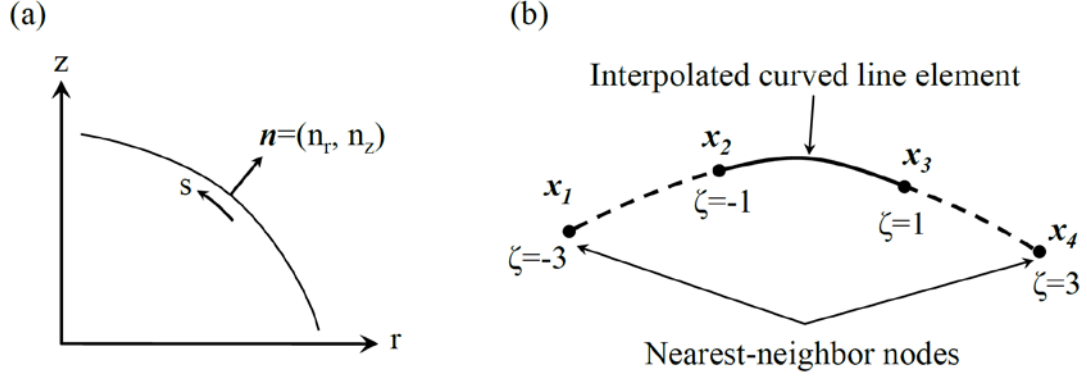
Figure 4.2. 2D axisymmetric coordinate system and geometry of the surface represented by curved line elements. (a) The membrane surface was parameterized by curvilinear coordinates: $x=x(s)$. (b) A curved line element was obtained from interpolating 4 node points including nearest-neighbor nodes.

Next, we derived the variables in 2D axisymmetric coordinate system. As can be seen in Fig. 4.2(a), the normal vector n is

$$n = (n_r, n_z) = (\frac{z'}{(r'^2 + z'^2)^{1/2}}, \frac{-r'}{(r'^2 + z'^2)^{1/2}}),$$ (4.15)

where the single quotation mark ($'$) denotes a partial differentiation with respect to the parameter s.

From the definition of the mean curvature and Eq. (4.15), the mean curvature can be derived as

$$2H = \nabla \cdot n = \frac{1}{r}\frac{\partial(rn_r)}{\partial r} + \frac{\partial n_z}{\partial z} = \frac{r'z'' - z'r''}{(r'^2 + z'^2)^{3/2}} + \frac{z'}{r(r'^2 + z'^2)^{1/2}}.$$ (4.16)

By the first variation of Eq. (4.16), δH can be obtained as

$$\delta(2H) = c_1\delta r + c_2\delta r' + c_3\delta r'' + c_4\delta z' + c_5\delta z'', \tag{4.17}$$

where $c_1 = -\dfrac{z'}{r^2(r'^2 + z'^2)^{1/2}}$, $c_2 = \dfrac{z'^2 z'' - 2r'^2 z'' + 3r'r''z' - (r'z'^3 + r'^3 z')/r}{(r'^2 + z'^2)^{5/2}}$,

$c_3 = -\dfrac{z'}{(r'^2 + z'^2)^{3/2}}$, $c_4 = \dfrac{-r'^2 r'' - 3r'z'z'' + 2r''z'^2 + (r'^4 + r'^2 z'^2)/r}{(r'^2 + z'^2)^{5/2}}$, and

$c_5 = \dfrac{r'}{(r'^2 + z'^2)^{3/2}}$.

The total surface area can be calculated as

$$A_{tot} = \int A ds = \int 2\pi r(r'^2 + z'^2)^{1/2} ds. \tag{4.18}$$

From the above equation, the infinitesimal surface area is

$$A = 2\pi r(r'^2 + z'^2)^{1/2}. \tag{4.19}$$

Then, the first variation of A is

$$\delta A = 2\pi[(r'^2 + z'^2)^{1/2}\delta r + rr'(r'^2 + z'^2)^{-1/2}\delta r' + rz'(r'^2 + z'^2)^{-1/2}\delta z']. \tag{4.20}$$

Similarly,

$$V_{tot} = \int V ds = \int \pi r^2 z' ds, \tag{4.21}$$

$$V = \pi r^2 z', \tag{4.22}$$

$$\delta V = (2\pi r z')\delta r + (\pi r^2)\delta z'. \tag{4.23}$$

Finally, the weak form of the energy functional was applied to find the conjugate direction for the numerical optimization method.

4.2.4. Finite element approximation and energy minimization

Curved line elements were used to approximate the membrane surface in the 2D axisymmetric coordinate system. Because the curvature calculation requires the second derivative of a function, the interpolation (or shape) function need to be at least a quadratic polynomial in order to have a nonzero curvature. To implement this, we used a cubic polynomial function as a shape function. As can be seen in Fig. 4.2(b), shape functions were obtained from interpolating 4 node points including nearest-neighbor nodes.

$$x(\zeta) = \sum_{i=1}^{4} N_i(\zeta)x_i ,$$ (4.24)

where x is a position vector of the membrane surface, N_i is a shape function, and x_i is a node point vector . To construct isoparametric shape functions, following conditions are applied.

$N_1(-3)=1$, $N_1(-1)=0$, $N_1(1)=0$, $N_1(3)=0$,

$N_2(-3)=0$, $N_2(-1)=1$, $N_2(1)=0$, $N_2(3)=0$,

$N_3(-3)=0$, $N_3(-1)=0$, $N_3(1)=1$, $N_3(3)=0$,

$N_4(-3)=0$, $N_4(-1)=0$, $N_4(1)=0$, $N_4(3)=1$.

Because there are 4 conditions for each equation, we use cubic polynomial functions. From the above conditions, the resulting shape functions are

$$N_1 = \frac{1}{48}(-x^3 + 3x^2 + x - 3) ,$$

$$N_2 = \frac{1}{48}(3x^3 - 3x^2 0 - 27x + 27) ,$$

$$N_3 = \frac{1}{48}(-3x^3 - 3x^2 + 27x + 27),$$

$$N_4 = \frac{1}{48}(x^3 + 3x^2 - x - 3).$$

The total energy functional and its weak form were discretized by substituting the position vector x with a node point vector x_i. At the given node positions, the numerical values of these discretized equations (Eqs. 4.7 and 4.11) can be evaluated by using a three-point Gaussian quadrature.

Finally, simulations were performed by applying the nonlinear conjugate gradient method. The nonlinear conjugate method is used to find the local minimum of the total energy functional without deriving the stiffness matrix. The weak form of the total energy functional was used to find the steepest descent direction and the conjugate direction for the numerical optimization. In this study, we used the Polak-Ribiere-Polyak formula for calculating the conjugate gradient update parameter [34, 35].

4.2.5. Initial configurations, pH profiles, and post-processing

We used oblate and prolate spheroids as initial shapes because the simulations were performed in 2D axisymmetric geometries. These initial shapes were parameterized by the equivalent radius (R_0) and the reduced volume (v).

$$R_0 = \sqrt{A/4\pi}, \tag{4.25}$$

$$v = \frac{V}{(4\pi/3)R_0^3}. \tag{4.26}$$

Since these initial shapes are not in equilibrium, the equilibrium shapes of these initial shapes were obtained by performing simulations with the zero spontaneous curvature. Finally, these equilibrium shapes were used as the initial configurations.
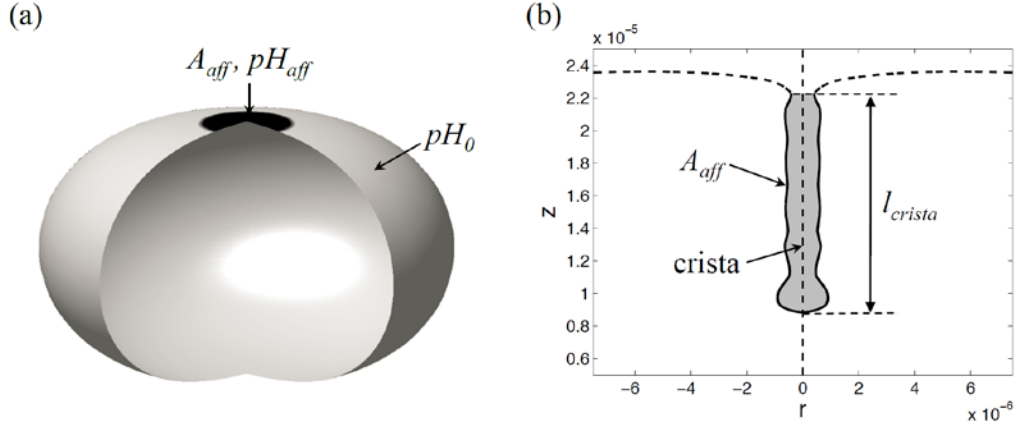
Figure 4.3. pH profile on the membrane surface and morphological parameters of a cristae-like structure. (a) The area affected by acid delivery (A_{aff}) was set on the top center part of the membrane. (b) Morphological parameters were calculated from the structure enclosed by the affected area (shaded area).

To simulate the experimental conditions described in Ref. [12], we defined the area affected by acid delivery (A_{aff}). As can be seen in Fig. 4.3(a), we set the affected area on the top center part of the membrane surface. To study the effects of the affected area, we changed the percentage of the affected area (P_{aff}).

$$P_{aff} = \frac{A_{aff}}{A_0} \times 100.$$

(4.27)

We assigned pH values at the node points of the affected area (pH_{aff}), while pH values elsewhere were assumed to remain at 8 (pH_0). For numerical integration, pH values at the

Gauss points were linearly interpolated from the nodal values. We decreased pH values of the affected area from pH_0 with a decrement of 0.1. However, during this process, the affected area can change due to the updates of node points. This problem is resolved by repositioning the node points. After every energy minimization step, the node points are repositioned along the surface of the membrane in order to have the same affected area. The overall simulation procedure is summarized as follows:

i) Set initial parameters and the reference configuration X

ii) Solve for the current configuration x at the given pH profile by the total energy minimization

iii) Reposition the node points

iv) Update the reference configuration: $X=x$

v) Update parameters (μ_V, μ_A, p^n, and α^n)

vi) Repeat steps ii−v until $|v-v_0|/v_0 < 10^{-5}$ and $I^{reg}/I < 10^{-5}$

After solving for the configuration at each pH step, the morphology of a cristae-like structure was quantified. Fig. 4.3(b) shows an example of a cristae-like strucuture. To quantify this morphology, we calculated the length (l_{crista}), radius (r_{crista}), aspect ratio (AR), and surface-to-volume ratio (SVR) of the cristae-like structure.

$$r_{crista} = \sqrt{\frac{-\int_{crista} \pi r^2 z' ds}{\pi l_{crista}}} \,, \tag{4.28}$$

$$AR = \frac{l_{crista}}{2r_{crista}}, \tag{4.29}$$

$$SVR = \frac{\int_{crista} 2\pi r(r'^2 + z'^2)^{1/2}ds}{-\int_{crista} \pi r^2 z'ds} .$$

(4.30)

(Note: a radius of a crista (r_{crista}) was defined as a radius of an equivalent cylinder.)

Finally, we analyzed the simulation results with these four morphological parameters: l_{crista}, r_{crista}, *AR*, and *SVR*.

4.3. RESULTS

We first simulated the equilibrium shapes of the membranes with a zero local pH gradient (or zero spontaneous curvature) for the verification purpose. After the verification of the model, we simulated the membrane dynamics at the GUV scale (R_0=30 μm). The formation and dissipation of the cristae-like structure with respect to the pH values on the affected area (pH_{aff}) was studied. We also investigated the factors, such as the percentage of the affected area (P_{aff}) and initial shapes, which may affect the morphology of the cristae-like structure. Finally, simulations were performed at the mitochondrial scale (R_0=1 μm). At this smaller scale, we examined the conditions (ex. the critical pH value and the area expansion coefficient) required for the tubular cristae formation.

4.3.1. Model verification

For the model verification, we simulated the equilibrium shapes of the membranes with different initial shapes and zero local pH gradient (i.e. zero spontaneous curvature). The normalized potential energy ($\Pi/8\pi K$) calculated from the equilibrium shape was compared with the result obtained from Seifert et al. [36].
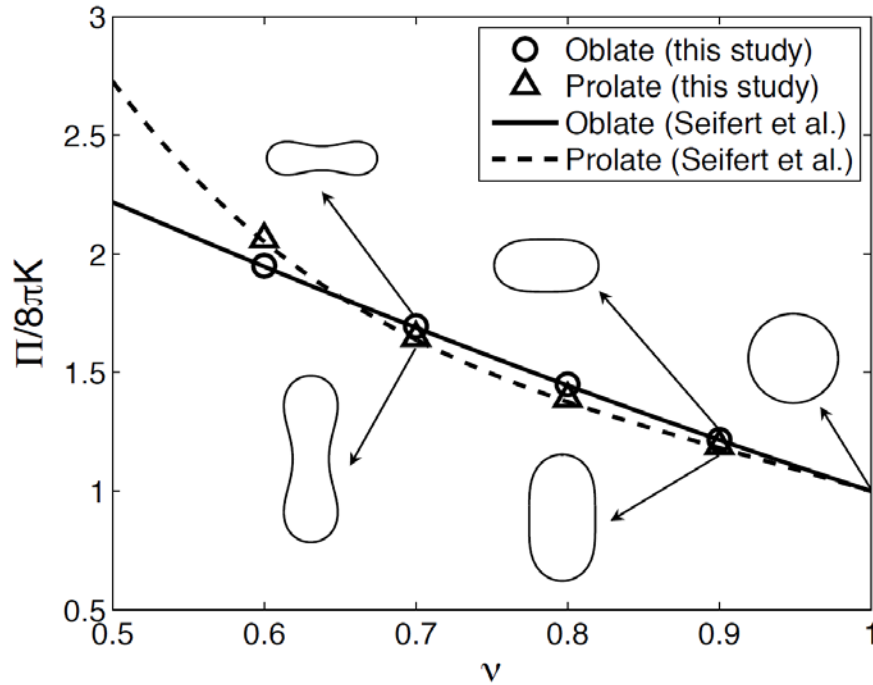
Figure 4.4. Comparison of the normalized potential energy calculated in this study with those obtained from Seifert et al. Equilibrium shapes of oblate and prolate spheroids at selected reduced volumes were presented in the inset.

Fig. 4.4 shows the normalized potential energy and equilibrium shapes of oblate and prolate spheroids with different reduced volume. As can be seen in this figure, our simulation results were in good agreement with those from Seifert et al.

4.3.2. Formation and dissipation of the cristae-like structure at the GUV scale

The dynamics of the membrane was studied at the GUV scale. We used an oblate spheroid with $v=0.95$ and $R_0=30$ μm as an initial shape and the area expansion coefficient (α_A) of 0.0214 (α_{GUV}).

Figure 4.5. Formation process of the cristae-like structure at selected pH_{aff}. An oblate spheroid with $v=0.95$ and $R_0=30$ μm was used as an initial shape. α_A of 0.0214 (α_{GUV}) and P_{aff} of 0.5% were used.

First, the equilibrium shape of the membrane was simulated at pH 8 (zero spontaneous curvature). We assigned the affected area at the top center of the membrane

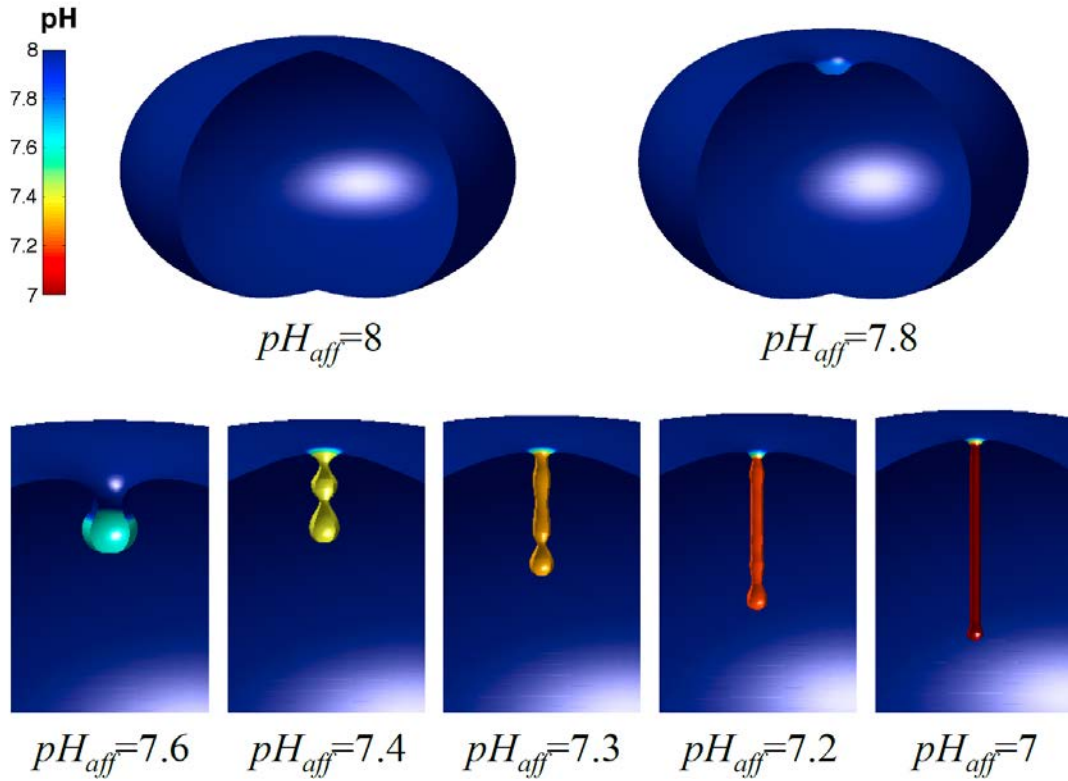surface as described in Section 4.2.5. The percentage of the affected area over the total surface area (P_{aff}) was maintained at 0.5%. We decreased the pH value of the affected area (pH_{aff}) from 8 to 7 with a decrement of 0.1.

As can be seen in Fig. 4.5, the affected area started to form a concave geometry due to the negative spontaneous curvature induced by pH_{aff}. As pH_{aff} decreased, a single spherical shape of a cristae-like structure emerged at pH_{aff}=7.6. Then the affected area evolved to a structure of connected spheres with smaller radii in order to have a greater negative spontaneous curvature. Finally, the affected area formed a tubular cristae-like structure. At pH_{aff}=7, the diameter ($2r_{crista}$) and the length (l_{crista}) of the cristae-like structure were 0.94 μm and 17.5 μm, respectively.

To study the reversibility of this membrane deformation, we increased pH_{aff} from 7 to 8 with an increment of 0.1. The membrane configuration at pH_{aff}=7 in Fig. 4.5 was used as an initial configuration for this simulation.

Fig. 4.6 shows the dissipation of the cristae-like structure with increasing pH_{aff}. At the same pH_{aff}, the morphology of the cristae-like structure shown during the dissipation process (Fig. 4.6) was very similar to that which emerged during the formation process (Fig. 4.5). However, at pH_{aff}=7.3, the structure of connected spheres was more clearly seen in the dissipation process. This slight difference in morphology may be caused by the different initial conditions for the formation process and the dissipation process (i.e., the equilibrium configurations in the formation process were developed from the configurations at the higher pH values, whereas those in the dissipation process were progressed from the configurations at the lower pH values). Finally, the cristae-like

structure was completely removed and the membrane was fully recovered to the original configuration when the local pH gradient disappeared (pH_{aff}=8).
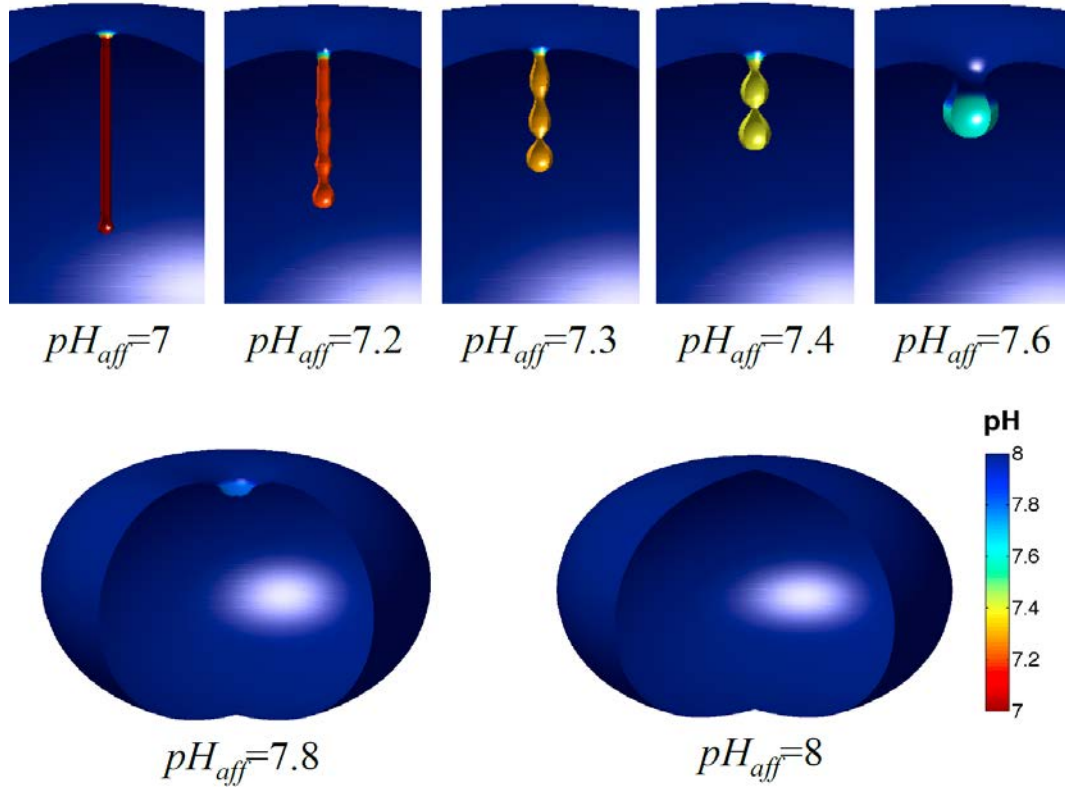
Figure 4.6. Dissipation process of the cristae-like structure at selected pH_{aff}. The membrane configuration at pH_{aff}=7 in Fig. 4.5 was used as an initial configuration. α_A of 0.0214 (α_{GUV}) and P_{aff} of 0.5% were used.

4.3.3. The effects of P_{aff} and initial shapes

To investigate the factors determining the morphology of the cristae-like structure, membrane models with different P_{aff} and initial shapes were simulated. The morphology

of the cristae-like structure at each pH_{aff} was analyzed by using four morphological parameters as described in Section 4.2.5: r_{crista}, l_{crista}, AR, and SVR.
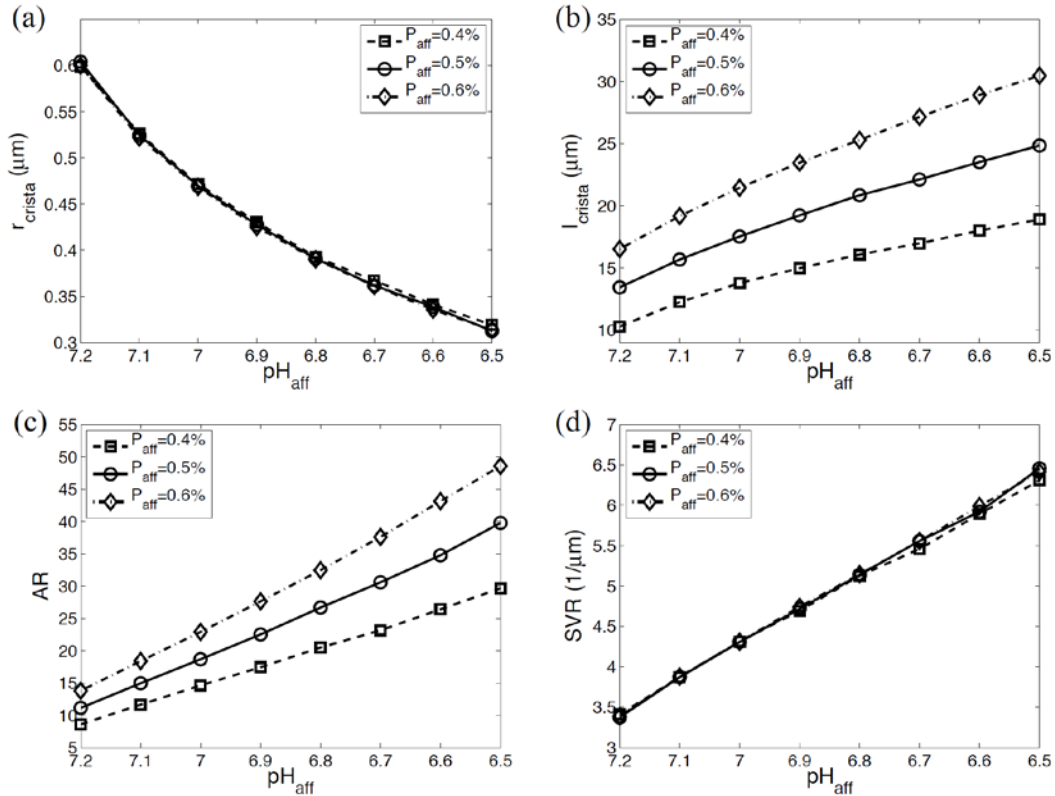
Figure 4.7. The effects of the percentage of the affected area (P_{aff}) on the morphological parameters of a cristae-like structure. (a) Changes in the radius of cristae-like structures. (b) Changes in the lengths of cristae-like structures. (c) Changes in the aspect ratios of cristae-like structures. (d) Changes in the surface-to-volume ratios of cristae-like structures.

The morphological changes of the critae-like structures with three different P_{aff} (0.4%, 0.5%, and 0.6%) were analyzed. The same initial configuration (oblate spheroid with v=0.95 and R_0=30 μm) and the area expansion coefficient (α_A) of 0.0214 were used.

As can be seen in Fig. 4.7(b) and (c), the cristae-like structure developed from a larger affected area was longer and consequently had a higher aspect ratio. On the other hand, the percentage of the affected area did not show significant effects on both r_{crista} and SVR (Fig. 4.7(a) and (d)). Because these two morphological parameters are mainly determined by the spontaneous curvature (which is directly related to the local pH), they were only associated with pH_{aff}.

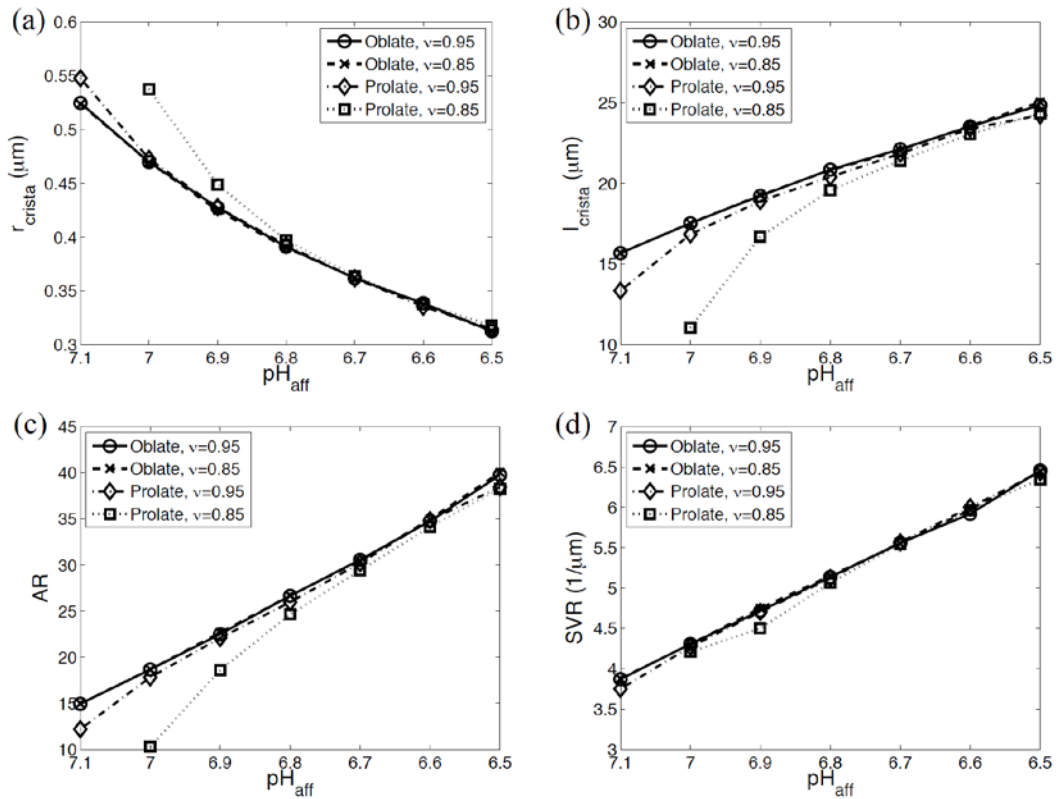Figure 4.8. The effects of the initial shape on the morphological parameters of a cristae-like structure. Oblate and prolate spheroids with v=0.95 and 0.85 were used as initial shapes. (a) Changes in the radius of cristae-like structures. (b) Changes in the lengths of cristae-like structures. (c) Changes in the aspect ratios of cristae-like structures. (d) Changes in the surface-to-volume ratios of cristae-like structures.

To study the effects of the initial shape, four different initial configurations were simulated at the same conditions (R_0=30 μm, α_A=0.0214, P_{aff}=0.5%). Fig. 4.8 shows the effects of the initial shapes on the morphological parameters. Oblate spheroids with two different reduced volumes (v=0.95 and 0.85) exhibited almost identical morphological parameters over the entire range of pH_{aff}, whereas prolate spheroids showed delayed growth of tubular cristae-like structures. In the case of the oblate spheroid, the initial pH value for tubular cristae-like structure formation was 7.2. The prolate spheroids with v=0.95 and v=0.85 started to form a tubular cristae-like structure at pH 7.1 and 7, respectively. Moreover, the prolate spheroids developed initially thicker and shorter cristae-like structures. This delayed formation and development of the cristae-like structure from the prolate spheroids may be contributed from the higher positive curvature of the affected area (i.e., in prolate spheroids, the membrane invagination may be hindered by the more convex geometry of the affected area). However, after the cristae-like structures were fully formed, the morphological parameters of prolate spheroids were converged to those of oblate spheroids.

4.3.4. Cristae formation at the mitochondrial scale

The membrane dynamics was finally simulated at the mitochondrial scale. We investigated whether the same mechanism applied at the GUV scale can still be valid at the smaller mitochondrial scale. An oblate spheroid with v=0.95 and R_0=1 μm was used as an initial shape. We maintained the percentage of the affected area (P_{aff}) of 0.5%, while pH_{aff} was decreased from 8 to 4.

As can be seen in Fig. 4.9(a), when α_A of 0.0214 (α_{GUV}) was applied, the affected area formed a concave geometry instead of a tubular cristae-like structure. This is due to the higher negative spontaneous curvature required to form a smaller crista.
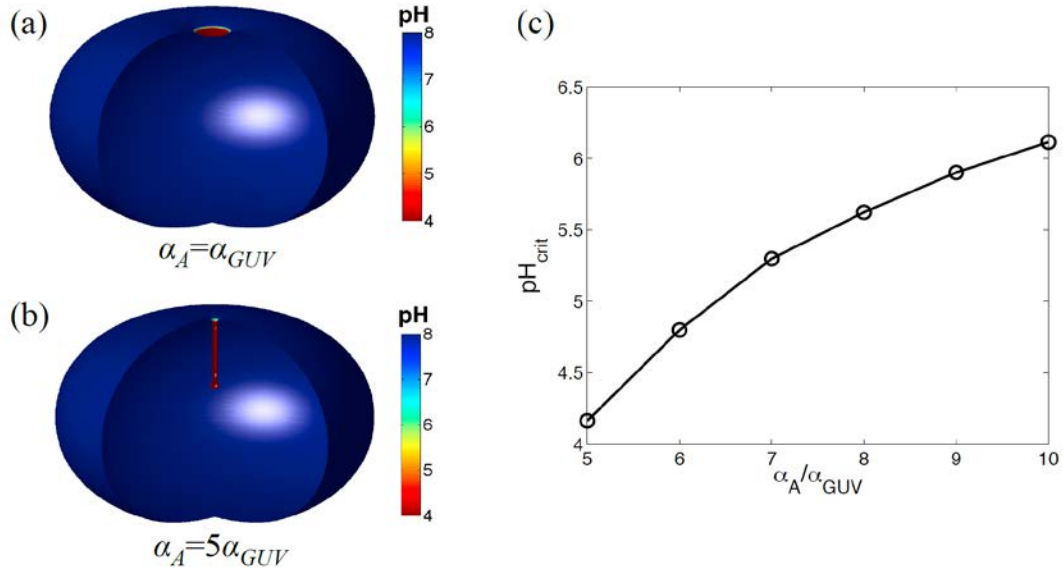
Figure 4.9. Cristae formation at the mitochondrial scale. (a) The membrane morphology simulated with α_{GUV} at pH_{aff}=4. (b) The membrane morphology simulated with $5\alpha_{GUV}$ at pH_{aff}=4. (c) Critical pH values required to form a tubular cristae-like structure with different area expansion coefficients.

The higher negative spontaneous curvature can be achieved by a higher local pH gradient (lower pH_{aff}) or a greater α_A. Since the applicable range of pH_{aff} is limited (a pH_{aff} lower than 4 might not be feasible due to the lipid degradation in acid), we performed simulations with greater area expansion coefficients (α_A was increased up to 10 times of α_{GUV}). When α_A=$5\alpha_{GUV}$, a tubular cristae-like structure was fully developed at pH_{aff}=4 (Fig. 4.9(b)).

We further investigated a critical pH value (pH_{crit}) required to form a tubular cristae-like structure. From the simulation results, we calculated the pH_{crit} where the membrane formed a crista with a diameter ($2r_{crista}$) of 40 nm. Fig. 4.9(c) shows the calculated pH_{crit} with different α_A. To form a tubular crista at pH 5 and 6, α_A of the cristae membrane should be greater than 6.4 times and 9.5 times of α_{GUV}, respectively. As explained in Section 4.2.2, for the actual cristae membrane, this greater α_A may be achieved by a higher CL composition of the cristae membrane. However, the accurate CL composition and the area expansion coefficient of the cristae membrane are still unknown.

4.4. DISCUSSION

In this section, by comparing the existing experimental observations, we first discuss the validity of the major findings in this study. In addition to the validation, the limitations from the model assumptions and simplifications are discussed.

4.4.1. Comparison with existing experimental observations

Through the simulation model, we showed that a tubular cristae structure can be formed and regulated by the local pH gradient. Even though the model did not reproduce complex and entangled geometries (due to the application of simple axisymmetric geometries), early steps of the cristae-like structure formation (from a concave geometry to a single sphere, connected spheres, and a tubular structure) and final steps of the

dissipation (from a tubular structure to connected spheres, a single sphere, and a concave geometry) were consistent with those observed in Ref. [12]. This distinctive process was more clearly seen during the dissipation of a cristae-like structure (see figures in Ref. [12]). This might be due to the fact that the complete disappearance of the local pH gradient after removing acid delivery takes more time than the development of the local pH gradient, and this slower process can provide more time for having a fully equilibrated membrane configuration (similar to those in the simulation results). Furthermore, the simulation results, which showed a decrease in the tubular crista radius accompanied by a increase in the local pH gradient, correspond to the experimental observations of actual cristae structures: swollen cristae were observed in mitochondria at state 3 (low local pH gradient), while narrow tubular cristae were shown in mitochondria at state 4 (high local pH gradient) [8].

Additionally, we investigated the effects of the affected area and the initial shape. First, the simulation results suggested that the affected area can only change the length, but not the diameter of a crista. From these simulation results, we can infer that the diameter of each crista may be nearly uniform if the local pH values on the cristae membranes are comparable. This inference is supported by the observations that found relatively small variations in tubular cristae diameters (20~40 nm) [37, 38]. Second, we showed that the initial shape can affect the growth of a tubular crista: The initial tubular crista formation on the membrane with higher positive curvature requires higher local pH gradient. Thus, the tubular cristae formation on a flat or concave surface is more favorable. This finding explains the direction of tubular cristae that is mostly perpendicular to the longitudinal axis of mitochondria [37, 39].

Simulations at the mitochondrial scale were performed with a range of area expansion coefficients. At this small scale, developing a tubular crista comparable to its actual size (diameter of 40 nm) requires a greater area expansion coefficient and higher local pH gradient. In reality, the area expansion coefficient of the cristae membrane may be much greater than that estimated from the GUV due to higher CL composition. Additionally, the higher local pH gradient can be obtained by the locally concentrated protons on the cristae membrane (enhanced proton trapping by higher CL composition) [12, 14, 27, 28]. According to our simulation results, the local CL composition and pH gradient on the cristae membrane might be higher than those speculated in the existing literature. However, due to the limitations in optical resolution and diffusion, these local values have not been accurately measured.

4.4.2. Model assumptions and limitations

We discuss the limitations from the model assumptions and simplifications. As mentioned earlier, we limited our study to the 2D axisymmetric coordinate system in order to reduce the computational cost and avoid numerical instabilities by applying extremely fine elements. Because of the symmetric geometries and pH profiles, detailed membrane dynamics that deviated from symmetric conditions could not be simulated.

In addition, we did not consider the effects of pH on mechanical properties of the membrane, such as the area expansion coefficient (α_A) and the bending modulus (K). However, studies have found that these mechanical properties can be altered by pH [40-42].
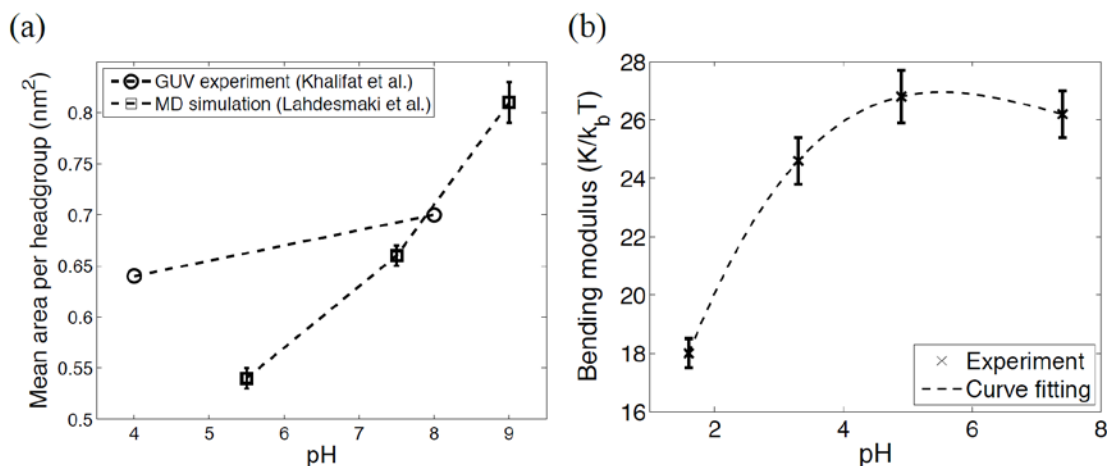
Figure 4.10. The effects of pH on the mechanical properties of lipid bilayers. (a) The correlation between the mean area per headgroup and pH estimated from the GUV experiment and the molecular dynamics (MD) simulation. (b) Bending modulus as a function of pH.

Fig. 4.10(a) shows the pH-dependent area changes estimated from the GUV experiment [12] and the molecular dynamics (MD) simulation [41]. The MD simulation results showed that the area expansion coefficient does not considerably depend on pH (i.e., almost linear relationship between the mean area per headgroup and pH). In the GUV experiment, however, the functional form of the correlation between the area per headgroup and pH could not be determined because the mean area per headgroup was measured only at two different pH values (pH 4 and 8). Since the compositions of lipid used in the MD simulation and the GUV experiment are different, the validity of our assumption of the linear relationship between the area per headgroup and pH is not yet conclusive.
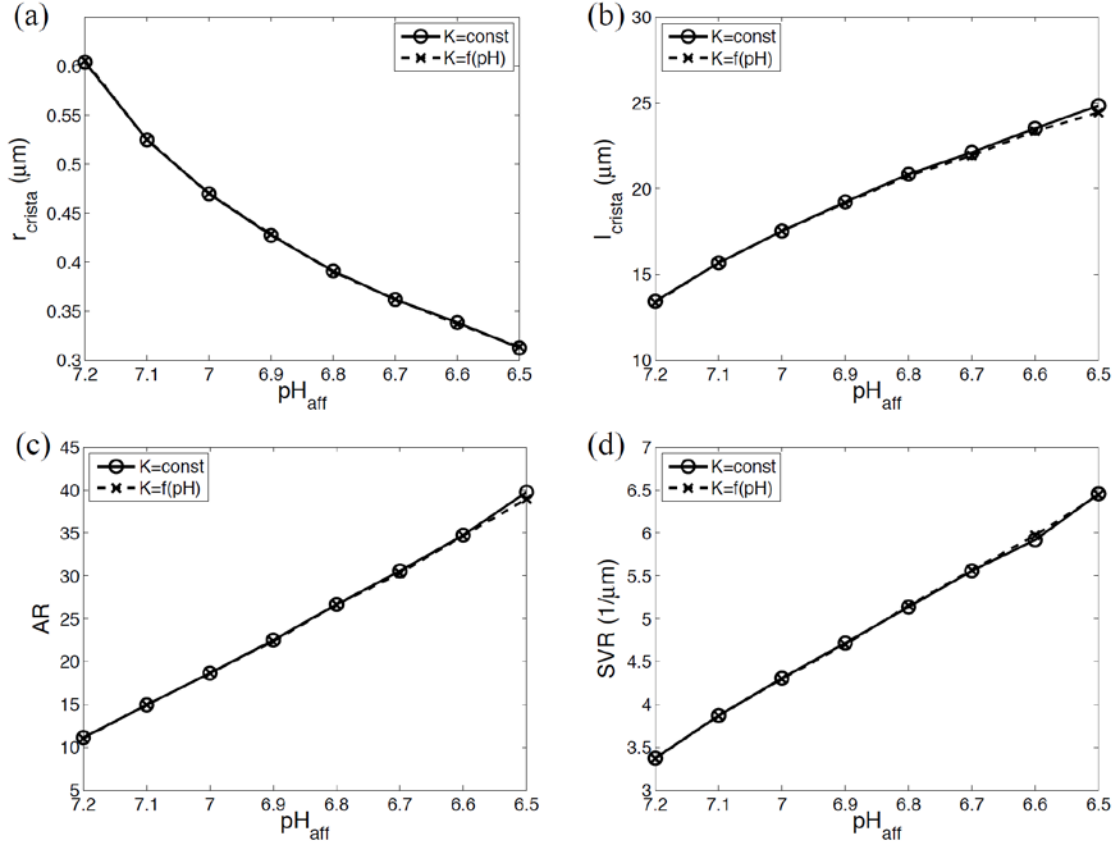
Figure 4.11. The effects of the pH-dependent bending modulus on the morphological parameters of a cristae-like structure (oblate spheroid with $v=0.95$, $R_0=30$ μm, $\alpha_A= \alpha_{GUV}$, $P_{aff}=0.5\%$).

As can be seen in Fig. 4.10(b), the bending modulus may be a function of pH. In order to examine whether the pH-dependent bending modulus may affect the simulation results, we modeled the bending modulus as a function of pH ($K=f(pH)$, where f is a cubic polynomial function) by curve-fitting the experimental data in Ref. [40]. This bending modulus was then applied to our simulation model. Within the range of pH values used in this study (from pH 6.5 to 8), applying the pH-dependent bending modulus did not notably affect our simulation results (Fig. 4.11). Thus, the bending modulus of the IMM

may be assumed as a constant (pH-independent) within the feasible pH range of mitochondria.

Next, with an assumption of a homogeneous lipid membrane, the effects of protein complexes were not modeled. However, the insertion of a protein complex, such as ATP synthase, has been hypothesized to bend the membrane [10, 11]. Thus, in conjunction with the local pH gradient, the spontaneous curvature of the protein complex may contribute to the formation and regulation of cristae structures.

Finally, we assumed localized protons on the cristae membrane (or the affected area by acid delivery) without considering the diffusion of protons along the membrane surface. Even though a meticulous modeling of the pH profile may provide more precise cristae dynamics, it requires consideration of many modeling parameters and physics (such as activities of proton source and sink, electric potential, and transport of proton), which may complicate the effects of the local pH on the crista morphology.

4.5. CONCLUSIONS

The complex and widely varied cristae morphologies have been studied in relation to mitochondrial functions. However, the mechanisms of how these cristae structures can be regulated and related to energetic functions of mitochondria are not clear. To date, the formation and regulation of cristae morphologies have been hypothesized i) by the distributions of protein complexes and ii) by the local pH gradient. Among these two hypotheses, we exclusively investigated the effects of the local pH gradient by using a numerical model.

To develop a numerical model simulating the morphologies of the IMM at the given pH profiles, we modeled a spontaneous curvature induced by the pH difference across the membrane. This spontaneous curvature was then applied to the finite element model of a single closed lipid bilayer in order to find the energetically favorable membrane configuration. This simulation model allows us to investigate the effects of the local pH on the IMM dynamics.

From this study, we developed the first numerical model simulating the dynamics of cristae structures, from which we substantiated the hypothesis that a tubular crista structure can be formed and regulated by the local pH gradient and investigated the effects of the local pH gradient on the morphological parameters of the crista structure. Moreover, through the simulations with various initial conditions, we provided the potential explanations of the relatively uniform diameter and direction of the tubular cristae: the diameter of a crista is mainly determined by the local pH gradient, and the energetically favorable direction of a crista is perpendicular to the longitudinal axis of mitochondria (the initial formation of a crista on a less convex membrane surface requires less pH gradient). Finally, we presented that the formation of the tubular cristae structure at the actual mitochondrial scale requires a greater area expansion coefficient than that estimated from the GUV experiment. This simulation result supported the hypothesis that the cristae membrane may have a higher composition of CL than the other parts of the IMM.

4.6. BIBLIOGRAPHY

1. P. Mitchell, Chemiosmotic coupling in oxidative and photosynthetic phosphorylation. *Biological Reviews* 41, 445 (1966).
2. N. Kocherginsky, Acidic lipids, H$^+$-ATPases, and mechanism of oxidative phosphorylation. Physico-chemical ideas 30 years after P. Mitchell's Nobel Prize award. *Progress in Biophysics and Molecular Biology* 99, 20 (2009).
3. R. W. Gilkerson, J. M. L. Selker, and R. A. Capaldi, The cristal membrane of mitochondria is the principal site of oxidative phosphorylation. *FEBS Letters* 546, 355 (2003).
4. F. Vogel, C. Bornhövd, W. Neupert, and A. S. Reichert, Dynamic subcompartmentalization of the mitochondrial inner membrane. *The Journal of Cell Biology* 175, 237 (2006).
5. C. A. Mannella, D. R. Pfeiffer, P. C. Bradshaw, I. I. Moraru, B. Slepchenko, L. M. Loew, C. E. Hsieh, K. Buttle, and M. Marko, Topology of the mitochondrial inner membrane: dynamics and bioenergetic implications. *IUBMB Life* 52, 93 (2001).
6. G. Perkins, E. Bossy-Wetzel, and M. H. Ellisman, New insights into mitochondrial structure during cell death. *Experimental Neurology* 218, 183 (2009).
7. M. Zick, R. Rabl, and A. S. Reichert, Cristae formation—linking ultrastructure and function of mitochondria. *Biochimica et Biophysica Acta (BBA) - Molecular Cell Research* 1793, 5 (2009).
8. C. A. Mannella, Structure and dynamics of the mitochondrial inner membrane cristae. *Biochimica et Biophysica Acta (BBA) - Molecular Cell Research* 1763, 542 (2006).
9. G. A. Perkins, and M. H. Ellisman, Mitochondrial configurations in peripheral nerve suggest differential ATP production. *Journal of Structural Biology* 173, 117 (2011).
10. M.-F. Giraud, P. Paumard, V. Soubannier, J. Vaillier, G. Arselin, B. Salin, J. Schaeffer, D. Brèthes, J.-P. di Rago, and J. Velours, Is there a relationship between the supramolecular organization of the mitochondrial ATP synthase and the formation of cristae? *Biochimica et Biophysica Acta (BBA) - Bioenergetics* 1555, 174 (2002).
11. M. Strauss, G. Hofhaus, R. R. Schroder, and W. Kuhlbrandt, Dimer ribbons of ATP synthase shape the inner mitochondrial membrane. *EMBO J* 27, 1154 (2008).
12. N. Khalifat, N. Puff, S. Bonneau, J.-B. Fournier, and M. I. Angelova, Membrane Deformation under Local pH Gradient: Mimicking Mitochondrial Cristae Dynamics. *Biophysical Journal* 95, 4924 (2008).
13. J. B. Fournier, N. Khalifat, N. Puff, and M. I. Angelova, Chemically Triggered Ejection of Membrane Tubules Controlled by Intermonolayer Friction. *Physical Review Letters* 102, 018102 (2009).
14. N. Khalifat, J.-B. Fournier, M. I. Angelova, and N. Puff, Lipid packing variations induced by pH in cardiolipin-containing bilayers: The driving force for the cristae-like shape instability. *Biochimica et Biophysica Acta (BBA) - Biomembranes* 1808, 2724 (2011).

15. C. Renken, G. Siragusa, G. Perkins, L. Washington, J. Nulton, P. Salamon, and T. G. Frey, A thermodynamic model describing the nature of the crista junction: a structural motif in the mitochondrion. *Journal of Structural Biology* 138, 137 (2002).

16. A. Ponnuswamy, J. Nulton, J. M. Mahaffy, P. Salamon, T. G. Frey, and A. R. C. Baljon, Modeling tubular shapes in the inner mitochondrial membrane. *Physical Biology* 2, 73 (2005).

17. M. Ghochani, J. D. Nulton, P. Salamon, T. G. Frey, A. Rabinovitch, and A. R. C. Baljon, Tensile forces and shape entropy explain observed crista structure in mitochondria. *Biophysical Journal* 99, 3244 (2010).

18. T. Taniguchi, Shape Deformation and Phase Separation Dynamics of Two-Component Vesicles. *Physical Review Letters* 76, 4444 (1996).

19. F. Feng, and W. S. Klug, Finite element modeling of lipid bilayer membranes. *Journal of Computational Physics* 220, 394 (2006).

20. J. Demongeot, N. Glade, O. Hansen, and A. Moreira, An open issue: The inner mitochondrial membrane (IMM) as a free boundary problem. *Biochimie* 89, 1049 (2007).

21. L. Ma, and W. S. Klug, Viscous regularization and r-adaptive remeshing for finite element analysis of lipid membrane mechanics. *Journal of Computational Physics* 227, 5816 (2008).

22. C. M. Funkhouser, F. J. Solis, and K. Thornton, Dynamics of two-phase lipid vesicles: effects of mechanical properties on morphology evolution. *Soft Matter* 6, 3462 (2010).

23. K. Guo, and J. Li, Exploration of the shapes of double-walled vesicles with a confined inner membrane. *Journal of Physics: Condensed Matter* 23, 285103 (2011).

24. M. Rahimi, and M. Arroyo, Shape dynamics, lipid hydrodynamics, and the complex viscoelasticity of bilayer membranes. *Physical Review E* 86, 011932 (2012).

25. R. Hovius, H. Lambrechts, K. Nicolay, and B. de Kruijff, Improved methods to isolate and subfractionate rat liver mitochondria. Lipid composition of the inner and outer membrane. *Biochimica et Biophysica Acta (BBA) - Biomembranes* 1021, 217 (1990).

26. G. Daum, and J. E. Vance, Import of lipids into mitochondria. *Progress in Lipid Research* 36, 103 (1997).

27. M. Schlame, D. Rua, and M. L. Greenberg, The biosynthesis and functional role of cardiolipin. *Progress in Lipid Research* 39, 257 (2000).

28. M. Schlame, and M. Ren, The role of cardiolipin in the structural organization of mitochondrial membranes. *Biochimica et Biophysica Acta (BBA) - Biomembranes* 1788, 2080 (2009).

29. M. Bogdanov, E. Mileykovskaya, and W. Dowhan, in *Lipids in Health and Disease,* P. Quinn, X. Wang, Eds. (Springer Netherlands, 2008), vol. 49, pp. 197-239.

30. E. Mileykovskaya, and W. Dowhan, Cardiolipin membrane domains in prokaryotes and eukaryotes. *Biochimica et Biophysica Acta (BBA) - Biomembranes* 1788, 2084 (2009).

31. P. B. Canham, The minimum energy of bending as a possible explanation of the biconcave shape of the human red blood cell. *Journal of Theoretical Biology* 26, 61 (1970).

32. W. Helfrich, Elastic properties of lipid bilayers: theory and possible experiments. *Zeitschrift für Naturforschung. Teil C: Biochemie, Biophysik, Biologie, Virologie* 28, 693 (1973).

33. E. A. Evans, Bending Resistance and Chemically Induced Moments in Membrane Bilayers. *Biophysical Journal* 14, 923 (1974).

34. B. T. Polyak, The conjugate gradient method in extremal problems. *USSR Computational Mathematics and Mathematical Physics* 9, 94 (1969).

35. J. Gilbert, and J. Nocedal, Global Convergence Properties of Conjugate Gradient Methods for Optimization. *SIAM Journal on Optimization* 2, 21 (1992).

36. U. Seifert, K. Berndl, and R. Lipowsky, Shape transformations of vesicles: Phase diagram for spontaneous- curvature and bilayer-coupling models. *Physical Review A* 44, 1182 (1991).

37. G. Perkins, C. Renken, M. E. Martone, S. J. Young, M. Ellisman, and T. Frey, Electron tomography of neuronal mitochondria: three-dimensional structure and organization of cristae and membrane contacts. *Journal of Structural Biology* 119, 260 (1997).

38. G. A. Perkins, C. W. Renken, T. G. Frey, and M. H. Ellisman, Membrane architecture of mitochondria in neurons of the central nervous system. *Journal of Neuroscience Research* 66, 857 (2001).

39. R. Schmidt, C. A. Wurm, A. Punge, A. Egner, S. Jakobs, and S. W. Hell, Mitochondrial Cristae Revealed with Focused Light. *Nano Letters* 9, 2508 (2009/06/10, 2009).

40. M. B. Boggara, A. Faraone, and R. Krishnamoorti, Effect of pH and ibuprofen on the phospholipid bilayer bending modulus. *The Journal of Physical Chemistry B* 114, 8061 (2010).

41. K. Lähdesmäki, O. Ollila, A. Koivuniemi, P. T. Kovanen, and M. T. Hyvönen, Membrane simulations mimicking acidic pH reveal increased thickness and negative curvature in a bilayer consisting of lysophosphatidylcholines and free fatty acids. *Biochimica et Biophysica Acta (BBA)-Biomembranes* 1798, 938 (2010).

42. Y. Zhou, and R. M. Raphael, Solution pH alters mechanical and electrical properties of phosphatidylcholine membranes: relation between interfacial electrostatics, intramembrane potential, and bending elasticity. *Biophysical Journal* 92, 2451 (2007).

CHAPTER 5

CONCLUSIONS AND FUTURE WORK

Over the last few decades, as average life expectancy has continuously increased, the importance of research on central nervous system diseases has been emphasized. Even though intensive studies have been conducted and several aspects of these diseases have been revealed, the molecular mechanism of the development and progression of these diseases has not yet been elucidated.

In one effort to reveal this mechanism, the role of mitochondria in CNS diseases has been investigated. Studies have presented evidence supporting the hypothesis that mitochondrial dysfunction may be closely related to the progression of CNS diseases via metabolism disruption and mitochondrial DNA mutation. Moreover, mitochondrial properties have been examined as potential indicators reflecting functional and disease states of mitochondria. However, the precise mechanisms are not fully understood, and quantitative and biophysical approaches on this research area are still insufficient.

Therefore, in this study, we quantitatively investigated alterations in mitochondrial properties under neurotoxin challenge. Additionally, by using a mathematical model, we studied biophysical functions of dynamic and diverse internal mitochondrial structures. Finally, we theoretically examined the mechanism of cristae formation and regulation.

In Chapter 2, we introduced methods for simultaneous quantification of mitochondrial morphology and membrane potential, and investigated the changes in mitochondrial properties under 1,3-DNB exposure. From the image processing and data analysis results, we found the following: i) At the level of individual mitochondria, major membrane potential fluctuations are accompanied by abrupt changes in morphology, ii) at the level of mitochondrial population, the respective effects of 1,3-DNB concentration, exposure time, and cell passage on the mean aspect ratio and the probability of membrane potential fluctuations are statistically significant, and iii) the mitochondrial permeability transition inhibitors may not prevent the 1,3-DNB induced alterations in mitochondrial properties.

In Chapter 3, by applying the finite element method, we studied the biophysical significance of the inner mitochondrial membrane (IMM) structure on the energetic function of mitochondria. By performing simulations with various morphological parameters, we showed that a crista can act as a proton trap, and consequently enhance the capacity for ATP synthesis. Additionally, we found that a high proton motive force can be induced by the large surface-to-volume ratio of a crista, whereas a high capacity for ATP synthesis can be mainly obtained from the large surface area of a crista. Finally, from the simulation results, we supported the hypothesis that cristae morphologies may be regulated by the energy state of mitochondria.

In Chapter 4, we investigated the effects of the local pH gradient on the IMM morphology. By using an energy minimization method, we simulated the morphological evolution of the IMM at the given pH profiles. From the simulation results, we demonstrated that a tubular crista structure can be formed and regulated by controlling

the pH profile. Moreover, we proposed a possible mechanism of relatively uniform diameter and direction of tubular cristae observed in many experimental studies. Finally, the simulation results suggested that the formation of the tubular cristae structure at the actual mitochondrial scale may require a greater area expansion coefficient, which may be achieved by higher cardiolipin composition.

Throughout this dissertation, by using quantitative data analyses and simulations, we investigated mitochondrial properties and their biophysical significance on mitochondrial functions. Even though we presented several significant findings, additional investigations and methodological improvements may provide a better understanding of mitochondrial properties and their functional effects. In the experimental study (Chapter 2), improvements in imaging, image processing, and data analysis techniques are necessary in order to handle biological data with intrinsically high levels of variation. Furthermore, for the validation of the simulation models (Chapters 3 and 4), it is required to accurately estimate local properties such as electric potential, proton concentration, and lipid composition of the cristae membrane. Finally, more precise modeling of mitochondrial electrochemistry and membrane dynamics may be accomplished by combining two numerical models introduced in this study.